UNIVERSITAT POLITÈCNICA
DE CATALUNYA
BARCELONATECH

PhD Thesis

Control and Operation of Multi-Terminal VSC-DC Networks

Cătălin Gavriluţă

Terrassa, November 2014

Control and Operation of Multi-Terminal VSC-DC Networks

Author:

Cătălin Gavriluţă

Supervisor:

Dr. Pedro Rodríguez Cortés

Disertation submitted to the PhD Doctorate Office of the Universitat Politécnica de Catalunya in partial fulfillment of the requirements for the degree of Doctor of Philosophy by the

UNIVERSITAT POLITÉCNICA DE CATALUNYA

Electrical Engineering Department
Research Center on
Renewable Electrical Energy Systems

NOVEMBER 2014

UNIVERSITAT POLITÈCNICA
DE CATALUNYA
BARCELONATECH

Control and Operation of Multi-Terminal VSC-DC Networks

ISBN:–.

Research Projects: ENE 2013-48428-C02-2-R
ENE 2011-29041-C02-01

Printed in Catalunya by the DEE-UPC
November 2014

UNIVERSITAT POLITÉCNICA DE CATALUNYA (UPC)
Electrical Engineering Department (DEE)
Research Center on Renewable Electrical Energy Systems(SEER)
Gaia Building, 3rd floor
Rambla de Sant Nebridi, 22
08222 Terrassa (Barcelona), Spain.
Web:http://seer.upc.edu

Părinţilor mei, pentru tot ce au făcut ca eu să ajung aici...

Mulţumesc.

Acknowledgements

First of all, I would like to thank my supervisor, Prof. Pedro Rodriguez, for providing me the opportunity to carry out my PhD at SEER. His determined attitude and critical thinking challenged my work several times, but for this I can only be grateful, as without his guidance, the outcome of this thesis would have been considerably different.

Further on, I have to thankfully acknowledge the administrative staff at SEER for finding the right tools to fund my research during this time of economical turmoil, and, of course, Lidia, for taking care of all the bureaucracy that surrounded my stay in Spain. Having these two aspects covered, it allowed me to focus exclusively on my research and this helped a lot in the development of my work. Also, to my colleagues at SEER, I have to say that you were a real source of inspiration. It is impressive to see how much a handful of dedicated people can achieve in a few years.

My acknowledgements to Alvaro, for continuously reminding me to publish and for actively pushing the group forward. Joan, thank you for all the things that you built and designed in order for us, the PhD students, to be able to carry out our experiments. Also, thank you for not getting too mad when we accidentally destroyed some of the things you built and designed...

I would like also to thank Prof. Antonio Gómez-Expósito for his advice and timely feedback, as they had a large contribution in improving the quality of my work.

A paragraph here is not sufficient to express my deepest gratitude to Prof. Ignacio Candela. Inaki, thank you for your endless support in my research and for your patience when dealing with my ignorance. You are the true definition of a

mentor and working with you was an eye-opening experience. I really hope that someday I will be able to match your undamped level of enthusiasm and constant curiosity towards science.

I want to also thank all my fellow PhD students, especially Costantino, with whom I shared this ride from the beginning, for all the challenging discussions, all the time spent in the lab, all the football games, and all the dinners. They certainly made my PhD program much more enjoyable.

To my family and friends, sorry for being absent these past years, sorry for all the missed events and gatherings, and sorry for being busy more than often. If I learned something during this time, then it is that, as one iconic wanderer said, happiness is only real when shared. A big thank you to my good friends Ion, Sergiu, and Stefy who walked beside me, inspired me, and believed in me all these years.

I cannot end this section without acknowledging Cosmin, Andrea, Ion, and Patri who proof-read my manuscripts and fought with my poor grammar and my lack of understanding regarding comma rules.

Last but not least, I would like to thank the one person that brings meaning to my life and has kept me on track throughout the years with her constant care and support. Patri, thank you for being by my side and for bringing me peace of mind.

Cătălin Gavriluţă
Terrassa, Spain
November 2014

Abstract

For the past century, ac networks have been established as the standard technology for electrical power transmission systems. However, the dc technology has not disappeared completely from this picture. The capability of dc systems to transmit higher power over longer distances, the possibility of interconnecting asynchronous networks, and their high efficiency has maintained the interest of both industry and academia. Historically, systems based on dc-generators and mercury valves were used for dc power transmission applications, but, by the 90's, all installations were thyristor-based line commutated converters (LCC). In 1999, the first system based on voltage source converters (VSC) was installed in Gotland, Sweden, marking the beginning of a new era for dc transmission. Over the past 15 years, the power rating of VSC-based dc transmission systems has increased from 50 to 700 MW, the operating voltage from 120 to 500 kV, meanwhile, the covered distances have become as long as 950 km (ABB's HVDC-light installation in Namibia in 2010).

The advancement of VSC technology applied to dc transmission has also rekindled the idea of multi-terminal dc (MTDC) networks. The interest in the area has been fueled by the increased feasibility of these systems for the large scale integration of remote offshore wind resources. Daring projects as the North Sea Supergrid, which proposes to use such a network for integrating the wind power resources of the North Sea into the mainland grids, have given rise to a lot of research in this field for the past few years. However, despite the active research effort in the field, at the moment, issues related to the operation and control of these networks, as well as sizing, are still uncertain.

The work presented in this thesis is oriented towards the control and operation of MTDC networks. The proposes approach is a hierarchical control architecture,

inspired by the well established automatic generation control strategy applied to ac networks.

In the proposed architecture, the primary control of the MTDC system is decentralized and implemented using a generalized droop strategy. The concept is based on the combination of a droop control method and dc-bus signaling in order to provide a more generic and flexible control solution that takes into account the states of the network. In this work, different droop characteristics are proposed for the various elements connected to the network. All of them are specifically tailored around five operation bands, which depend on the dc-bus voltage level. Special attention is paid to the integration of energy storage (ES): the state of charge (SoC) is considered at the primary control level, yielding a surface characteristic that depends both on the SoC and the dc-bus voltage.

More than analyzing the behavior of the primary control, this thesis attempts to make a contribution by providing a methodology for designing the various parameters that influence this behavior. The importance of the correct dimensioning of the VSC's output capacitor is underlined, as this element, when set in the context of a MTDC network, becomes the inertial element of the grid and it has a direct impact on the voltage overshoots that appear during transients. Analytical formulas are developed for estimating the voltage peaks during transients and then, it is shown how these values can be used to size the dc-bus capacitor of each VSC connected to the network. Further on, an improved droop control strategy that attenuates the voltage oscillations during transients is proposed. The presented methods are validated on a study case built around a five terminal dc network. Starting from the structure of the network and the power rating of the converters at each terminal, the output capacitors and the primary control layer are designed together in order to ensure acceptable voltage transients.

Also part of the proposed hierarchical control, the secondary control is centralized and it regulates the operating point of the network so that optimal power flow (OPF) is achieved. Compared to other works, this thesis elaborates, both analytically and through simulations, on the coordination between the primary and secondary control layers. This includes the method through which the local primary con-

trollers have to be driven by the centralized controller in order to ensure a smooth transition to the optimal operating point.

Contents

List of Figures

List of Tables

Chapter 1

Introduction

This chapter provides an introduction to the problems and challenges of the modern electrical power system. The integration of energy storage into renewable energy power plants is underlined by the need of providing ancillary services to the grid. The role of dc technology in power systems is also reviewed, as the need for a highly distributed power system that integrates renewable power plants has lately sparked the interest on the topic of multi-terminal dc (MTDC) networks. The objective and the contributions of this thesis in the presented background are described in the latter sections of this chapter.

1.1 Background

The importance of renewable energy in the global electrical production map has evolved in the last twenty years from an optimistic idea to a fast emerging reality. At the moment, wind and solar are still the two most promising renewable energy sources. Wind energy systems are already a mature technology and this can be observed also from the evolution of the wind energy market. According to the last report of the Global Wind Energy Council (GWEC) [1], the market seems to have reached a constant trend. The annual installed capacity reported for each of the last five years is at 39 GW, with small deviations from this value. 2013 with its 35 GW of newly installed capacity ranks considerably low compared to the average, but this is probably due to the peak in installed capacity from the previous year, i.e., 45 GW in 2011.

Meanwhile the wind market is on a constant trend, the photovoltaic (PV) market is growing fast and catching up. The number of PV systems installed last year has exceeded the newly installed wind capacity by more than 3 GW, making 2013 a historical year for PV generation. With 38.4 GW installed in the last year and reaching a global cumulative installed capacity of 138.9 GW, PV generation units now cover 3% of the electrical power demand and 6% of the peak demand in Europe [2].

As the share of renewable energy in the electricity mix increases, grid and market integration challenges are becoming more and more stringent.

1.1.1 Challenges of the modern electrical power grid

The classical structure of the conventional electric power system (EPS) is characterized by a hierarchical architecture with the top layer represented by the central generation system. Worldwide, all the generation capacity at this level lays almost entirely on large central power plants, normally based on fossil fuels, nuclear, and hydraulic power. The generation layer is linked to the utility distribution system through the high-voltage (HV) grid, also known as the transmission grid. This layer is the backbone of the electric grid. Transmission wires, transformers, and control systems are used to send large amounts of electricity over long distances. Most transmission systems use alternating current, though systems based on high-voltage direct current can also be encountered, as it will be seen in the next section. Once the power reaches the distribution substation, it is stepped down in voltage from the high-voltage transmission level to the medium-voltage distribution level. Power generators of smaller rating, typically based on renewable energy, are included at this level. Finally, upon arrival at the service location, the power is stepped down again from the distribution voltage to a lower voltage, depending on the power needs of the final consumer.

The two primary functions of the electricity grid are 1) providing a supply of electric energy and 2) delivering that energy to customers via the transmission and distribution (T&D) system. Additional to these two elementary functions, there are the so-called *ancillary services*, which are defined by the Federal Energy Regulatory Commission (FERC) as "*those services necessary to support the delivery of elec-*

tricity from seller to purchaser while maintaining the integrity and reliability of the interconnected transmission system" [3]. The names, particularities, and specific requirements of each of these services, as well as their financial benefits, might present differences from country to country. For example, a study presented in [4], on data from twelve transmission system operators (TSOs), shows nine different ways of defining the frequency control service. However, despite these small differences, the services imposed by the various TSOs address the same aspects and require, in most cases, for the power plant to be able to actively control and predict its power output. Frequency control (including primary control and inertial response), spinning reserves, supplemental reserves, load following, and dynamic scheduling are some of these services that require output power control from the plant.

At the current moment, as the primary form of energy generation is based on converting fuel to electricity in real-time, providing the above services is a manageable task that has been successfully performed for the past century. However, taking into consideration the global decrease in fuel-reserves and the steep increase in the renewable energy markets, it is just a matter of time until renewable power generators are going to form the majority of the generating units in the grid. Such a scenario is alarming from the point of view of the stability and reliability of the grid. None of the services that require the predictability and controllability of the generated power can be provided when the primary source of energy has stochastic behavior.

Current trends in the electrical power network research propose a new approach towards designing the EPS; the top-to-bottom architecture described previously is being overtaken by new ones based on distributed generators. These generators, included at both the transport and distribution level [5, 6], will have smaller power ratings (0.1 up to 50 MW) and will provide both energy and ancillary services. Such a system, especially if it is based on renewable energy sources, cannot be made possible without adding energy storage (ES) into the system. The concept of energy storage units connected to the electrical-grid was the source of serious research in the past few years and still continues today. A series of studies [3, 7] performed for the Department of Energy of the United States show that the importance of the

storage element in the modern grid is going to increase dramatically in the upcoming years. Analyses of market potential and benefits are being performed in order to provide new business models that will finally drive innovation in the field of electric power systems .

1.1.2 History of the evolution of the dc technology in the context of power transmission

For the past century, ac networks have been established as the standard technology for electrical power transmission systems. However, the dc technology has not disappeared completely from this picture. The capability of dc systems to transmit higher power over longer distances, the possibility of interconnecting asynchronous networks, and their high efficiency, has maintained the interest of both industry and academia. Even though, historically, dc generators and mercury arc rectifiers have been used for dc transmission, for the past five decades, high voltage dc (HVDC) applications were almost exclusively built using line commutated converters (LCC) based on thyristors. More than 145 installations with power ratings ranging up to 7000 MW have been commissioned until 2013 in over 40 countries worldwide, and 40 new projects are planned to be finished before 2020 [8]. In parallel with LCC, a new technology for HVDC applications has emerged in the 90s, with a first 50 MW installation in Gotland, Sweden, in 1999. This new technology uses voltage source converters (VSC) based on IGBTs. A brief overview highlighting key points of the evolution of the dc technology in the context of power transmission, is offered in Fig. 1.1.

While LCC is a mature technology that is successfully used in applications transferring very large amounts of power with high efficiency, it has the drawback of drawing considerably amounts of reactive power and generating a large number of low-harmonics, hence, requiring a strong connection to the ac-network [9]. Moreover, the operation and control of LCC dc networks with more than two terminals has proved to be extremely difficult.

VSCs, on the other hand, can connect to very weak ac-grids. They can provide reactive power and have black start capability. The smaller filters and compensators

reduce considerably the overall footprint of the station, making it ideal for offshore platforms and dense urban environments. Higher losses and smaller power ratings used to be the main disadvantage of the VSC, but advances in multi-modular converters (MMC) are tackling this issue [10].

The fast advances in power electronics, together with the challenges raised by the integration of distributed generation into the modern power grid, have drawn a lot of attention towards VSC multi-terminal dc (MTDC) networks. Daring projects, as the North Sea Supergrid, which proposes to use such a network for integrating the wind power resources of the North Sea in the mainland grids, have fueled the research in the area for the past few years [11–16]. Various topologies and control algorithms for such systems are presented in [13, 14, 17–20]. Also, studies regarding stability [21], [22], [12], protection [23–27], and interaction with the conventional ac grids [28–31], can be found in the literature. Even though the topic of HVDC for the integration of offshore wind farms is the most approached subject in the area, other authors have started to analyze the benefits of lower voltage MTDC grids in other applications, such as railway electrification [32]. Also, according to [33],[34], a modular PV system, based on a common dc bus that allows the integration of ES and dc loads, could be the ideal solution for future microgrid applications. Such a system could offer advantages in terms of efficiency, reliability, and scalability.

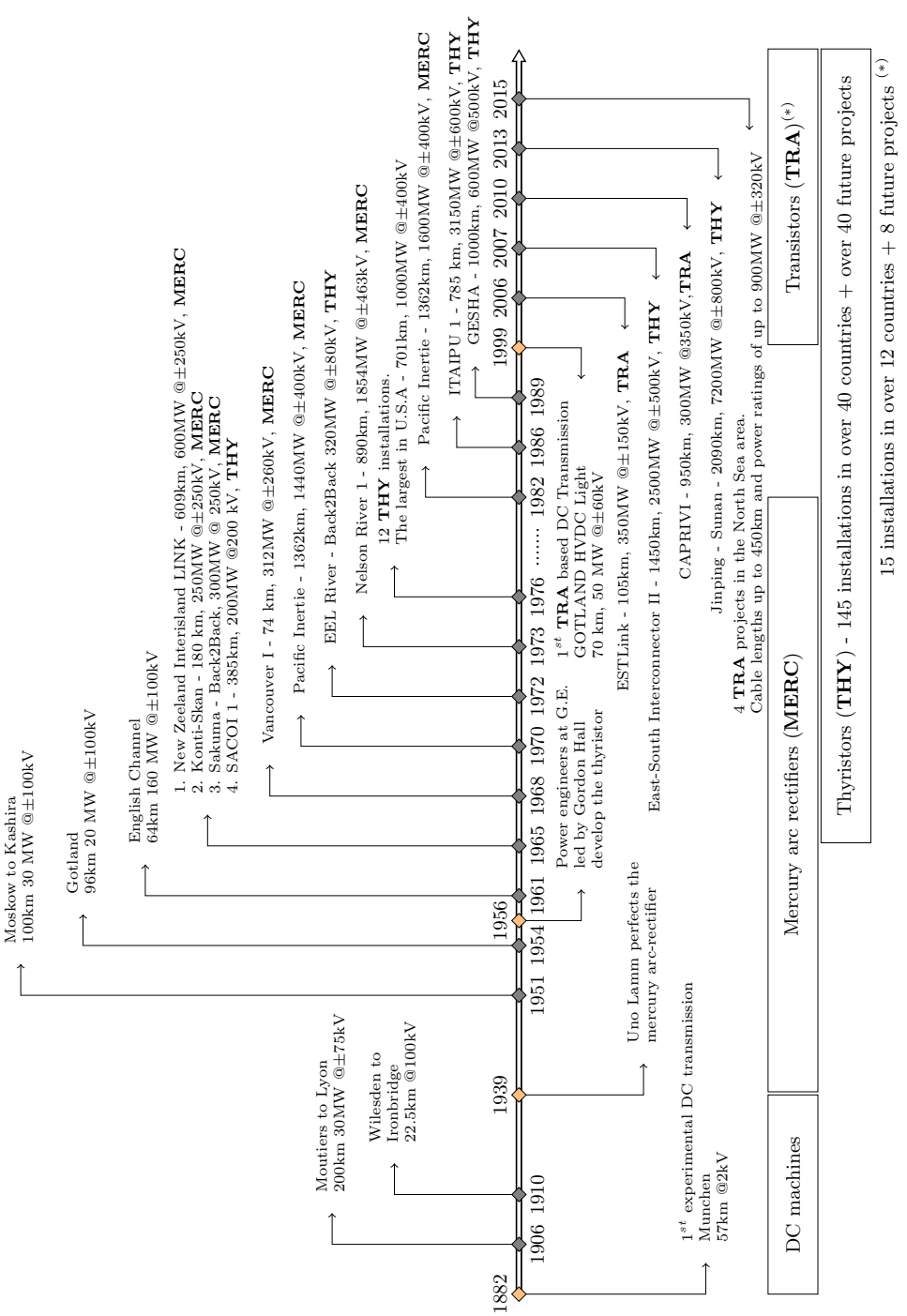

Fig. 1.1: History of the evolution of the dc technology in the context of power transmission

1.1.3 Challenges of dc multi-terminal control

The main control challenge in MTDC systems is the regulation of the dc voltage. This challenge comes from the fact that, in dc systems, the voltage is influenced by the power flow between the elements of the network, as well as by the power imbalance between generation and production. This is the key difference when compared with the well-known ac-systems. In these systems, the power flow is dictated by the voltage-angle differences between the different busses. Meanwhile, the power imbalance influences the frequency, which is a unique parameter throughout the entire grid.

As underlined in [35], there are two options for implementing the control of dc networks. The first one is based on a centralized controller that monitors the entire system through an external communication link and optimally dispatches the loads and the sources. A centralized system has the advantage of being optimal, but the dependence on external communication is a serious drawback. As an alternative to the centralized structure, there are the so-called decentralized control strategies, including master-slave, droop, and dc bus signaling methods [35].

Since currently there are no specific standards that regulate the operation of dc grids, various application-specific approaches, based on combinations of droop and master-slave controllers, are found in the literature, such as in [36–39].

Despite the lack of regulation in this field, it is starting to become clear that the most generic, scalable, and reliable control method for a dc network is a hierarchical approach, similar to the one used in ac grids, as suggested by [40–42]. In this hierarchical approach, the primary layer is decentralized and independent of any communication link. Several decentralized control methods for MTDC grids are identified also in [43]. From these methods, the droop control seems to be the most common voltage control strategy, being used either exclusively[44], or in combination with other voltage control strategies [14]. Meanwhile, the secondary control is centralized and regulates the voltage profile of the network, as well as the basic power flow, by making use of low-bandwidth communication [45–47]. Even though it is inspired by the hierarchical control of frequency in ac-grids, this control strategy is not directly applicable to dc networks. As mentioned earlier, proper

adaptations are required to deal with the fact that voltage amplitude in dc networks, unlike frequency in ac networks, is not a unique parameter.

Another challenging fact in the operation of MTDC networks, and at the same time another argument in favor of decentralized primary control, is the speed of the voltage variations. Conventional power plants connected to the ac network are usually characterized by large inertial constants, in the range of 2 to 10 seconds [48]. These large inertial constants are given by the large amount of energy accumulated in the rotating parts of the electrical generators, which oppose any fast change in frequency. This is not the case when dealing with MTDC networks. The active element in this scenario is the VSC converter, and its output capacitor becomes the only inertial element of the network. While very large capacitors would be desirable from the inertial point of view, the large short-circuit currents impose difficult requirements for the protection system. Therefore, small capacitors with time constants in the range of milliseconds are typically used [49]. With almost no inertial element to oppose them, the voltage transients in a dc network will be very fast when compared to the frequency transients in ac-network.

1.2 Project objectives and outline of the thesis

This thesis presents the work performed while carrying out my PhD studies at the SEER (Sistemas Elèctricos de Energia Renovable) research center, during the three-year period between 2011 and 2014. While working at SEER, I was initially involved in the PAPE (Procesamiento Avanzado de Potencia y Energía) project, which is a joint collaboration between Abengoa Solar and SEER, with the purpose of creating original theoretical and practical knowledge on cutting-edge PV power plants that include energy storage. The project was divided into two main directions. One was focused on the ac-side of the converter, studying problems related to control architectures that enable the dc-ac converter connected to the PV power plant to behave similarly to a synchronous generator in terms of grid support. Meanwhile, the other research line, covered in this thesis, was directed to the dc side of the converter. Initially, aspects regarding to the integration of energy storage in grid-supporting PV

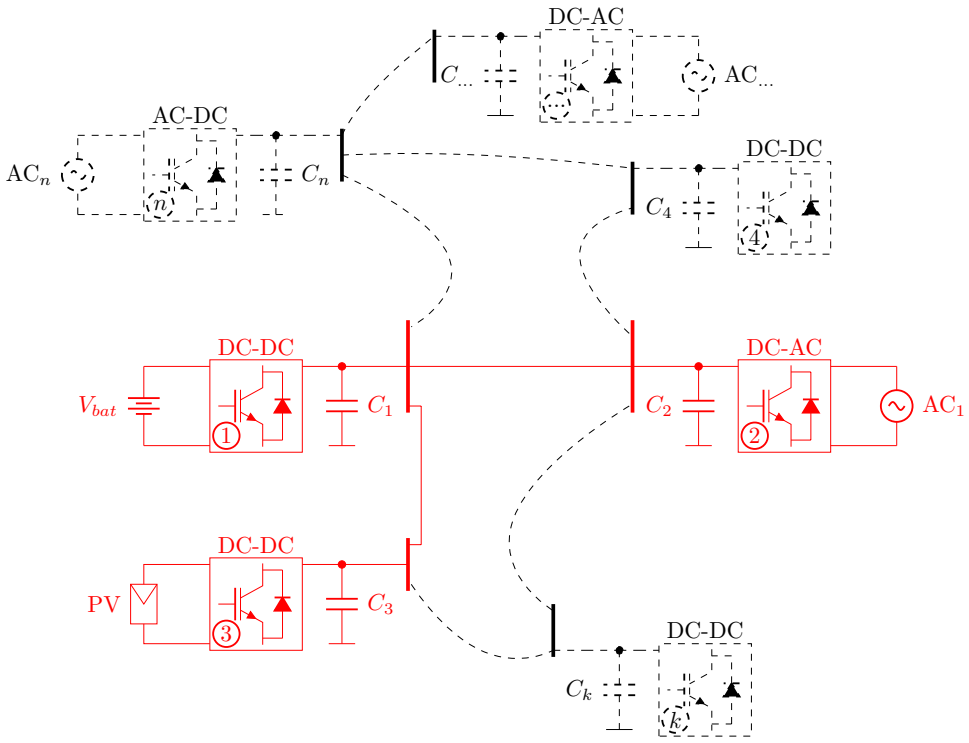

Fig. 1.2: Evolution of the thesis objectives from grid-supporting power plants to control of MTDC networks

power plants were addressed. Further on, as it can be seen in Fig. 1.2, while trying to evaluate how the dc side of the system can be managed when more elements are added to the network, the focus of the thesis evolved from the control of three elements connected to a common dc bus, to the control and operation of a generic MTDC network.

The present document is structured as follows. Chapter 2 describes the first aspects covered in the PAPE project, mainly those regarding grid-supporting PV power plants. Here, we will show the basic structure of the power plant and we will present the control strategy for the two main converters, i.e., the dc-dc converter connected to the energy storage element and the dc-ac converter connected to the ac grid. Aspects regarding the sizing of the storage element depending on the services that the plant has to provide to the ac-grid, are also considered in this chapter. The

presented methods were validated on a scaled 10 kW laboratory prototype and some of the results will be detailed here.

The following chapters, starting with Chapter 3, deal with aspects regarding the control and operation of MTDC networks on a larger scale. For this, we proposed a hierarchical control structure, similar to the one used for the control of ac-grids. In this control strategy, the primary control layer is decentralized and implemented locally in each converter. Meanwhile, the secondary control is centralized and is based on low bandwidth communications. Chapter 3 presents the primary control that we propose, which is based on a generalized droop control, built around five different operating voltage bands. Here, we propose various droop characteristics for each connected element, depending on their role in the operation of the network.

Aspects regarding the design of the elements involved in primary control are treated in details in Chapter 4. Here, we propose a methodology for sizing together the parameters of the primary control, such as: the voltage operating bands, the dc bus capacitor, the droop gain, and the speed of the current controller, by analyzing the voltage transients of the network.

Chapter 5 presents the secondary level of our hierarchical control architecture. The secondary control is a centralized controller and acts like a supervisory control and operation optimizer. After a network contingency or a load change, the primary control will act instantaneously, trying to control the voltage of the network. However, given the inherent proportional behavior of the droop control, the operating point of the network will deviate from its initial state. The secondary control periodically re-evaluates the operating point of the network and, when a better option is found, it computes new references for the primary control, in order to bring the network to the new operating point.

Finally, the conclusions of the thesis and the ideas for future work are presented in Chapter 6.

1.3 List of publications and contributions

Some of the results of this research work were published or are under review for publication in various journals and conference proceedings. These publications are listed below.

1. **Gavriluta, C.**; Candela I., Citro, C.; Luna, A.; Gomez-Exposito, A.; Rodriguez, P., "Hierarchical Control of HV-MTDC Systems with Droop-Based Primary and OPF-Based Secondary", Smart Grid, IEEE Transactions on – *Accepted for publication*

2. **Gavriluta, C.**; Candela, I.; Rocabert, J.; Etxeberria-Otadui, I.; Rodriguez, P., "Storage system requirements for grid supporting PV-power plants ," Energy Conversion Congress and Exposition (ECCE), 2014 IEEE, 14-18 Sept. 2014

3. **Gavriluta, C.**; Candela I., Citro, C.; Luna, A.; Rodriguez, P., "Design Considerations for Primary Control in Multi-Terminal VSC-HVDC Grids", Electric Power Systems Research – *Under review*

4. **Gavriluta, C.**; Candela I., Luna, A.; Rocabert, J.; Rodriguez, P., "Adaptive Droop for Control of Multi-Terminal DC-bus Integrating Energy Storage," Power Delivery, IEEE Transactions on – *Accepted for publication*

5. Rouzbehi, K.; **Gavriluta, C.**; Candela, J.I.; Luna, A.; Rodriguez, P., "Comprehensive analogy between conventional AC grids and DC grids characteristics," Industrial Electronics Society, IECON 2013 - 39th Annual Conference of the IEEE,10-13 Nov. 2013

6. **Gavriluta, C.**; Candela, I.; Luna, A.; Rocabert, J.; Rodriguez, P., "Adaptive droop for primary control in MTDC networks with energy storage," Power Electronics and Applications (EPE), 2013 15th European Conference on, 2-6 Sept. 2013

7. **Gavriluta, C.**; Candela, I.; Citro, C.; Luna, A.; Rodriguez, P., "Decentralized control of MTDC networks with energy storage and distributed gen-

eration," Energy Conversion Congress and Exposition (ECCE), 2013 IEEE, 15-19 Sept. 2013

8. **Gavriluta, C.**; Candela I., Luna, A.; Rocabert, J.; Rodriguez, P.,"Adaptive Droop for Primary Control in MTDC Networks with Energy Storage", EPE Journal – *Accepted for publication*

9. **Gavriluta, C.**; Candela, I.; Citro, C.; Rocabert, J.; Rodriguez, P., "Decentralized Primary Control of MTDC Networks with Energy Storage and Distributed Generation," Industry Applications, IEEE Transactions on – *Accepted for publication*

10. **Gavriluta, C.**; Citro, C.; Nisak, K.; Beltran San Segundo, H., "A simple approach for fast controller prototyping for a three phase interleaved DC-DC converter," Industrial Electronics (ISIE), 2012 IEEE International Symposium on, 28-31 May 2012

11. Citro, C.; **Gavriluta, C.**; Nizak, M.H.K.; Beltran, H., "Current control design for three-phase grid-connected inverters using a pole placement technique based on numerical models," Industrial Electronics (ISIE), 2012 IEEE International Symposium on, 28-31 May 2012

12. **Gavriluta, C.**; Spataru, S.; Mosincat, I.; Citro, C.; Candela, I.; Rodriguez, P., "Complete methodology on generating realistic wind speed profiles based on measurements," International Conference on Renewable Energies and Power Quality (ICREPQ), 28-30 March 2012

Chapter 2

Primary Control of MTDC Networks

This chapter shows how the focus of the thesis has expanded from the control of three elements connected to a common dc bus to the control of a generic multi-terminal dc network. The chapter starts by providing an overview of the control techniques available in the literature, then it presents the proposed control strategy. We adopted a hierarchical approach to tackle the problem of MTDC control and this chapter describes the operation of the proposed primary control. Various droop characteristics are designed for the different elements connected to the dc network in an attempt to extend the classic concept of droop control to a more generic control approach.

2.1 Overview of control strategies for MTDC networks

Before analyzing the various control strategies proposed in the literature for MTDC networks it is useful to take a short glance at how ac networks are controlled as most of the authors extend these concepts also for dc networks.

2.1.1 Similarities between ac and dc networks

The overall control task in the ac electric power system, or in any power system for that matter, is to maintain the balance between the electric power produced by the generators and the power consumed by the loads, including the network losses, at every moment. In ac systems this is achieved through the Automatic Generation

Control (AGC), which is a hierarchical control strategy composed of three layers, as shown in Fig. 2.1 [50]. From these three layers only the primary and secondary control are of interest when analyzing the dynamics of the system. This is due to the slow reaction time of the tertiary reserves – more than 15 minutes, according to ENTSO-E [51]– which are dispatched according to economic offline optimizations algorithms. Tertiary control is manually activated and supports the system operator in the process of releasing the used primary and secondary control reserves after a disturbance.

The primary control layer is decentralized and implemented locally as a proportional controller in each power plant that participates in frequency regulation. This proportional gain, also known as the speed-droop characteristic, or the P-f droop characteristic, determines the ratio between the deviation in frequency Δf and the change in the reference power ΔP_m^{set} sent to the internal controller of the turbine as seen in Fig. 2.2 [48, 50, 52]. Implementing the primary control in this manner has the great advantage that multiple generators can be connected in parallel without them competing each other for the control of frequency.

After the primary control has acted, the secondary control adjusts the power setpoints of the generators in order to compensate for the steady state frequency error, caused by the proportional behavior of the primary control. On top of canceling the frequency error, the secondary control has to correct another undesired effect that appears in interconnected systems: active power imbalances and primary control actions cause changes in the load flows on the tie-lines to other areas, i.e., power exchanges not according to the scheduled transfers between the areas. The secondary control ensures through an integral controller that this aspect is remedied after a short period of time.

When a difference between load and generation occurs, the frequency will experience various changes at different time-scales depending on which of the control layers is active. The first step, which is not immediately visible from the diagram of Fig. 2.1, but is of critical importance for the operation of the system, is the inertial response. This occurs during the first frequency transient, even before the action of the primary control, and it involves the power imbalance being compensated by the

kinetic energy stored in the rotating parts, rotor and turbines, of the generator. This causes the speed of the generator to change, which in turn results in a frequency change. If the imbalance is too large and the frequency starts to deviate from its nominal value, the primary control becomes active and the power supplied from the generators is changed accordingly to their P-f droop characteristics.

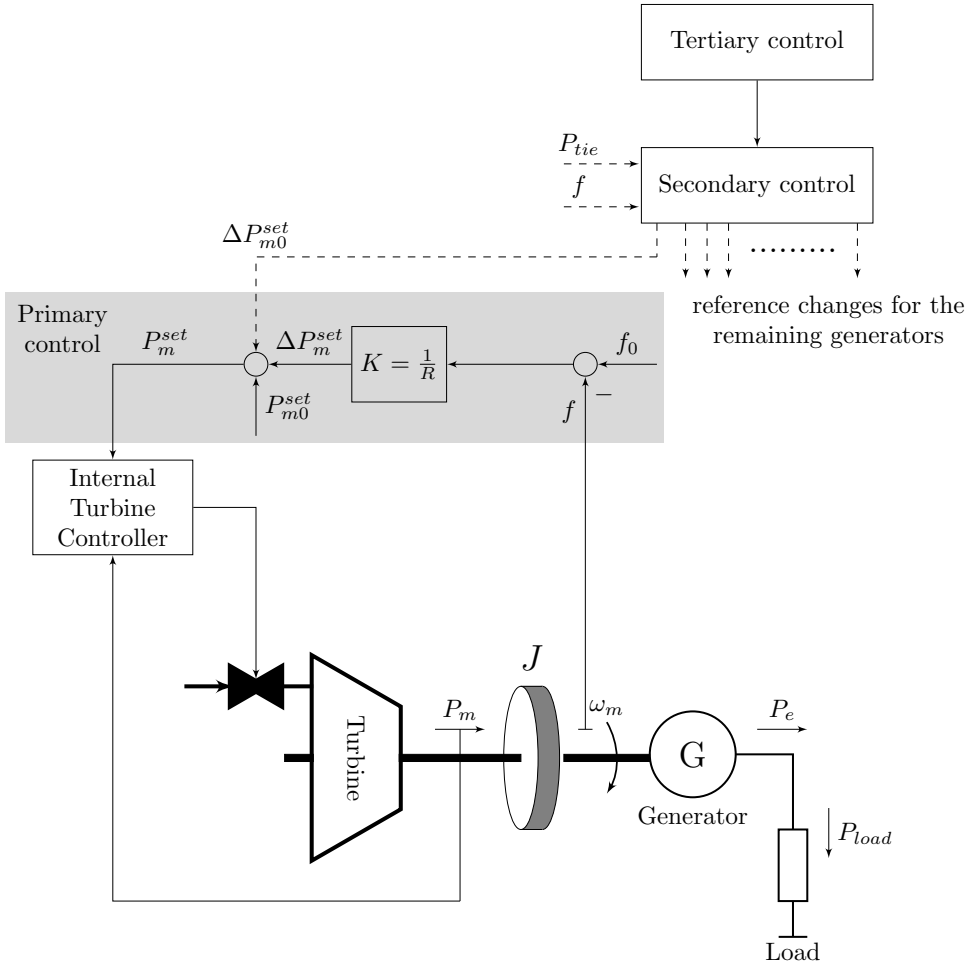

Fig. 2.1: Conceptual view of the control layers involved in the automatic generation control of ac networks.

The inertia J of the generator can be seen as an energy buffer that has to supply

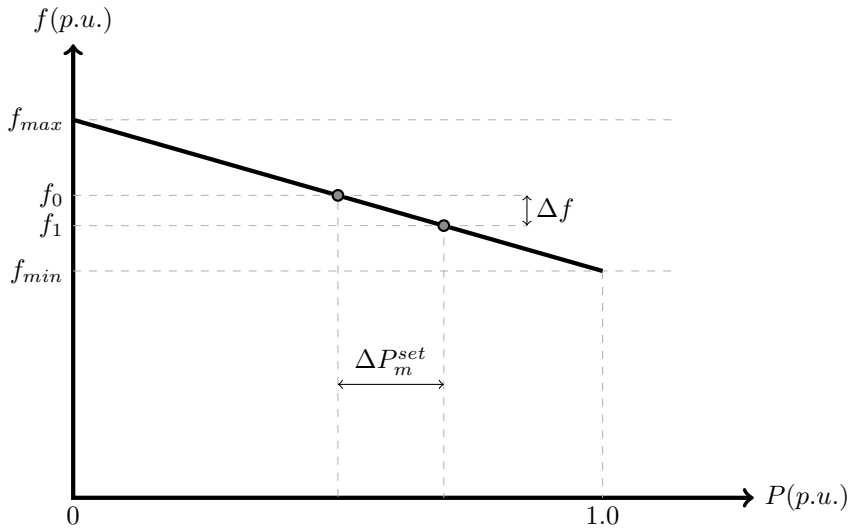

Fig. 2.2: P-f droop characteristic used in the primary control of ac power plants.

the difference between the electrical power P_e and the mechanical power P_m until the primary control has time to react and change P_m accordingly.

In order to better understand the basic dynamic characteristics of the frequency, the swing equation of the generator is presented in (2.1). Here, H_{ac} is the so-called *inertial constant* and represents the ratio between the energy stored in the rotating mass at nominal speed ω_0 and the nominal power of the machine S_B, as shown in (2.2). The unit for H_{ac} is seconds and can be interpreted as the time needed for the rotating parts of the generator to arrive from nominal speed to a full stop when the difference between P_m and P_e is equal to the rated power of the machine.

$$\frac{d\omega}{dt} = \frac{\omega_0^2}{2 \cdot H_{ac} \cdot S_B \cdot \omega} (P_m - P_e) \tag{2.1}$$

$$H_{ac} = \frac{0.5 \cdot J \cdot \omega_0^2}{S_B} \tag{2.2}$$

If the non-linear frequency dynamics described in (2.1) were to be linearized around the nominal operating point, and expressed in terms of deviations in frequency f rather than angular velocity ω, then the relationship shown in (2.3) is

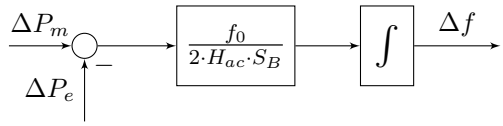

Fig. 2.3: Block diagram of linearized frequency dynamics as in (2.3)

obtained. The block diagram of this relationship is shown in Fig. 2.3; the difference between the deviation in mechanical power and electrical power is first scaled by H_{ac} and then integrated in order to obtain the deviation in frequency. If the internal turbine controller is slow, and it takes a long time for the primary to act on P_m, then a large inertial constant is required in order to limit the variation in frequency.

$$\dot{\Delta f} = \frac{f_0}{2 \cdot H_{ac} \cdot S_B} (\Delta P_m - \Delta P_e) \tag{2.3}$$

It is interesting to note that the dynamics of the generator frequency are very similar to the one of the voltage at the dc output of a power converter. Using the automatic generation control of the ac networks as an example, it is not difficult to imagine the analogy shown in Fig. 2.4. Here, the generator is replaced by the power converter and the inertial element becomes the dc bus capacitor C. Before, the time constant of the internal turbine controller was affecting how fast the mechanical power will follow its reference. In this case it will be the internal current or power controller of the converter that will determine how fast the converter can inject power into the capacitor.

Stretching the notation for the sake of analogy we maintained the terms P_m and P_e to mark the power flowing in and out of the inertial element, which in this case is the dc bus capacitor. Then, the equation of the voltage across the capacitor can be written as shown in (2.4). The term H_{dc} appearing in (2.4) is not an established concept as H_{ac}, but given its expression in (2.5) we can call it the *inertial constant of the dc bus capacitor*. Once again the unit for H_{dc} is seconds and it represents the ratio between the energy stored in the capacitor at nominal voltage V_{dc0} and the nominal power of the converter S_B.

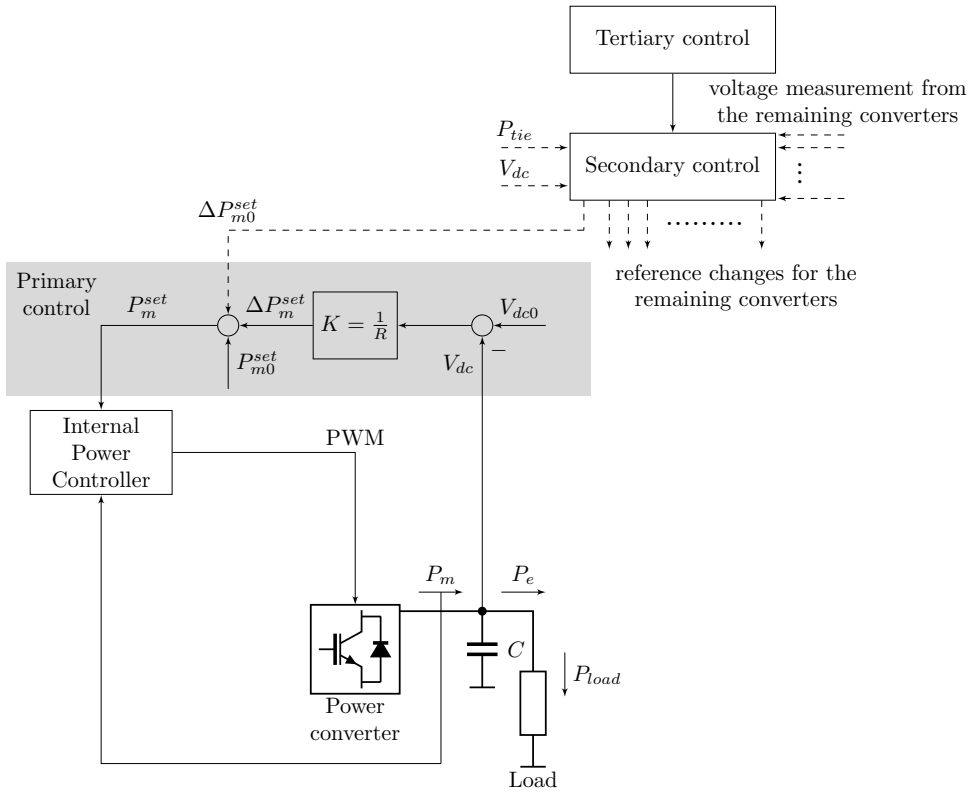

Fig. 2.4: Conceptual view of the control layers involved in the hierarchical control of dc networks

$$\frac{dV_{dc}}{dt} = \frac{V_{dc0}^2}{2 \cdot H_{dc} \cdot S_B \cdot V_{dc}} (P_m - P_e) \tag{2.4}$$

$$H_{dc} = \frac{0.5 \cdot C \cdot V_{dc0}^2}{S_B} \tag{2.5}$$

As before, linearizing the non-linear voltage dynamics shown in (2.4) around the nominal operating voltage we obtain the relationship shown in (2.6) and Fig 2.5.

$$\Delta \dot{V}_{dc} = \frac{V_{dc0}}{2 \cdot H_{dc} \cdot S_B} (\Delta P_m - \Delta P_e) \tag{2.6}$$

Given the similarity between the frequency dynamics (2.1) - (2.3) in ac systems

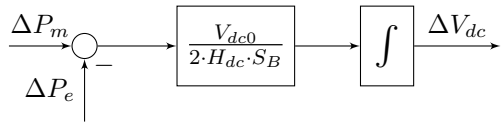

Fig. 2.5: Block diagram of linearized voltage dynamics as in (2.6)

and the voltage dynamics (2.4) - (2.6) in dc systems, it also makes sense to try to apply the same control strategy that is used in ac networks in order to manage the dc networks.

However, this extrapolation is not immediate. In ac systems the sinusoidal voltages are characterized by three distinct quantities: amplitude, frequency, and phase. From these three parameters, voltage amplitude is related to reactive power while frequency and phase are directly linked to active power. Frequency is a unique parameter for the whole grid and reflects the imbalance between active power production and consumption. Meanwhile, the phase angle at each bus is different according to the power flow of the network.

On the other hand, the voltage in dc systems is characterized only by a single parameter, i.e., the voltage amplitude. There is no reactive power to take into account in dc systems; but the fact that both the power flow and the power balance of the grid are reflected in the amplitude of the voltage makes it difficult to use exactly the same control strategy as for ac grids.

Another important aspect that also needs to be pointed out when discussing the differences between ac systems and dc systems is the large difference between the inertial constants. According to [48] values for H_{ac} up to 8-10 seconds are typical for large machines connected to the grid. To obtain similar values for H_{dc} would require either an enormous capacitor, either a very high operating voltage for the network. The inertial time constant for the dc grids would typically be in the range of ms [49]. This will require fast controllers for the power converters involved in the primary control.

2.1.2 Control strategies for MTDC networks

The interest of both academia and industry towards MTDC grids is mainly being fueled by the North Seas Countries' Offshore Grid Initiative, which from 2010 is on a mission to find the most suitable way for integrating over 100 GW of planned offshore wind power plants into the mainland grids [16, 42]. Work on MTDC networks for wind integration is the main subject being approached in the literature [11, 15, 18, 20, 25, 28, 53, 54], and the concept of MTDC has started to automatically be associated with HVDC systems. However, proposals for MTDC systems can also be found at lower voltage levels for applications related to photovoltaic power generation systems, microgrids, or other applications such as railway electrification [32]. According to [33, 55] a modular PV generation system based on a common dc bus that also allows the integration of energy storage (ES) and dc loads could be an attractive solution for future microgrid applications. Such a system could offer advantages in terms of efficiency, reliability, and scalability.

The main control challenge in a MTDC system is the one of the dc voltage, which, as seen in the previous section, is directly related to the power balance between the elements of the network. Various control strategies can be found in the literature for MTDC networks of different sizes, but not all of them are easy scalable. For starters, there are two main options for controlling the dc voltage, as underlined in [35]. The first one is based on a centralized controller that monitors the entire system through an external communication link. This system has the advantage of optimality as a tradeoff for the dependence on the external communication link. As it was mentioned in the previous section, the dynamics of the dc grid are very fast, therefore this type of control is not suitable for geographically distributed power systems and is more commonly found in small UPS systems [56] or for the parallel operation of converters in microgrids [57].

As an alternative to the centralized structure, there are the so-called decentralized control strategies, including droop controllers and dc bus signaling methods. A good review of these strategies, as they apply to the control of HVDC grids, is presented in [43]. The decentralized control strategy is quite popular in the literature. Several examples based on droop controllers, dc bus signaling or combination

of both can be found for low voltage applications [33, 36–38, 55, 58] but also for high voltage applications [14, 44–46, 59]. From the distributed control strategies, droop control has been acknowledged in the literature as a good candidate for implementing the primary control in large MTDC networks. This is mainly due to the fact that the system controlled in this way is easy scalable. New elements can be added without having to reconfigure the ones that are already connected. This control strategy is already the standard in the primary control of ac grids and is highly appreciated for its simplicity and robustness.

A more powerful approach for the control of MTDC networks can be achieved by combining the two previously described control methods, centralized and decentralized, in a hierarchical structure as shown in the previous section when following the analogy between dc and ac grids. In an attempt to standardize the control of MTDC networks, a hierarchical control architecture is proposed in [40, 42], and this idea is also brushed on in [46, 60]. In this approach the primary layer of control is decentralized while the upper layers, based on low bandwidth communication, manage the system.

While the topic of primary or secondary control in dc networks has been addressed before in the literature in one way or another, every time there are important aspects that are left out of the discussion. For example, papers that approach the topic of primary control do not address the sizing of the elements involved in the primary control, such as: the speed of the internal current loop of the converter, the size of the capacitor, the droop constant, or the operating voltage interval of the network. In a similar way, the works that address the secondary control limit themselves to steady state analysis and do not approach the interaction between the primary and secondary control.

The work presented in this thesis tries to remediate these aspects. For this, we start by proposing in this chapter a new approach for the primary control of dc networks. The operation principles of such a system are explained and validated through simulations and experimental results on low voltage systems. Then, in the next chapter we address aspects related to the sizing of all the parameters involved in the primary control, taking as a study case a meshed high voltage MTDC network

proposed in [61] for the integration of wind power. Finally, in Chapter 4, we propose and implement a secondary control algorithm that manages the network by properly driving the primary control.

2.2 Primary control

Similar to ac systems, in a hierarchical control structure for MTDC networks, the lowest control level, namely the primary control, should be able to operate independently and maintain the system operational and stable without making use of external communication channels. However, while in ac grids the frequency is a global and unique parameter, based on which the primary control is implemented, dc grids do not have a similar parameter. A generator connected to the ac grid will sense changes in the power balance of the network just by analyzing the variations in the frequency. If the grid is loaded, the frequency will start to decrease and, given the global nature of this parameter, all the connected elements will sense the same change regardless of their position relative to the load. Therefore it is easy to implement a distributed control strategy based on the frequency, and as it is well known, droop-controllers that establish linear relationships between frequency variations and power injection are the standard [51] for managing generators that participate in the primary control of the ac grid.

However, this is not the case for dc power systems. In dc grids there is no power flow without voltage deviation between the nodes. Therefore, the voltage at the terminals of each converter has to be allowed to vary slightly around the nominal value in order for the network to be able to transfer power. Also, because information regarding both power-flow and power-balance are reflected in the network voltage, typically an element connected to the dc grid will not be able to sense the state of the entire network just by measuring the voltage at its terminals. The concept of droop control can be extended from ac networks to dc networks, only now the state of the network is not characterized by a single parameter which is the frequency, but rather by the voltage profile of the entire network. The different voltage levels at each dc bus can be used as a global decision parameter and the control actions can be taken

locally based on this value.

The method that we propose for the primary control starts by defining different operating intervals in the dc bus voltage. According to [51] the frequency in the ac grids is allowed to vary 5% around its nominal value. These limits are given by the safe operation of the synchronous generators, and if the frequency goes below 47.5 Hz and above 52.5 Hz the generators will automatically disconnect due to the action of their protective relays. Similarly, upper and lower bounds are to be expected for the dc grid, these limits being imposed by the safe operation of the VSCs connected to the grid. For example, the upper critical limit of the dc voltage V_{dc}^{ch} might be imposed by the over-voltage rating of the VSC, meanwhile the lower limit V_{dc}^{cl} can be imposed by the voltage at which the converter enters in over-modulation. How these limits are established is an aspect related more to safety and manufacturing and is not of great importance for the purpose of the thesis. What is important is that these two limits should be established and they should be the same for all the elements connected to the network.

Once the critical operation limits have been established, five operating bands are defined between these limits and around the nominal dc voltage V_{dc}^{n} as seen in Fig. 2.6. We divided the operating bands surrounding the nominal voltage in three categories: normal operation, safety, and critical. This choice was inspired by the classification of power system operating states used in ac networks, as proposed by CIGRE Report No. 325: normal, alert, and emergency [50]. The first one is the normal operation (NO) band and is the interval allowed for the natural voltage deviations that appear in the network as a result of power flowing through the resistive lines. When the voltages at all the network busses are within this band as shown in Fig. 2.6, the system is considered to be under standard operation with the balance between generation and consumption being satisfied.

The NO band is surrounded by two safety bands; one in the lower part, namely safety low band (SL), and one in the higher, namely safety high band (SH). These bands are considered for the cases of transients or other sudden events that deflect the dc voltage from the NO band for short periods of time. Ideally, the network should not operate for long periods of time in this voltage band. However, as it

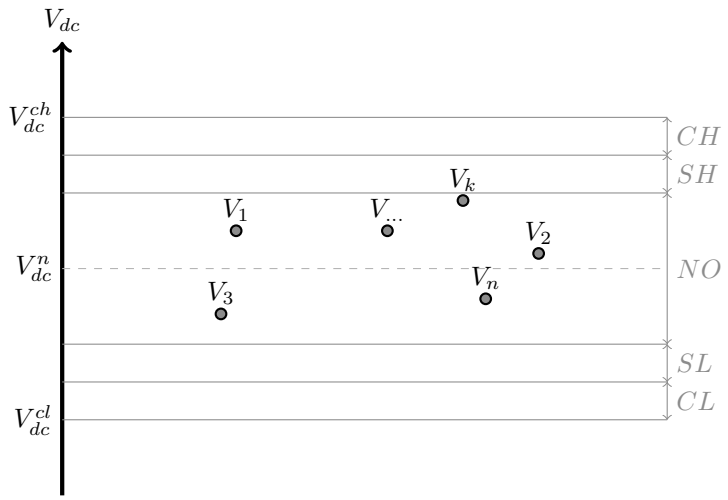

Fig. 2.6: Voltage operating bands for the dc network. All the bus voltages in the NO band - the system is considered to be under standard operation

will be seen from the presented study cases, if this happens, it indicates either a contingency in the network or a depletion of the energy reserves.

Finally, a critical high band (CH) and a critical low band (CL) are considered. When the voltage at the output terminals of an element connected to the dc network reaches these bands, there is a serious mismatch between production and consumption that can no longer be supported by the actual structure of the network. Such a large voltage deviation is no longer a sign of normal power flow in the network and corrective actions have to be taken.

Once the five operating bands have been defined as a base-framework, the control of each element connected to the grid has to be designed so that the overall network operates as intended, i.e., during normal power flow the voltages of the network remain in the NO band, the transient voltages do not surpass the safety bands, and finally, the voltages arrive in the critical bands only during contingency scenarios or under serious imbalance between production and generation.

In the following subsections we will show that by cleverly defining various droop characteristics – designed around the five operating bands – for the main elements encountered in the dc network, a flexible primary control that satisfies the

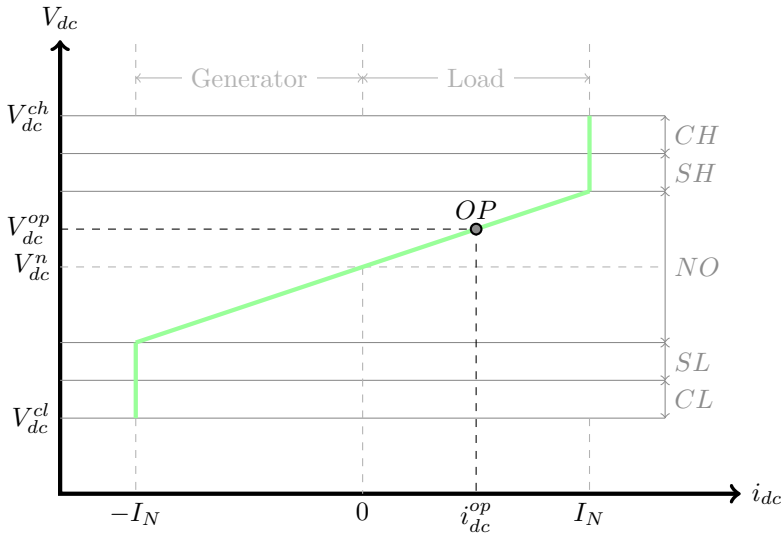

Fig. 2.7: Droop characteristic for bidirectional non-critical element.

operation requirements of the dc grid can be achieved. A detailed mathematical approach for sizing the operating bands together with the primary control is presented in the next chapter. Meanwhile, in this chapter, we will try to clarify, by means of both simulation and experimental scenarios, how the primary control operates, and how a network controlled by these advanced droop characteristics will remain operational even for contingency scenarios such as: trip of convertor, saturation of energy storage, depletion of energy reserves, etc.

2.2.1 Bidirectional droop

Before analyzing each of the droop characteristics, a convention for the signs of the currents has to be set. Throughout this thesis a positive current is considered to be a load current and goes out of the dc bus, while a negative current corresponds to generator behavior and enters the dc bus. This aspect is highlighted above the graph of the droop characteristics, as shown, for example, in Fig. 2.7. A converter that operates in the negative-current region will be seen as a generator by the grid, while one operating in the positive-current region will be seen as a load.

The droop characteristic presented in Fig. 2.7 is the one proposed for generic

bidirectional, non-critical elements. Bidirectional refers to the fact that such a unit can process power in both directions, therefore it can behave both as load and generator. The term non-critical refers to the behavior of such a unit with respect to its power reference. While the dc voltage is in the NO band, a unit using this type of droop control would alter its current output linearly with the increase or decrease in the voltage. If the voltage is in the safety or critical bands then also the current output is at its limits, as seen in Fig. 2.7. Such an element could be a power converter connected to an energy storage unit, or to a strong ac grid. These types of units are the ones that are mainly responsible with the regulation of the dc bus voltage.

There are two options for defining the droop characteristics in a dc system. According to [43] the control scheme can either be current-based, i.e., I-V droop characteristics, or power-based, which is equivalent to a P-V droop characteristic. As seen in Fig. 2.7 we opted for an I-V characteristic because it reflects linear control behavior, in the sense that a voltage deviation will result in an equivalent proportional current deviation. The voltage-power relation is non-linear (parabolic) and when analyzed in control problems it has to be linearized, which in turn will yield an approximate I-V relationship.

Some of the particularities of this curve that need to be highlighted are summarized below:

- at nominal dc voltage V_{dc}^{n} the current absorbed or injected is equal to zero

- in the NO band a proportional behavior is exhibited, emulating a virtual resistance of r_d as seen in (2.7), where NO is the height in volts of the normal operation band and I_N is the nominal current of the converter. As can be seen in the example shown in Fig. 2.7, if the voltage reaches the steady state operating point V_{dc}^{op}, which is above the nominal dc voltage V_{dc}^{n}, the converter will operate as a load and will discharge the dc bus by changing its reference to

the positive current i_{dc}^{op} in an attempt to stop the increase in the voltage.

$$\begin{aligned} i_{dc}^{op} &= \frac{V_{dc}^{op} - V_{dc}^{n}}{r_d} \\ r_d &= \frac{NO/2}{I_N} \end{aligned} \tag{2.7}$$

- in the safety and critical bands the current saturates to the nominal values of the converter.

A converter controlled by this type of droop characteristic will try to compensate any voltage deviation by injecting or absorbing current. By the time the voltage reaches the safety bands, the converter has done all that it was possible in order to try to maintain the voltage in the NO band, and is now operating at full power.

2.2.2 Droop surface for energy storage (ES)

When applying the previous control strategy for interfacing batteries, or other ES with similar behavior, an important aspect that has to be taken into account is that the amount of power a battery is able to deliver or absorb is directly linked to its state of charge (SoC). A battery that is close to being discharged will be able to deliver only a small amount of power, but it can absorb nominal current. Similarly, when close to being fully charged, current can no longer be injected into the battery, but it can be extracted. This behavior can be seen as if the limits I_N and $-I_N$ from Fig. 2.7 change with the SoC of the battery.

Considering the typical operation of a battery, two intervals, depending on the SoC, can be identified. The first one, $[SoC_{h1}, SoC_{h2}]$, is the range where the battery exhibits a high state of charge and current can no longer be injected, therefore I_N is constrained. The second one, $[SoC_{l1}, SoC_{l2}]$, is the SoC interval for which the battery is considered to be in a low state of charge. In this case the battery can not support the grid by injecting current, hence $-I_N$ is limited. It is considered that

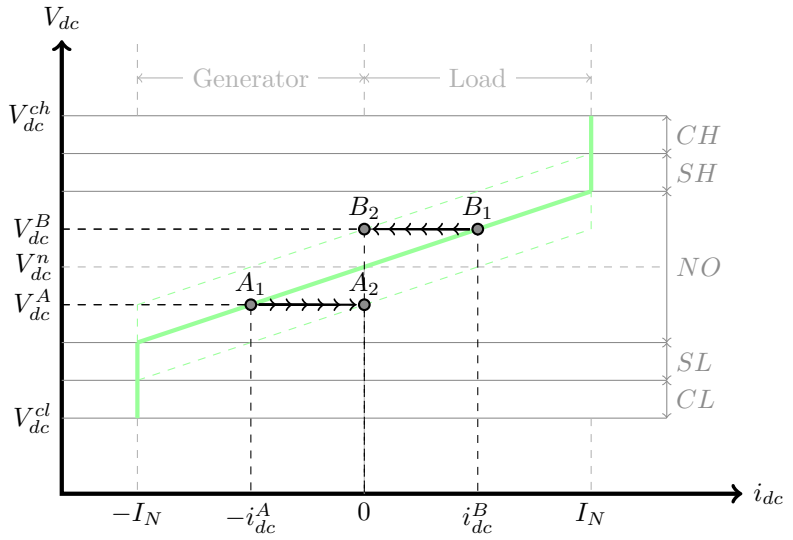

Fig. 2.8: Droop characteristic for energy storage element.

outside of these two SoC intervals the battery can circulate nominal current in both directions, hence there are no restrictions in neither I_N nor $-I_N$.

In order to account for this behavior we included the SoC in the definition of the droop characteristic. This was done by using the SoC to control the vertical offset of the droop, as seen in Fig. 2.8. Mainly, the voltage level for which the converter injects zero current, i.e., operating point $\left(V_{dc}^{0}, 0\right)$, is defined as a function of the SoC as shown in (2.8). The droop characteristic becomes a surface defined by SoC and the dc voltage, as shown in Fig. 2.9. From the terms present in (2.8), V_{dc}^{n} is the nominal voltage of the network, while V_{dc}^{ch} and V_{dc}^{cl} are the maximum and minimum voltage levels defined in the previous sections.

$$V_{dc}^{0} = \begin{cases} V_{dc}^{n}, & SoC \in [SoC_{l1}, SoC_{h1}] \\ \min\left(\frac{SoC - SoC_{h1}}{SoC_{h2} - SoC_{h1}} \cdot \left(V_{dc}^{ch} - V_{dc}^{n}\right) + V_{dc}^{n}, V_{dc}^{ch}\right), & SoC \geq SoC_{h1} \\ \max\left(\frac{SoC - SoC_{l2}}{SoC_{l1} - SoC_{l2}} \cdot \left(V_{dc}^{n} - V_{dc}^{cl}\right) + V_{dc}^{cl}, V_{dc}^{cl}\right), & SoC \leq SoC_{l1} \end{cases} \tag{2.8}$$

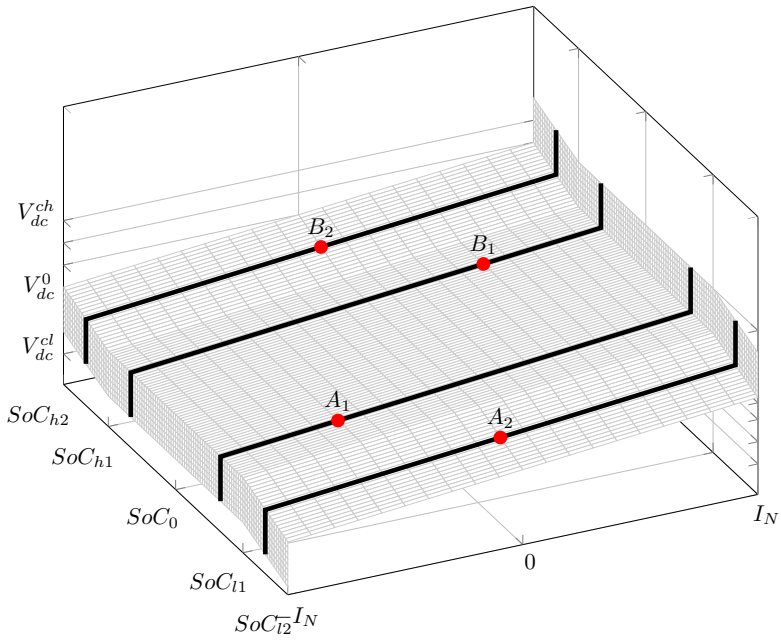

Fig. 2.9: Droop surface for energy storage elements

The $SoC - V_{dc}$ droop-surface used for the control of the VSC connected to the ES inherently includes at the primary control level a protection mechanism against the overcharge and deep-discharge of the battery. Looking at the way the droop is designed, the SoC of the battery will never go below SoC_{l2} or above SoC_{h2}.

Fig. 2.8 can be seen as a cross-section of the $SoC - V_{dc}$ droop-surface. Two operating scenarios, also shown in Fig. 2.9, are highlighted here. In the first one, the converter connected to the battery operates at point A_1, discharging the battery at a rate equal to $-i_{dc}^{A}$. As time goes on and the discharge continues, the SoC of the battery will eventually reach the SoC_{l1} limit.. According to Fig. 2.9 at this point the converter starts to linearly shift its droop characteristic downwards, limiting the amount of power extracted from the battery. If there are other elements in the network that can compensate for this reduction in power, V_{dc} will remain at the same level and the converter will reach A_2, where no more current is allowed to be drawn from the battery as seen in Fig. 2.8. In the case that there are no other elements to compensate for the reduction in power, then, as it will be seen in the simulation

and experimental results, V_{dc} will linearly decrease and will enter the CL operating band. In both cases, the SoC of the battery will not decrease bellow SoC_{l2}, therefore ensuring protection against deep discharge.

The second operating scenario starts with the converter operating at point B_1, charging the battery with a current equal to i_{dc}^{B}. Similar to the previous scenario, as the charging continues, the SoC reaches SoC_{h1} and the converter starts to push its droop characteristic upwards, as seen in Fig. 2.9. If the dc bus voltage is maintained at the same level, the converter reaches B_2 where it reduces the current injected into the battery to zero. As before, the dependence of the droop surface on both SoC and V_{dc} will never allow for the SoC of the battery to increase above SoC_{h2}.

Using such a droop characteristic has two main advantages. The first one is that it includes at the primary control level a protection mechanism against the over-charge and deep-discharge of the battery. The second one is, as it will be seen in the simulation results, that the network will be able to handle multiple energy storage elements without the intervention of the higher control layer.

2.2.3 Pseudo-critical droop

Fig. 2.10 presents the characteristic for the pseudo-critical elements. Different than the previous droop characteristic, elements controlled in this manner have a critical behavior while the dc bus voltage is in the normal or safety operation bands (critical behavior meaning that they act like a constant current source and do not take the voltage amplitude into consideration when computing their power reference). The term *pseudo* was added to the description of this droop characteristic in order to describe the behavior displayed in the critical bands. If the dc voltage reaches these bands, this type of elements become non-critical and they start to regulate their output in a fashion similar to the one described in the previous section and illustrated here as equation (2.9) and (2.10). i_{dc}^{c} refers to the current reference calculated for a voltage V_{dc}^{c} situated in the critical bands. As before V_{dc}^{cl} and V_{dc}^{ch} refer to the minimum and maximum allowed values for the dc voltage, while CL and CH represent the height of the two critical bands in volts. The new current reference is calculated as a deviation from the initial current reference i_{dc}^{op} that was set in the converter before

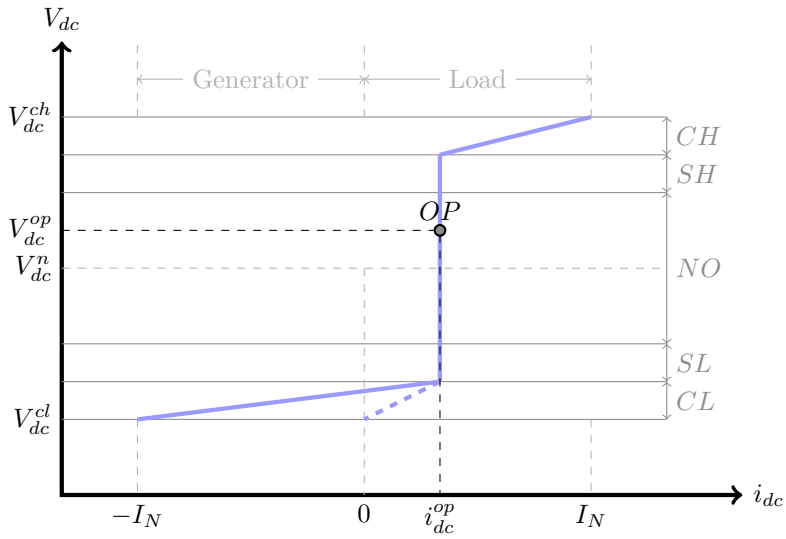

Fig. 2.10: Droop characteristic for bidirectional (solid line) and unidirectional (dotted line) pseudo-critical element.

the voltage reached the critical band.

$$i_{dc}^{c} = \begin{cases} i_{dc}^{op} - \frac{V_{dc}^{c} - V_{dc}^{cl}}{r_d} & , V_{dc}^{c} \in \left[V_{dc}^{cl}, V_{dc}^{cl} + CL\right] \\ i_{dc}^{op} + \frac{V_{dc}^{ch} - V_{dc}^{c}}{r_d} & , V_{dc}^{c} \in \left[V_{dc}^{ch} - CH, V_{dc}^{ch}\right] \end{cases} \tag{2.9}$$

$$r_d = \begin{cases} \frac{CL}{i_{dc}^{op} + I_N} & , \text{for the CL band} \\ \frac{CH}{I_N - i_{dc}^{op}} & , \text{for the CH band} \end{cases} \tag{2.10}$$

Two characteristics are displayed in Fig. 2.10. The bidirectional (solid line) allows under critical conditions for the power to flow in both directions. This type of behavior can be employed by a converter that connects to an ac grid with whom there is a power supply contract. If the dc grid operates normally, the required power is supplied as specified in the contract. However, if the voltage in the dc grid reaches critical values, the power contract is disregarded as the security of the dc network has maximum priority.

The unidirectional characteristic (dotted line) does not allow for the power to

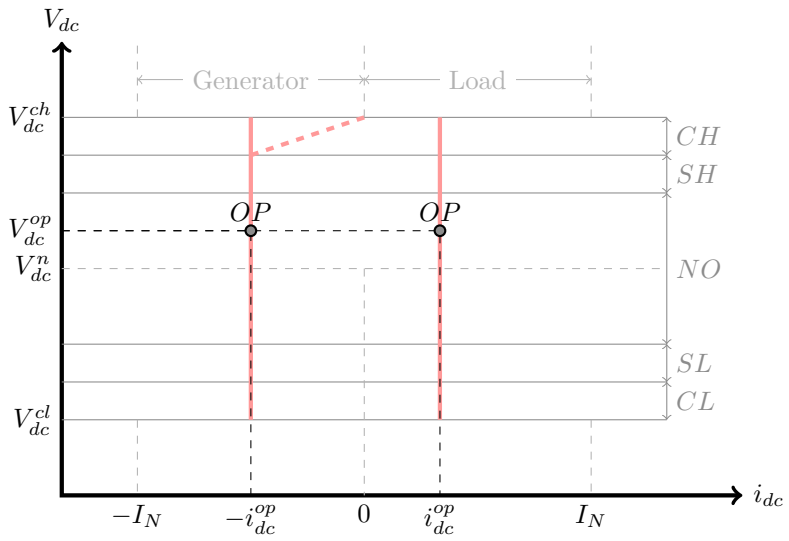

Fig. 2.11: Droop characteristic for critical load and generator

change direction and could be employed by either generators or loads that can reduce or increase their power consumption if the dc bus level reaches critical levels. In this category of elements we could include diesel generators, fuel cells, and even some maximum power point tracking (MPPT) controlled renewable sources. As for loads, smart heating or cooling units could display this exact behavior.

2.2.4 Critical droop

A critical load or a critical source will not reduce its output not even when the dc bus is in the critical bands. Since most of the generators can safely reduce their power output if needed, a small variation (dotted line) was introduced for the critical generators. Renewable sources, such as PV or wind energy, that employ some MPPT capability would typically be interfaced with the network through one of these connections. However, an element that is more likely to be encountered in the grid is the constant power load. This type of element is not able to regulate in any way its power consumption, therefore in will be seen by the grid as a critical element. Fig. 2.11 presents the droop characteristic proposed for these critical elements.

From the point of view of network security, pseudo-critical elements are prefer-

able to constant current units. This is because the pseudo-critical elements can be seen as back-up primary control units that are automatically enabled when the voltage of the network reaches the critical operating bands. However, some generators or loads are too slow in controlling their power output, or they can't control it at all; therefore these elements can only be operated as critical elements.

As it will be demonstrated in the next sections through simulation and experimental results, using these four droop characteristics for the primary control of a MTDC network is enough to maintain the system in safe operation without making use of any communication channel. Secondary control is treated in one of the next chapters of this thesis, as in order to optimize the overall behavior of the system a second layer of control that makes droop adjustments for the individual elements of the system has to be implemented.

2.3 Simulation results

In this section we are going to present a few simulation scenarios in an attempt to clarify how a network composed of elements controlled by the proposed droop characteristics will operate in a pseudo steady-state regime. These simulation scenarios were chosen considering the operation of a 100 kW PV power plant that integrates ES. At first, a very basic study case composed of three elements connected to a common dc bus will be analyzed followed by more complex ones in the latter paragraphs.

As can be inferred from the previous section, the SoC of the energy system is critical in implementing the droop surface governing the control of its converter. The estimation of the SoC, especially for batteries connected to renewable energy sources, is at the moment a troublesome aspect. The main research driver on the operation and management of batteries is the electric-vehicle industry. Various methods based on equivalent models [62–64], current integration [65, 66], artificial intelligence [67–70], or other imaginative combinations of these methods [71, 72] can be found in the literature. Applying these methods for batteries connected to renewable power plants is a rather challenging task and with questionable results.

The large differences in the cycle patterns between a battery operated in an electric vehicle and one operated, for example, in a PV system, combined with issues related to cell aging, balancing, state of health, and manufacturing inconsistencies makes the development of a robust algorithm for the SoC prediction a challenging aspect. Luckily, modern battery systems are equipped with their own battery management system (BMS) that provides information about the SoC. Such a system is based on intelligent estimation methods that have access to internal measurements of all the cells and monitors aspects related to balancing, aging, health, and SoC. As the proposed control method for ES elements depends strongly on the SoC, energy storage with a robust BMS system is needed for real-life applications.

The Coulomb counting method [66] was used to determine the state of charge of the batteries in our simulation scenarios. Starting from the initial state of charge $SoC(t_0)$, the current flowing through the battery is integrated in order to determine the remaining capacity, as described in (2.11), with Q_n representing the nominal capacity of the battery in Ah. In practice, the initial state of charge can be obtained by comparing the open circuit voltage with the characteristic provided by the battery manufacturer. This method for obtaining the SoC of the battery is a very naive approach and was chosen to be implemented in the investigated simulation and laboratory scenarios because of its simplicity and because it is sufficient in order to demonstrate the behavior of the proposed control system. Estimating the SoC in this way will not work in a real-life application because any measurement noise integrated over a long period of time will have a strong negative impact on the precision of the SoC.

$$SoC(t) = SoC(t_0) + \frac{\int_{t_0}^{t} i_{dc} dt}{Q_n} \cdot 100 \tag{2.11}$$

As the purpose of this section is to clarify the interaction between the different droops, another simplification that we introduced is to consider the cables that connect the elements of the network as being ideal, resulting in an unique voltage throughout the network. This is not the case in a real network where the various elements are interconnected by long cables, but for the sake of clarity we will allow this simplification for the moment. The impact of the connecting cables, together

with the mathematical analysis related to the sizing of the system, as well as the design of the control algorithm, are covered in details in the next chapter.

2.3.1 Study case 1 – Basic System. Energy Storage discharge.

As can be seen in Fig. 2.12, in this study-case three power converters are connected to a common dc bus. Converter 1 is a boost-converter controlled by a bidirectional droop and connects a battery with a storing capacity of 30 minutes at nominal power. A PV power plant rated at 100 kW is connected to the common dc bus by converter 3 which is controlled by a critical droop characteristic. A real irradiance profile was used in order to emulate the hectic behavior of the PV production. Finally, the system is connected through a pseudo-critical connection to the ac grid by means of a 100 kW dc-ac converter, i.e., converter 2.

Table 2.1: Parameters of the droop characteristics used in the simulation scenarios

Parameter	Value	Description
V_{dc}^{n}	685 V	*nominal voltage of the dc bus*
NO	70 V	*height of the normal operating band*
SH, SL	14 V	*height of the safety bands*
CH, CL	14 V	*height of the critical bands*
V_{dc}^{ch}	748 V	*maximum allowed voltage*
V_{dc}^{cl}	622 V	*minimum allowed voltage*
$SoC_{l1,l2}$	20%-5%	*low state of charge interval*
$SoC_{h1,h2}$	80%-95%	*high state of charge interval*

The operating intervals for the voltage and for the SoC, needed for defining the droop characteristics for the three elements, are shown in Table 2.1.

The proposed scenario starts with the battery charged at 40% of its maximum capacity and converter 2 disconnected. The average PV production is around 40 kW, but large deviations from this value typical for PV generation can be observed. Since initially converter 2 is disconnected, all the power produced by the PV goes into the batteries, increasing the SoC, visible in Fig. 2.13a.

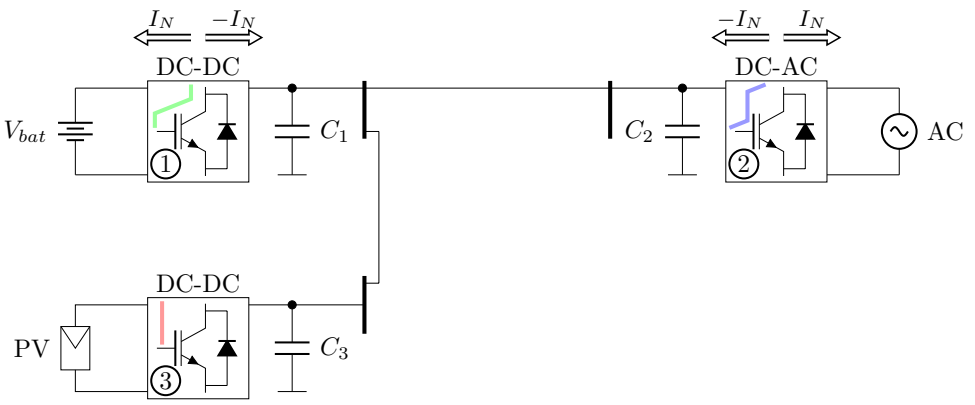

Fig. 2.12: Block diagram of simulation study case 1. Basic system composed of a bidirectional ES, one critical PV generator, and one pseudo-critical ac grid connection.

Fig. 2.13 shows the signals of interest for this scenario. A set of key events, either triggered intentionally or occurring naturally due to the operation of the system, are highlighted in Fig. 2.13 and described next. The events are marked by a vertical guideline completed with a round marker at the top of the figure.

Event 1 (Ev_1) – ac grid converter is enabled. A reference of 100 kW is set for converter 2 as can be seen in Fig. 2.13d. At this moment there are two elements controlled as constant power sources connected to the dc bus. The PV generator injects power in the dc bus, while the grid connected converter operates as a load, discharging the dc bus. Since the PV output visible in Fig. 2.13b is not sufficient to satisfy the load requirements, the dc bus capacitors will start to discharge and the dc bus voltage will decrease very fast as seen in Fig. 2.13e. The converter connected to the battery is droop-controlled, hence the voltage deviation will induce a proportional injection of power, as seen in Fig. 2.13c, in order to compensate for the imbalance between generation and load. The battery starts to discharge and the SoC decreases as shown in Fig. 2.13a. A large drop in the dc bus voltage, proportional with the power that the battery has to compensate can be noted in Fig. 2.13e, but the voltage is kept between the normal operation limits. This is due to the fact that while the SoC is out of the critical limits the battery can compensate the grid demand even if there is no power being produced by the PV.

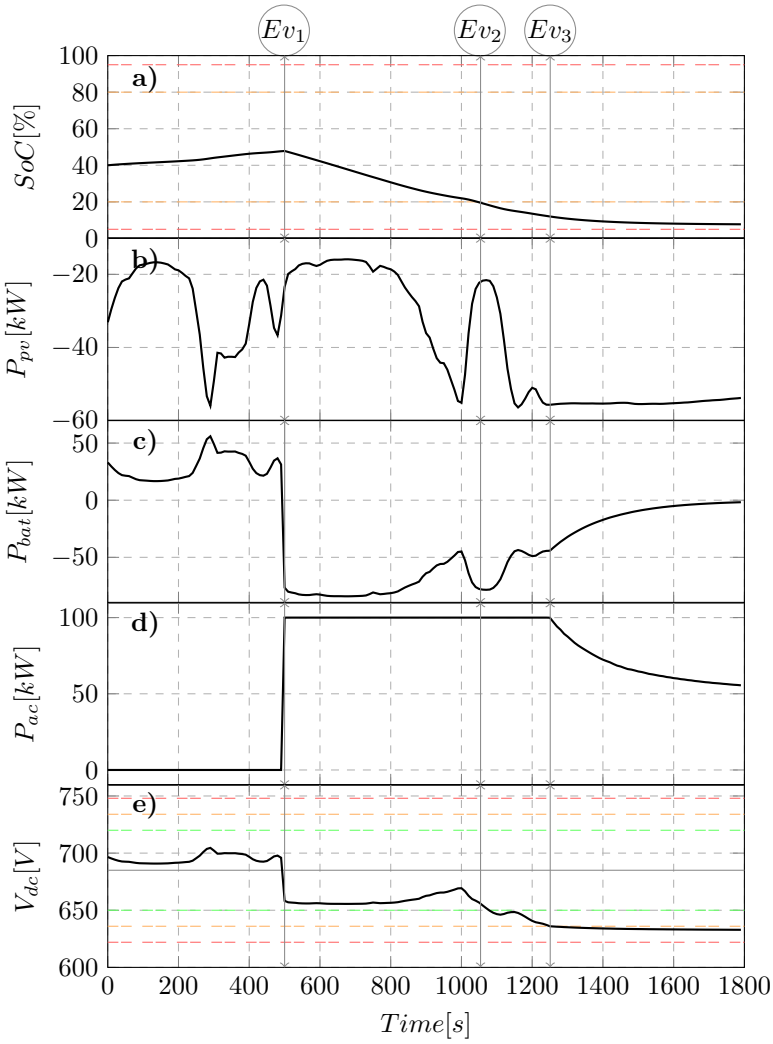

Fig. 2.13: Simulation study case 1. Basic system. Discharge of the ES a) State of charge of the ES and the operating bands (in percentage). b) Power production of the PV plant (in kW). c) Power imported/exported by the ES (in kW). d) Power injected to the ac grid (in kW). e) dc bus voltage and the operating bands (in V).

Event 2 (Ev_2) – battery SoC reaches 20%. This corresponds to SoC_{l1}. What happens next is a continuous process which is explained in Fig. 2.14. Firstly, according to the dependence of the droop characteristic on the SoC, as the battery continues discharging, the connected converter linearly shifts downwards its droop

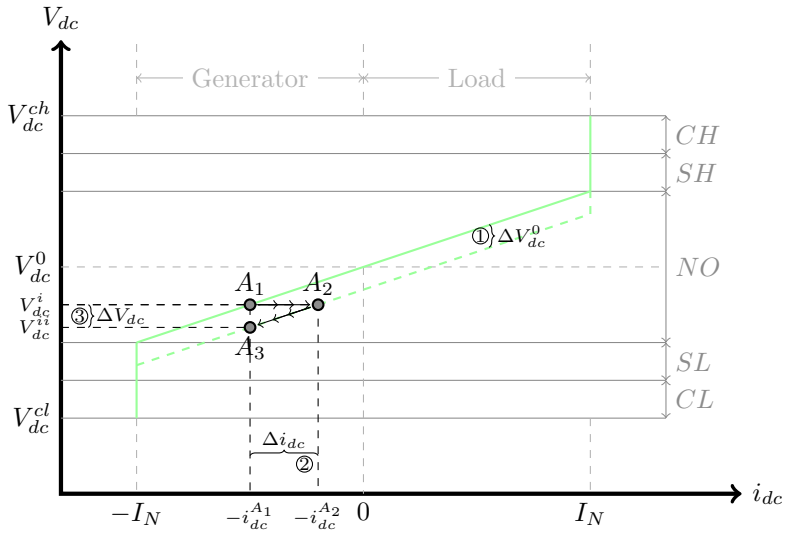

Fig. 2.14: Steady state analysis of battery droop while the SoC is decreasing.

characteristic by controlling the $\left(V_{dc}^{0}, 0\right)$ point as dictated by (2.8). The deviation ΔV_{dc}^{0} in the position of the droop moves the operating point of the converter from A_1 to A_2 causing a reduction Δi_{dc} in the injected current, and leaving the system with a slight imbalance between the load and generation. This in turn will discharge the dc bus capacitor and the dc voltage will start to decrease, finally setting the operating point of the converter to A_3– point at which the converter injects the same current as in the case of A_1, but at a lower voltage. After this, the process repeats itself. The decrease in the SoC will move the droop curve down, which in turn will generate a reduction in current, that in the end will discharge the dc capacitor and decrease the voltage, and so on.

The steps, i.e., the delta values, in Fig. 2.14 are exaggerated for the purpose of illustration. What actually happens is a continuous process, with the size of the steps at each moment being dictated by the discharge rate of the battery. This can be seen in Fig. 2.13e, where the described process linearly decreases the dc bus voltage until it reaches the critical band.

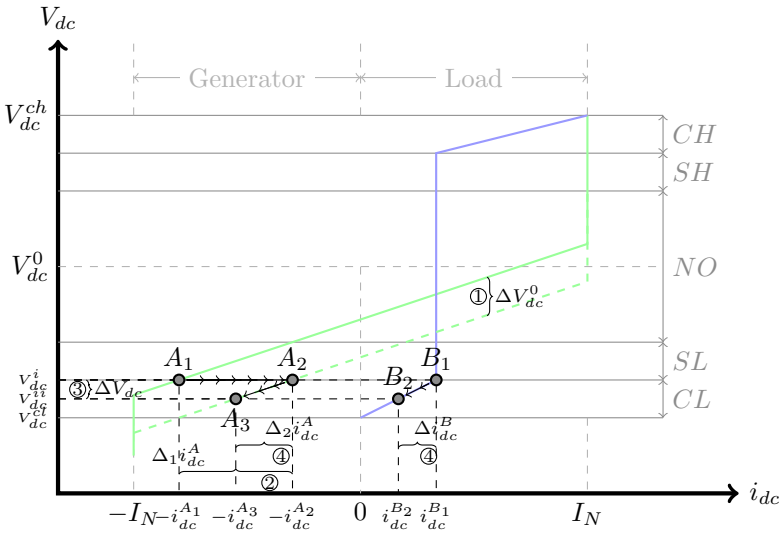

Fig. 2.15: Steady state analysis of battery droop interacting with the pseudo critical droop while V_{dc} is in the CL band.

Event 3 (Ev_3) – dc bus voltage reaches CL band. As the battery continues to discharge, the dc bus voltage reaches the critical low band as seen in Fig. 2.13e. Since the ac connection is pseudo-critical it will change from constant power control to droop control. This means that it will be able to automatically deviate from its power reference in order to maintain the power balance of the system. The interaction between the two droop curves is analyzed in Fig. 2.15. As before, the first step is done by the battery converter that shifts its droop characteristic down. This moves the operating point of the battery converter from A_1 to A_2 and causes a reduction $\Delta_1 i_{dc}^{A}$ in the injected current. As a result, the system becomes unbalanced and the dc bus capacitor discharges, as the power extracted from the dc bus is larger than the one injected. As the voltage of the system decreases, it enters the CL band where also the pseudo-critical elements contribute to the voltage regulation. As it can be seen in Fig. 2.15, since there are two elements participating in the voltage regulation the power imbalance will be shared between them. Unlike in the previous case, the new operating point for the battery converter A_3 requires a smaller current from the battery and the difference is compensated by the grid converter which shifts its operating point from B_1 to B_2.

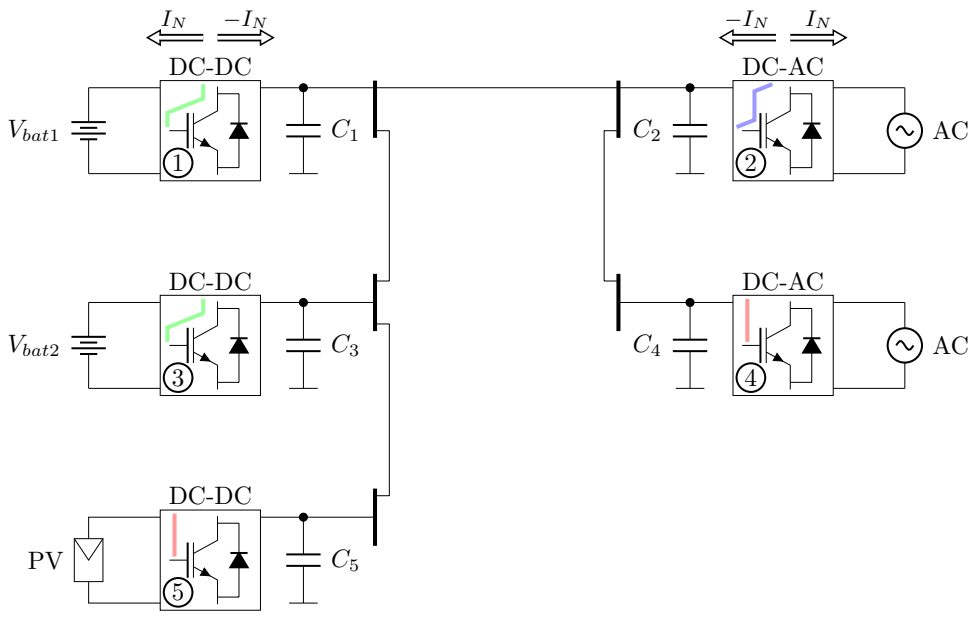

Fig. 2.16: Block diagram of study case 2. Extended system composed of two batteries, one critical PV generator, and two ac grid connections (one critical and one pseudo-critical).

This can also be seen in our simulation scenario in Fig. 2.13d. The grid power slowly deviates from its initial value in order to compensate the reduction in the battery current. Finally, the battery current is reduced to zero as the battery is getting close to SoC_{l2}. Meanwhile, the power produced by the PV is injected into the ac grid. In such a case an upper control layer or the system operator could choose to dispatch the energy in a different manner, and decide to charge the battery instead of supplying the non-critical load.

2.3.2 Study case 2 – Extended System. Energy Storage discharge.

The second scenario expands the previous one by connecting two extra converters to the common dc bus. The previous 30 minutes storage unit is split in this study case in two battery banks of 20 minutes (Bat1) and 10 minutes (Bat2), respectively. The two battery banks are interfaced by two bidirectional dc-dc converters. Additionally, the 100 kW pseudo-critical ac grid connection has been replaced by two connections,

one critical (converter 4) and one pseudo-critical (converter 2) as seen in Fig. 2.16.

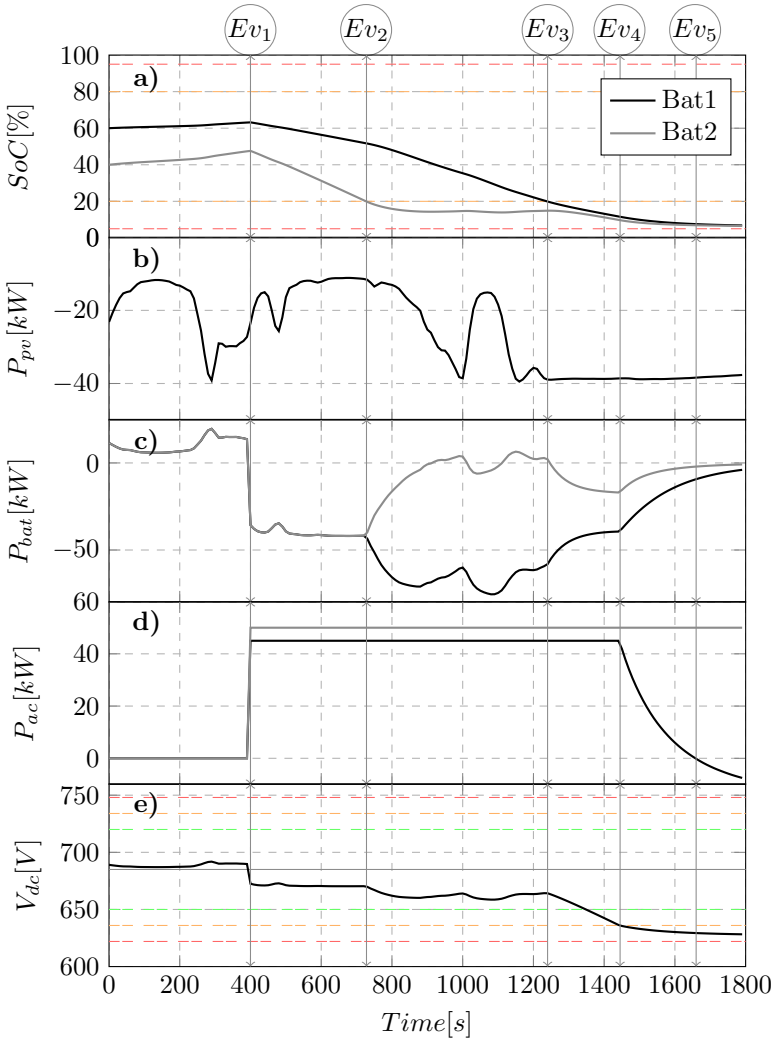

Fig. 2.17: Simulation study case 2. Extended system. Discharge of the ES. a) State of charge of the ES (in percentage). b) Power production of the PV plant (in kW). c) Power imported/exported by the ES (in kW). d) Power injected by the ac grid converters (in kW). e) dc bus voltage and the operating bands (in V).

As previously, the system starts with converter 2 and 4 disabled, and the two batteries being charged by the production of the PV. The initial state of charge of

the two batteries is 60% for Bat1 and 40% for Bat2. The evolution of the signals of interest can be observed in Fig. 2.17. As previously, the key events are highlighted at the top of the figure.

Event 1 (Ev_1) – ac grid converters are enabled. A reference of 50 kW is set for converter 4 and a reference of 45 kW for converter 2, as seen in Fig. 2.17d. Since the PV output is not sufficient to cover the power demand, the two batteries have to compensate for the difference. Both batteries have sufficient energy, therefore the load is equally shared between the two converters as can be seen in Fig. 2.17c.

Event 2 (Ev_2) – SoC of Bat2 reaches 20%. Besides having a smaller capacity, Bat2 also starts with a smaller SoC, hence it reaches the lower threshold of 20% faster, as seen in Fig. 2.17a. As a result, converter 3 will start to shift its operating voltage downwards yielding a reduction of the power output as seen in Fig. 2.17c. The steady state analysis of the interaction between the two battery droops is presented in Fig. 2.18. Initially both the batteries are operated at the same point, sharing equally the load power. Bat2 saturates first; converter 3 starts to shift its droop characteristic downwards and changes its operating point from $A_1$to A_2, causing a decrease $\Delta_1 i_{dc}^A$ in the injected current. As a result, the voltage of the dc bus starts to decrease and new operating points are reached by the two converters. Converter 1 connected to Bat1 increases the injected current by changing its operating point from C_1 to C_2, while converter 3 finally reaches A_3 where a lower current is required compared with A_1. This behavior can clearly be observed in Fig. 2.17c, while the converter connected to Bat2 reduces its power, the converter connected to Bat1 increases its reference in order to compensate for this reduction.

The dc voltage decreases only slightly because there is still one battery remaining between normal SoC limits that can fully compensate the load demand. The system continues to operate in the NO band, as it can be seen in Fig. 2.17e.

Event 3 (Ev_3) – SoC of Bat1 reaches 20%. Bat1, which until now was compensating for the reduction in the power of Bat2, also reaches SoC_{l1} and converter 1 starts to shift its operating voltage according to the implemented droop characteristic. Now both converter 1 and 3 are reducing their power and the unbalanced system discharges the dc bus capacitor. This time there is no other element in the

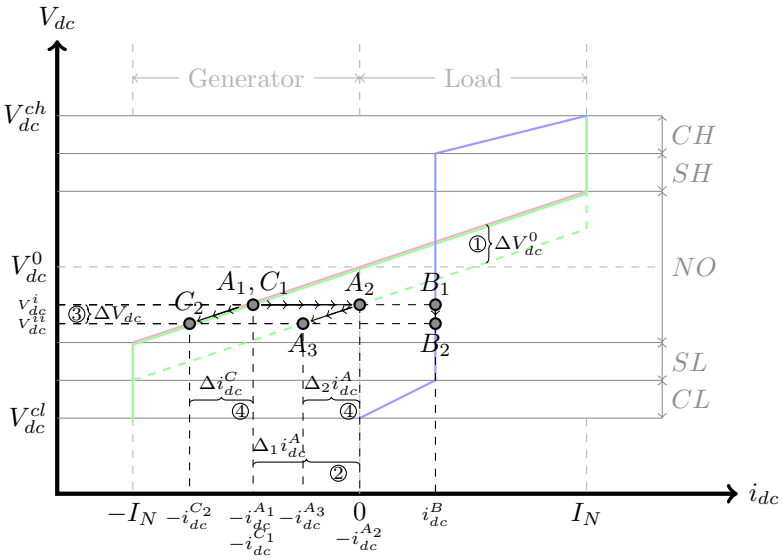

Fig. 2.18: Steady state analysis of two battery droops interacting while one of the batteries enters the low SoC band.

network to maintain the dc bus voltage in the normal operating band, hence it decreases slowly into the safety band, as seen in Fig. 2.17e.

Event 4 (Ev_4) – dc bus voltage reaches CL band. The dc bus reaches the critical low limit. At this point, the power output of the energy storage units is severely limited and the PV-production is not sufficient to supply both loads. Under these circumstances the non-critical grid connection, i.e., converter 2, starts to reduce its power output in order to avoid the collapse of the system. As it can be seen in Fig. 2.17d, the reference of 50 kW for converter 4 is still entirely fulfilled, while the reference for converter 2 starts to deviate from its scheduled value.

Event 5 (Ev_5) – inversion of power direction. If the droop characteristic allows it, the non-critical grid connection can pass from consuming power to injecting power in order to supply the requirement of the critical load, as seen in Fig. 2.17d the sign of the power changes at Ev_5.

An interesting aspect that needs to be pointed out is the ability of the system to properly manage itself even with multiple energy storage elements. The overall behavior of the system is somehow natural and intuitive: the ES element with the

highest charge will inject the most power in order to regulate the voltage, similarly the ES elements with the lowest SoC will absorb the most power. The system will always try to balance the energy between the various storage elements. This aspect can be observed by analyzing the SoC of the two ES between Ev_2 and Ev_4 in Fig. 2.17a. After Bat2 reaches the low SoC band its discharge is almost completely stopped; the battery is *waiting* for all the other ES elements to reach the low SoC band. When this happens at Ev_3 the discharge starts once again in a final attempt to stabilize the dc bus voltage. This behavior can also be observed in the following study-case where a more complex scenario is investigated in order to test the ability of the system to manage itself without the action of a centralized control layer.

2.3.3 Study case 3 – Extended System. Energy Storage charge. Trip of a converter.

The same 5-element network used in the previous scenario was used here as well. The initial SoC of the batteries is 70% for Bat1 and 60% for Bat2. As before, the two grid converters are initially disabled and all the power produced by the PV charges the two batteries. The average power produced by the PV is around 60 kW, and the batteries, already at a high SoC, are charging fast.

Event 1 (Ev_1) – Bat2 reaches 80%. This corresponds to SoC_{h1} and, according to the definition of the droop surface, the converter starts to shift upwards its droop characteristic reducing the charging current, as seen in Fig. 2.19c. This leaves the system slightly unbalanced, with more power being injected than extracted from the dc bus. This small difference in power charges the dc bus capacitor and increases the voltage of the network. This increase in voltage will define a new operating point for Bat1, of higher charging current.

Event 2 (Ev_2) – ac grid converters are enabled. The two grid converters are enabled and a reference of 22 kW is set for the pseudo-critical connection, i.e., converter 2, and 20 kW for converter 4, which is controlled as a critical element. The self-balancing property of the system that was mentioned earlier can also be noted here. At the moment when the two grid converters are connected, Bat2 starts discharging (P_{bat} becomes negative), while Bat1 continues to charge for a while.

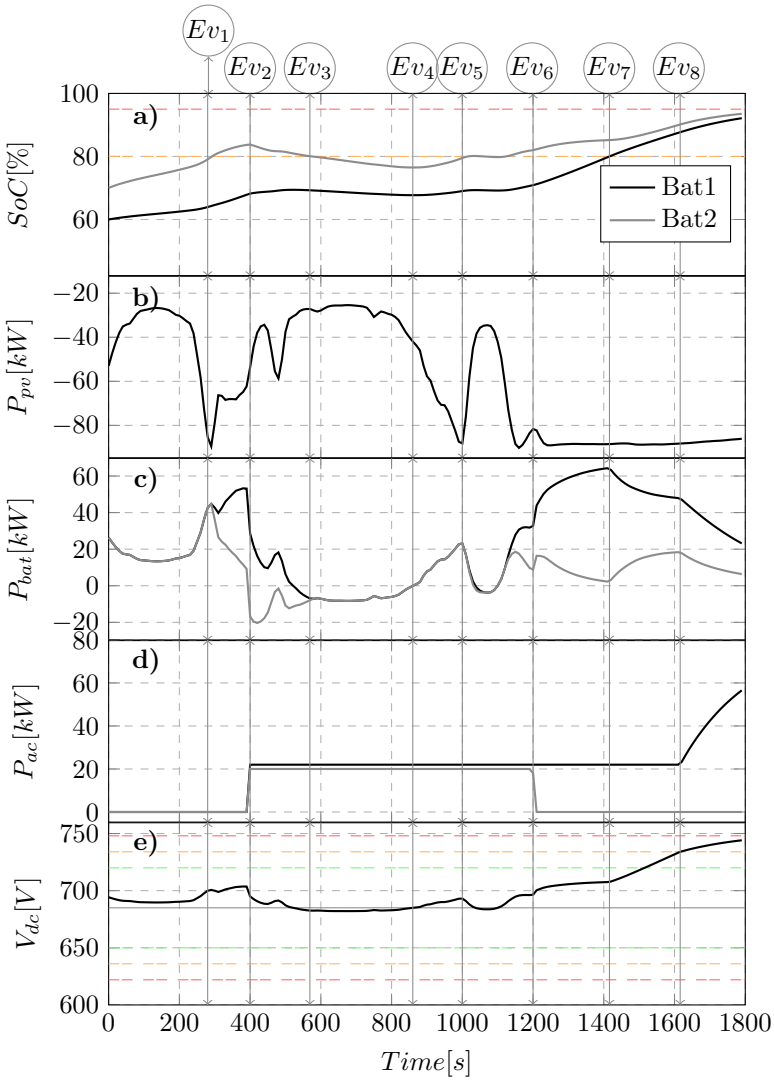

Fig. 2.19: Simulation study case 3. Extended system. Charge of the ES. a) State of charge of the ES (in percentage). b) Power production of the PV plant (in kW). c) Power imported/exported by the ES (in kW). d) Power injected by the ac grid converters (in kW). e) dc bus voltage and the operating bands (in V).

Event 3 (Ev_3) – Bat2 enters the normal SoC band. As the discharge of Bat2 continues, its SoC decreases below SoC_{h1} and the power difference between the PV production and the ac loads is shared equally between the two batteries, as can be

seen in Fig. 2.19c. The large reduction in the PV power visible in Fig. 2.19c forces the two batteries to discharge in order to satisfy the load demand.

Event 4 (Ev_4) – dc voltage equal to V_{dc}^n. By controlling the ES elements with the proposed strategy, the dc bus voltage becomes an indicator of the state of the system. As can be seen in Fig. 2.19e when the production is larger than the consumption and the batteries are charging, V_{dc} is above the nominal value V_{dc}^n. Similarly, when the system is overloaded and the batteries are discharging V_{dc} is below the nominal. As seen at Ev_4 when the balance between production and consumption is satisfied V_{dc} is equal to V_{dc}^n.

Event 5 (Ev_5) – Bat2 reaches again 80%. As the PV production increases again, the two batteries start to charge, and Bat2 enters once again the high SoC band as can be seen in Fig. 2.19a.

Event 6 (Ev_6) – Converter 4 trips. The critical connection to the grid trips at Ev_6 and the imbalance in the system becomes more obvious. Bat1 still operates in the normal SoC band therefore it compensates the reduction in the load by increasing the charging power. Bat2 is already in the high SoC band and it continues to reduce its charging power, as seen Fig. 2.19c. The system is overcharged and this can also be seen in the increasing V_{dc}.

Event 7 (Ev_7) – Bat1 reaches 80%. The charging continues, as the PV production remains above the grid demand. Finally Bat1 reaches the high SoC band and converter 1 starts to shift its droop characteristic upwards. Once again the self-balancing property of the system can be observed. As Bat1 starts to reduce its power, Bat2 tries to compensate – even though it is already in the high SoC band – in a final attempt to avoid the increase in the voltage level. The two batteries are driven together towards the maximum SoC level.

Event 8 (Ev_8) – dc bus voltage reaches CH band. The charging power of the two batteries is not sufficient to balance the system and so, the dc bus capacitors are starting to charge and the dc bus voltage increases. As the dc bus voltage enters the CH band, the pseudo critical element changes from constant power control to droop control and participate in the voltage regulation. As can be seen in Fig. 2.19d, converter 2 increases its power in order to match the large PV-production. Meanwhile,

the two batteries continue to decrease their charging power as their SoC approaches the maximum level.

In this section we tried to provide a clear picture on how the different droop controllers interact between them and how the system behaves under various scenarios. Further on, we will present some experimental results obtained from our 10 kW laboratory prototype. The same behavior observed in simulations was reproduced by the experimental results, thus confirming the potential of the proposed solution to operate independently as a primary control layer for a MTDC network.

2.4 Experimental results

In order to validate the simulation results, a scaled prototype was assembled in our laboratory, as shown in Fig. 2.20. Three elements were connected to a common 685 V dc bus. The energy storage element, a 24 Ah lead acid battery, was connected through a three-phase interleaved boost dc-dc converter that was controlled by a dSpace 1103 unit. The 10 kW ac grid connection was performed through a 2 level dc-ac converter, controlled by another dSpace 1103 unit. Finally, the PV was emulated by programming a real irradiance profile in a current controlled Regatron power source. The detailed description of the elements connected to the experimental setup is presented in Table 2.2. More information about the experimental setup can be found in Appendix A.

In this experiment the height of the NO band for the droop controller was fixed to 16 V. The critical bands and the safety bands were chosen equal to half of the normal operation one.

While performing tests for determining the behavior of the batteries, we observed increased power sensitivity at low or high SoC. However, this is a well-known effect in lead-acid batteries according to [73]. Therefore, the limits of 5% and 95% used in simulation were impracticable due to the small amount of power that the battery is able to provide, respectively absorb at these levels. The following limits were chosen for the practical usage of the lead-acid battery: $SoC_{l2} = 30\%$, $SoC_{l1} = 45\%$, $SoC_{h1} = 60\%$, $SoC_{h2} = 75\%$. All the parameters used for design-

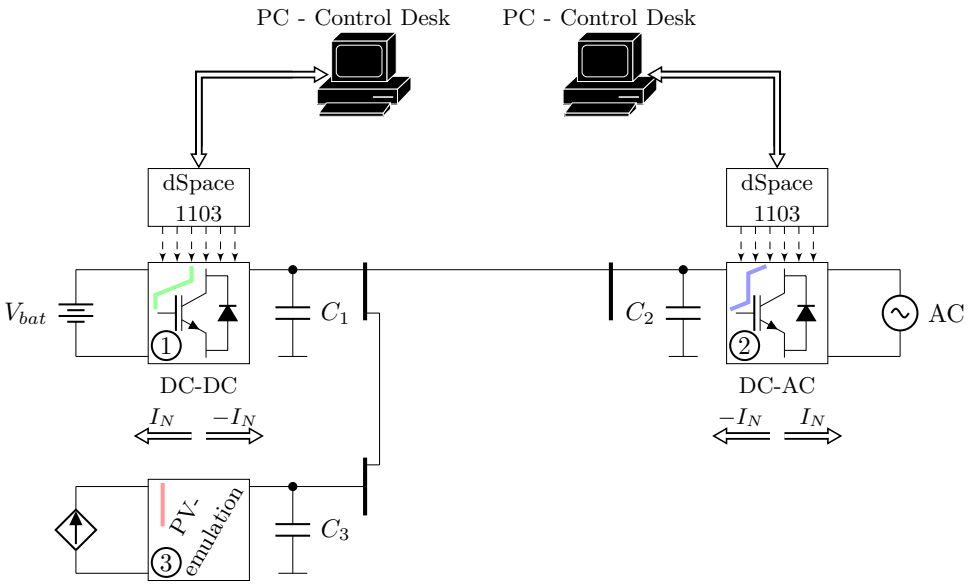

Fig. 2.20: Block diagram of experimental setup. Basic system composed of a bidirectional ES, one critical PV generator, and one pseudo-critical ac grid connection.

Table 2.2: Parameters of the Experimental Setup

		Description	Value
dc-dc	P_n	nominal power	10 [kW]
	V_{dc}	dc bus voltage	685 [V]
	V_{bat}	battery voltage	200 [V]
	f_s	switching frequency	10 [kHz]
dc-ac	P_n	nominal power	10 [kW]
	V_{dc}	dc bus voltage	685 [V]
	f_s	switching frequency	10 [kHz]
Battery	Sprinter - P12V600 Lead Acid		
	V_n	nominal unit voltage	12 [V]
	C_n	nominal capacity	24 [Ah]
	The battery bank contains 17 units connected in series		
PV	P_n	nominal power	10 [kW]
	emulated using real irradiation data for a Regatron power source		

Table 2.3: Parameters of the droop characteristics used in the simulation scenarios

Parameter	Value	Description
V_{dc}^{0}	685 V	*nominal voltage of the dc bus*
NO	16 V	*height of the normal operating band*
SH, SL	8 V	*height of the safety bands*
CH, CL	8 V	*height of the critical bands*
V_{dc}^{ch}	709 V	*maximum allowed voltage*
V_{dc}^{cl}	661 V	*minimum allowed voltage*
$SoC_{l1,l2}$	45%-30%	*low state of charge interval*
$SoC_{h1,h2}$	60%-75%	*high state of charge interval*

ing the droop characteristics for the experimental study cases are summarized in Table 2.3.

2.4.1 Study case 1 – Energy Storage discharge

The first study case investigates the self-management capability of the system when the battery is discharging. The experiment starts with the battery charged at 56% and the grid converter disconnected. Therefore, all the power produced by the PV goes into the batteries, increasing the SoC, visible in Fig. 2.21a. In the same fashion as before, Fig. 2.21 shows the signals of interest for the described scenario and highlights the key events that are detailed in the following paragraphs.

Event 1 (Ev_1) – ac grid converter is enabled. The ac grid converter is enabled and a reference of 8 kW is set, as seen in Fig. 2.21d. Since the PV output, Fig. 2.21b, is not sufficient to satisfy this demand, the system remains unbalanced and the dc bus voltage decreases fast as the capacitors discharge. This decrease in voltage generates a new operating point on the droop characteristic of the battery, increasing the injected power in order to compensate for the difference. The battery starts discharging as seen in Fig. 2.21a and Fig. 2.21c. A large drop in the dc bus voltage, proportional with the power that the battery has to compensate, can be noted in Fig. 2.21e. However, the voltage remains between the normal operation limits as long as the battery is out of the critical SoC limits.

Event 2 (Ev_2) – PV power fluctuation. Fluctuations in the PV production, seen

in Fig. 2.21b, are compensated entirely by the battery; the grid converter is operated at constant power while the system is in the normal operation band.

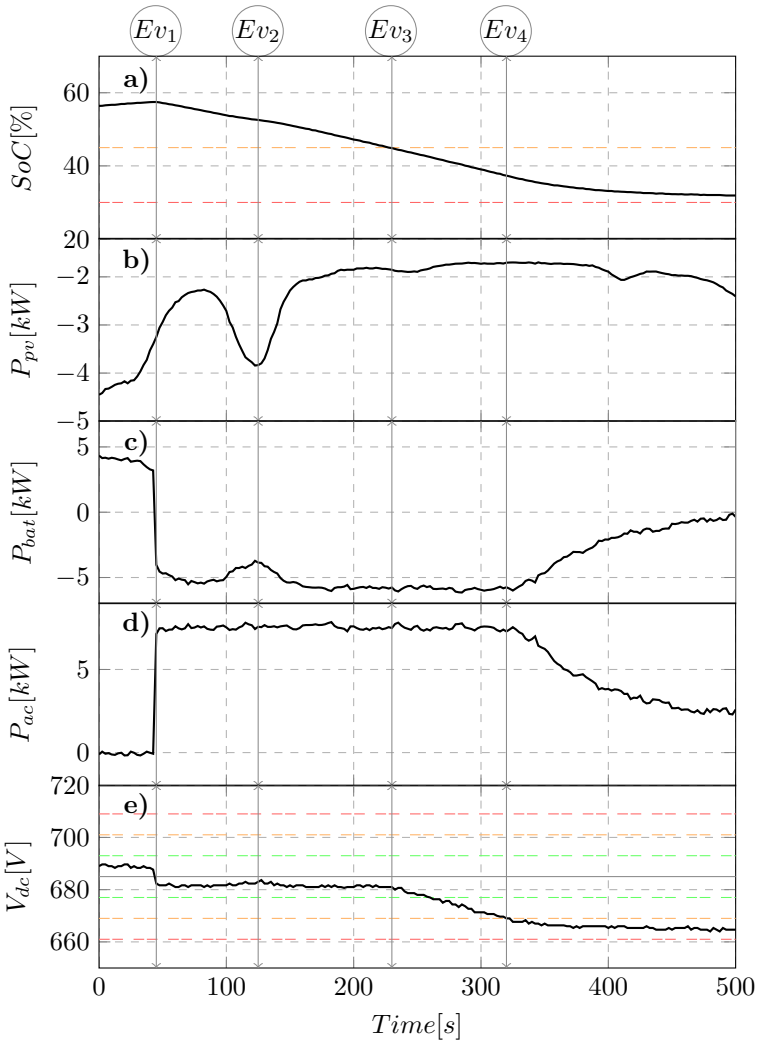

Fig. 2.21: Experimental study case 1. Basic system. Discharge of the ES. a) State of charge of the ES (in percentage). b) Power production of the PV plant (in kW). c) Power imported/exported by the ES (in kW). d) Power injected by the ac grid converter (in kW). e) dc bus voltage and the operating bands (in V).

Event 3 (Ev_3) – battery SoC reaches 45%. The SoC of the battery reaches

SoC_{l1} and, since the discharge continues, the converter linearly shifts its droop characteristic down and limits the discharge current. This leaves the system slightly unbalanced and the dc bus capacitors start to discharge. As the voltage decreases, a new operating point is established on the droop curve, as explained in the previous section in Fig. 2.14. The dc bus voltage linearly decreases towards the CL band signaling the reduced energy level remaining in the battery.

Event 4 (Ev_4)– dc bus voltage reaches CL band. The dc bus voltage reaches the CL band, as seen in Fig. 2.21e. At this point, the pseudo-critical grid connection changes from constant power control to droop control and starts to reduce its power demand as shown in Fig. 2.21d in order to avoid the collapse of the dc voltage.

2.4.2 Study case 2 – Energy Storage charge

The second scenario, presented in Fig. 2.22, investigates the behavior of the system when the battery is charging. As before, the initial SoC of the battery is 57% and the ac grid converter is disabled, the power produced by the PV charging the battery. The events highlighted in Fig. 2.22 are detailed in the following paragraphs.

Event 1 (Ev_1) – ac grid converter is enabled. The ac grid converter is enabled and a reference of -2.8 kW is set, as shown in Fig. 2.22c. Since both the grid converter and the PV are injecting power into the dc bus, the rate of charge of the battery increases in order to maintain the system in equilibrium, as seen in Fig. 2.22a and Fig. 2.22c. A change in the dc bus voltage level, proportional with the increase in the injected power, is seen in Fig. 2.22e at the moment of connection, but the final value is inside the NO band.

Event 2 (Ev_2) – battery SoC reaches 60%. The SoC of the battery, shown in Fig. 2.22a, reaches the 60% limit, which corresponds to the the experimental SoC_{h1}. Since the charge continues, the converter linearly shifts upward its droop characteristic, limiting the charge current. Similar to the previous study case, this generates a linear increase in the voltage, bringing the dc bus voltage towards the critical high band, as seen in Fig. 2.22e.

Event 3 (Ev_3) – dc bus voltage reaches CH band. The dc bus voltage reaches the critical high band. Since the grid converter is controlled as a pseudo-critical

element it will automatically shift to droop control and it will start to decrease the power injected into the dc bus, as seen in Fig. 2.22d.

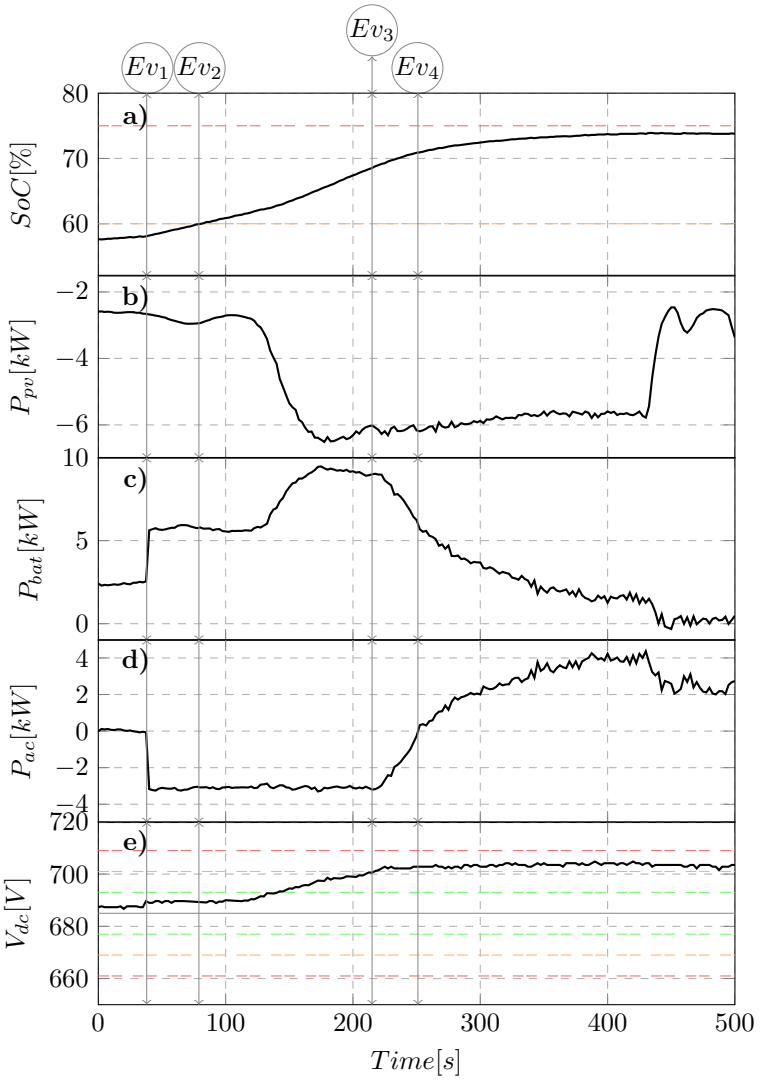

Fig. 2.22: Experimental study case 2. Basic system. Charge of the ES. a) State of charge of the ES (in percentage). b) Power production of the PV plant (in kW). c) Power imported/exported by the ES (in kW). d) Power injected by the ac grid converter (in kW). e) dc bus voltage and the operating bands (in V).

Event 4 (Ev_4) – inversion of power direction. Since the droop of the grid converter is bidirectional, it allows for the converter to change the sign of its reference. As shown in Fig. 2.22d, the grid converter independently modifies its power reference from charging the dc bus to loading it, in order to avoid an overvoltage situation. In this way the battery can reduce its charging power to zero.

2.5 Conclusions

While supporting the idea of a hierarchical control strategy for MTDC networks, we have presented in this chapter a new methodology for planning the primary control. We propose five operating voltage intervals for characterizing the different states of the network, i.e., normal, alert, and critical. Then, based on these voltage intervals we designed different droop characteristics for the various elements that might be encountered in a dc power system. Given the previous discussions about the importance of the ES elements in the future of the power system, particular attention was paid to the control of the ES elements. For this we defined a droop surface that depends on the SoC as well as on V_{dc}.

The simulation and experimental results have shown that controlling the network in this way introduces more independence and flexibility at the primary control level. The system can operate without a central controller and, if properly designed, it can handle situations such as energy storage saturation or converter trips. Moreover, given the droop characteristic proposed for the ES elements, the system is able to beautifully manage in a decentralized fashion the balance of energy between the various ES elements.

The simulation and experimental scenarios considered the cables of the network as being very short so that they can be ignored when analyzing the behavior of the system. This resulted in a unique value for V_{dc} for all the power system, similar to the frequency in ac grids. This however is not the case in a real system and, as it will be shown in the next chapter, the resistance of the cables will generate steady state voltage deviations between the various busses, depending on the power flow that the lines have to accommodate. Moreover, the reactance of the lines will generate

transient voltages and need to be taken into account when sizing the system.

Another aspect that requires additional words of caution is the design of the ES droop surface. In the proposed strategy a linear relationship between the SoC and the limitation in current is assumed for the SoC-high and SoC-low intervals. However, this assumption is not valid for any type of ES, as some of them have very non-linear power dynamics. For example, in the lead-acid batteries used in the experimental setup, the amount of energy that they were able to provide at a given SoC was influenced by the rate at which this energy was being used. In other words, considering the following two scenarios: 1) the battery is charged at SoC_0 and discharged at a rate equal to the the nominal current I_N, and 2) the battery also starts at SoC_0, but it is discharged at a rate equal to half the nominal current. Given these two scenarios, the battery will provide more energy in the second case than in the first. What we are trying to underline here is that, at least in lead-acid batteries, the SoC is not a direct indicator of the usable energy in the battery. Therefore, in order to design a control strategy that properly manages the energy reserves of the battery, all these nonlinearities have to be taken into account.

Chapter 3

Design Considerations for Primary Control

While the previous chapter offered a detailed picture of how the proposed primary control should behave and it focused on providing a clear idea regarding the interaction between the different droop characteristics, this chapter addresses problems related to the design of the system. The relationship between the size of the voltage operating bands and the parameters of the primary control is discussed in details. Analytical formulas are developed for estimating the voltage peaks during transients and then, it is shown how these values can be used to dimension the primary control of each VSC connected to the network. Further on, an improved droop control strategy, that attenuates the voltage oscillations during transients, is proposed. The proposed methods are validated on a meshed dc-grid proposed in [61]. Starting from the structure of the network and the power rating of the converters at each terminal, the output capacitors and the primary control layer are designed together in order to ensure acceptable voltage transients.

3.1 Introduction

Fig. 3.1 shows a typical cascaded structure used for the control of the voltage at the output of a power converter. The internal loop controls the injected current by properly changing the duty cycles of the PWM unit. The current controller $K_i(s)$ is a negative feedback controller and would typically be implemented so that it achieves zero steady state error; this implies that the converter will perfectly track its current reference. The outer loop controls the dc-voltage by properly adjusting the reference

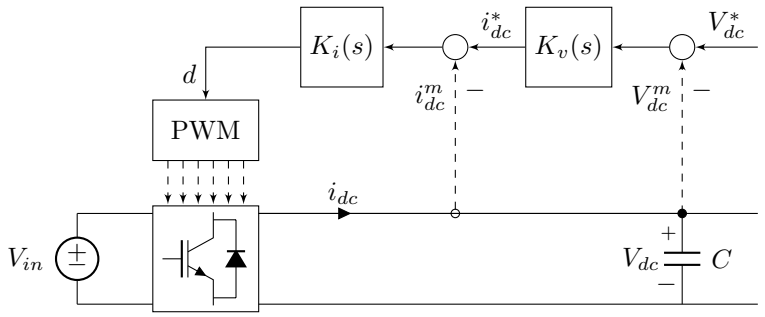

Fig. 3.1: DC-voltage control diagram.

for the current loop.

The advantage of this method is that it can limit the injected current in case of short circuits and it is preferred to the single voltage loop when used in power systems applications. Also, if a droop controller is required for the control of the voltage, any voltage deviation would require a precise current injection; therefore, a current controller that is able to perfectly track its reference is required for droop control. The downside of this control structure is that it requires two sensors, one for the voltage and one for the current, and it is slower than the single loop approach.

The input voltage source V_{in} can be an ac source corresponding to an ac-grid or a single ac-generator, such as a wind-turbine, but it can also be a dc source, such as a battery or a PV generator. Depending on the type of the input voltage source, the topology of the power converter and also the specific implementation of the two controllers will be different, but the overall control structure would be the same.

The same control method is also widely used in the control of power converters connected to ac power system because of the same reason, i.e., it can limit the current injection in case of short-circuits on the grid side.

3.2 DC voltage droop control dynamics

The previous chapter analyzed the behavior of the droop control from a steady-state perspective. Now, in order to get a better understanding on the parameters that interact at the primary control layer, we are going to take a look at the dynamic

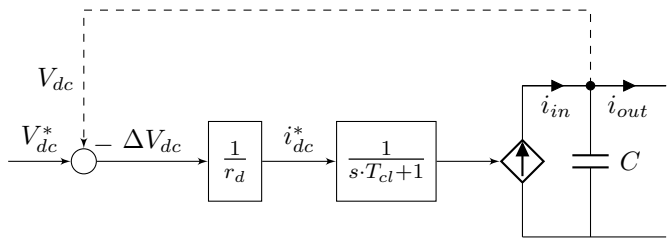

Fig. 3.2: Block diagram of DC-bus voltage controlled by droop.

behavior of the droop-controlled dc-voltage. As it was argued in the previous section and can also be seen in Appendix A, we chose to control the dc-bus voltage by regulating the current injected into the dc-bus capacitor. In order to achieve this, a zero steady-state error current control loop is required, this being easily obtained using classic control methods as shown in [74]. Taking this into consideration, we simplified the control structure used in our analysis to the one shown in Fig. 3.2. Here, we consider that the closed loop dynamics of the current loop are perfect and the only parameter of interest is its speed. Therefore, we approximated the closed loop current dynamics with a first order element with time constant T_{cl}. The voltage loop is implemented as a droop controller and the parameter of interest is the equivalent droop resistance r_d.

Intuitively, the system of Fig. 3.2 would operate as follows: at steady state, the current i_{in} injected into the system by the converter is equal to the load current i_{out}. If i_{out} is suddenly increased, in the first instants, the capacitor will start to discharge as i_{in} is maintained constant. The decrease in the dc voltage will activate the voltage droop that in turn will increase the current reference i_{dc}^*. However, i_{in} will not change instantaneously, but with the dynamics of the current loop. The initial design problem then becomes: given a certain speed for the current loop of the converter, the droop resistance and the output capacitor have to be sized so that the voltage does not go out of the operation limits during transients.

Fig. 3.3 shows the typical evolution of the current injected by the converter and of the dc voltage after a step change in the load current i_{out}. Both the current and the voltage responses exhibit a peak overshoot and damped oscillations typical for

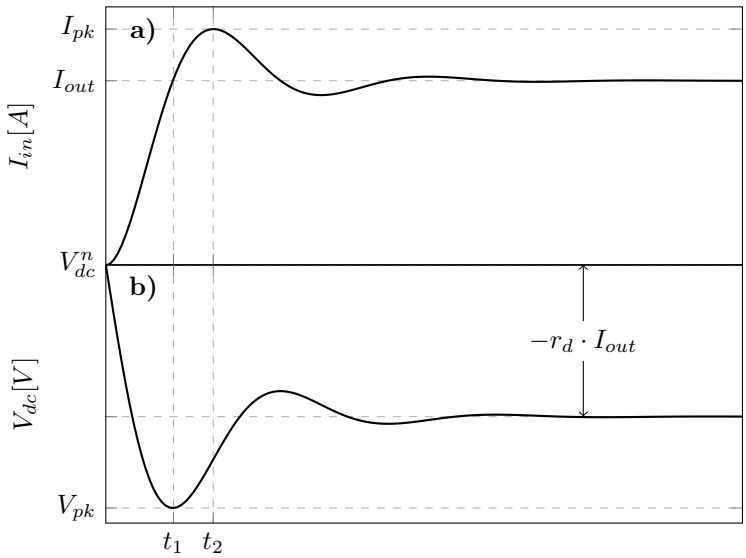

Fig. 3.3: Evolution of the a) current injected by the VSC and b) dc voltage to a step in the load current.

second order systems. This behavior can be properly characterized by analyzing the transfer functions emerging from the system shown in Fig. 3.2.

As it can be seen in Fig. 3.2, there are two inputs to the system that can generate changes in the output current and voltage. The first one is the voltage reference V_{dc}^{*} and the second one is the load current i_{out}. Equation (3.1) shows the relationship between V_{dc}^{*}, the load/disturbance current i_{out}, and the injected current i_{in}, with the corresponding transfer functions being defined in (3.2) and (3.3).

$$i_{in} = V_{dc}^{*} \cdot H_{*u} + i_{out} \cdot H_{du} \tag{3.1}$$

$$H_{*u} = \frac{C \cdot s}{C \cdot T_{cl} \cdot r_d \cdot s^2 + C \cdot r_d \cdot s + 1} \tag{3.2}$$

$$H_{du} = \frac{1}{C \cdot T_{cl} \cdot r_d \cdot s^2 + C \cdot r_d \cdot s + 1} \tag{3.3}$$

For our analysis, the effect of the changes in V_{dc}^{*} on the injected current is not so critical. This is due to the fact that, as it will be seen in the next chapter, V_{dc}^{*} is reg-

ulated by the secondary control layer and, in order to avoid fast changes, additional pre-filters can be mounted on the input path. Variations in the load current, on the other hand, are unpredictable and they can occur in steps; it is their impact on the injected current and output voltage that we are interested in.

As seen in (3.3), the transfer function from the disturbance current to the actual injected current is of second order and can be written in the canonical form with the terms presented in (3.4).

$$\begin{aligned} \xi &= \sqrt{\frac{r_d \cdot C}{4T_{cl}}} \\ \omega_n &= \sqrt{\frac{1}{r_d \cdot C \cdot T_{cl}}} \end{aligned} \tag{3.4}$$

There are a few important aspects that can be observed from these expressions. If the time response of the current loop is fast, i.e., T_{cl} very small, then the response of the system is approximately the one of a first order system with a time constant equal to $r_d \cdot C$. From (3.4), it can be observed that if $r_d \cdot C > 4T_{cl}$, the system will experience an overdamped response, therefore there will be no overshoot in the current response; otherwise, the damping of the system can be improved either by making the current loop faster, therefore decreasing T_{cl}, either by increasing r_d or C.

As seen in Fig. 3.3a, the current response will experience a peak value I_{pk}. Using the procedure presented in Appendix B, for a unit step in i_{out}, the peak current injected by the converter is obtained as shown in (3.5). For safety reasons, this value has to be smaller than the peak rating of the converter.

$$I_{pk} = 1 + e^{-\pi \cdot \sqrt{\frac{r_d \cdot C}{4T_{cl} - r_d \cdot C}}} \tag{3.5}$$

Further on, by taking the transfer functions of the systems interacting in Fig. 3.2 we can determine the expression of the output voltage, as shown in (3.6). We can see from (3.8) that the effect of the disturbance on the dc voltage is of a second order system with an additional zero. As previously, a fast current loop would transform

the system into a first order system with the time constant imposed by r_d and C.

$$\begin{aligned} V_{dc} &= V_{dc}^{*} \cdot H_{*y}(s) + i_{out} \cdot H_{dy}(s) && (3.6)\\ H_{*y}(s) &= \frac{1}{C \cdot T_{cl} \cdot r_d \cdot s^2 + C \cdot r_d \cdot s + 1} && (3.7)\\ H_{dy}(s) &= -\frac{r_d \cdot (T_{cl} \cdot s + 1)}{C \cdot T_{cl} \cdot r_d \cdot s^2 + C \cdot r_d \cdot s + 1} && (3.8) \end{aligned}$$

According to (3.8), the steady state gain of the system is equal to r_d, that is, the steady state voltage offset is equal to the product between the droop resistance and the load current, as highlighted in Fig. 3.3b. Meanwhile, the peak value of the voltage during transients V_{pk} can be calculated in a similar fashion to I_{pk} by making use of the formulas presented in the Appendix B, as shown in (3.9). The terms of (3.9) are defined in (3.10) based on the natural frequency ω_n and damping ξ introduced earlier in (3.4).

$$V_{pk} = -r_d \cdot \left(1 - e^{-\xi \omega_n t_{pk}} \cdot \left(\cos(\omega_d \cdot t_{pk}) + \beta \cdot \sin(\omega_d \cdot t_{pk})\right)\right) \tag{3.9}$$

$$\begin{aligned} t_{pk} &= \frac{1}{\omega_d} \cdot \left[\tan^{-1}\left(-\frac{T_{cl} \cdot \omega_n^2}{\omega_d + \xi \cdot \omega_n \cdot \beta}\right) + \pi\right]\\ \omega_d &= \omega_n \cdot \sqrt{1-\xi^2}\\ \beta &= \frac{\xi}{\sqrt{1-\xi^2}} - T_{cl} \cdot \omega_d - \frac{\xi^2}{\sqrt{1-\xi^2}} \cdot T_{cl} \cdot \omega_n \end{aligned} \tag{3.10}$$

As seen in Fig. 3.3b, in the case of a sudden increase of load, V_{pk} will be considerably smaller than the nominal dc voltage. Considering the definition of the voltage operating bands from the previous chapter, V_{pk} should remain inside the safety operating bands during transients.

Sudden increases of load are atypical events in the power system, as the load power is usually slowly ramped up. However, a rather possible occurrence is the sudden decrease of load as a result of a trip. In this case, the voltage peak V_{pk}

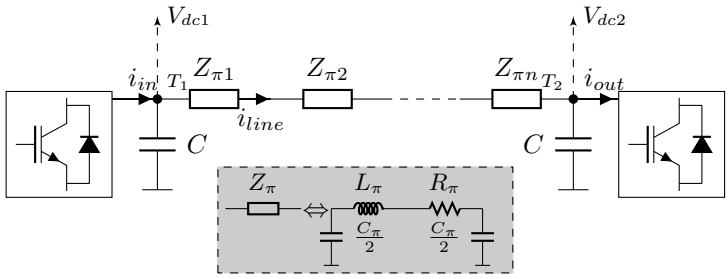

Fig. 3.4: Block diagram of two converters connected through a long cable or overhead line.

will be larger than the nominal value and, if the system is not properly sized, it can damage the power converter.

3.3 Effect of connecting cable on droop control dynamics

In the previous section we have shown how a change in the load current will create overshoots, both in the current injected by the converter and in the voltage across the output capacitor. However, the step change in the load current was considered near to the output capacitor which is typically not the case in a real system.

A more common scenario would be the one shown in Fig. 3.4: one converter acting as load is connected to the generating-converter through a long cable or overhead line. In the presented system, the converter at terminal 2 (T2) acts as load draining the dc-bus with the current i_{out}, meanwhile, the converter at terminal 1 (T1) regulates the voltage through a droop control loop as in the previous section.

Before advancing, a few things regarding the cable model should be pointed out. In ac systems the π-model is considered suitable for cable lengths up to 50 km and overhead lines up to 170 km [48]. Therefore, for modeling longer lines, multiple π-sections have to be chained together as shown in Fig. 3.4. According to [75] the cascaded π-section model performs rather well only up to the frequency range of 3-4kHz. However, this is more than enough for dc systems, where the large capacitor at the output of the VSC will dominate the high frequency dynamics of the equivalent impedance seen from the terminals of the VSC. Moreover, for large enough dc-bus capacitors, modeling the line by using one single π-section will give

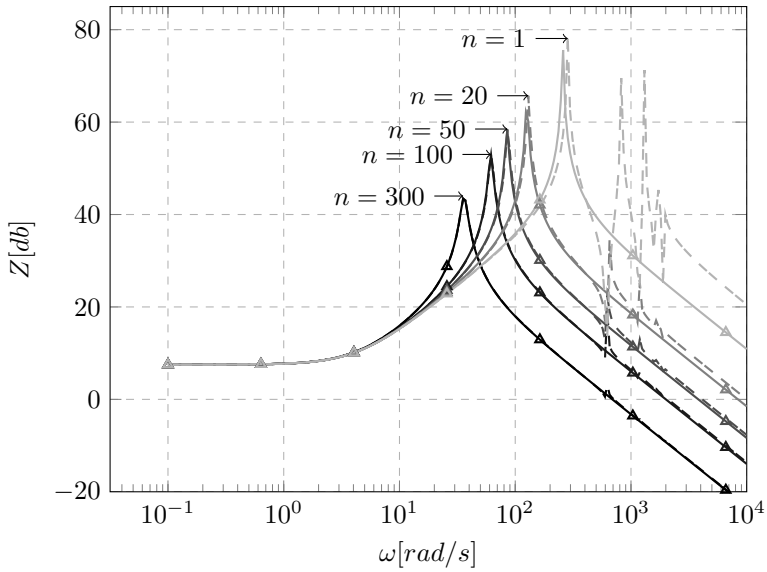

Fig. 3.5: Equivalent impedance seen by the VSC when connected to a 250 km cable. Cable modeled using a single π-section (triangle markers) and five π-sections (dashed).

the same impedance characteristic as when using multiple sections.

Fig. 3.5 shows the equivalent impedance seen by a VSC converter connected to a 250 km cable. The cable is considered as part of a 400 kV system and its parameters per unit of length are shown in [49]. Two models are considered for the cable. One using a single π-section for the whole 250 km section, marked with a solid line and triangular markers in Fig. 3.5, and one using five cascaded π-sections – one for every 50 km – marked with a dashed line.

The value of the equivalent capacitance for a 50 km section $C_{\pi-50km}$, i.e., $4.76\,\mu F$ for the cable data provided in [49], is used as a reference point and the value of the output capacitor of the VSC is varied according to $C = n \cdot C_{\pi-50km}$.

It can be seen that, even for values as small as $n = 20$, the difference between the two models starts to be insignificant, the high frequency peaks being dominated by the output capacitor. For values of n in the range of hundreds, the size of the VSC's output capacitor arrives at a few mF (values that are typically found in the literature) and, as it can be seen in Fig. 3.5, the two models for the cable are almost

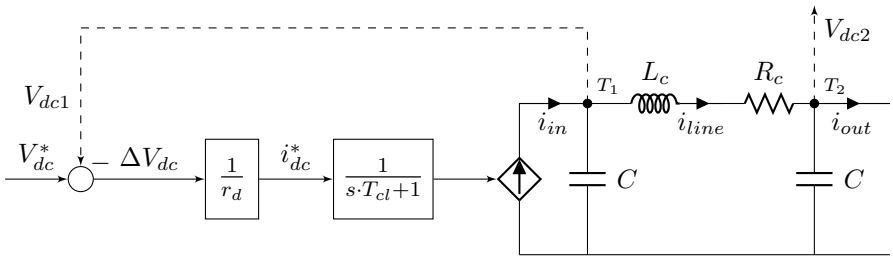

Fig. 3.6: Block diagram of DC-bus voltage controlled by droop with the load connected at the end of cable.

identical.

This being said, if we consider the converter at T1 in Fig. 3.4 to be droop controlled and we model the cable through a single π-section with the shunt capacitors lumped together with the dc-bus capacitors of the two converters connected at each end of the line, the system in Fig. 3.6 is obtained.

The behavior of this system will be considerably different from the one presented in the previous section, mainly due to the low frequency resonance appearing between the parasitic cable inductor and the large capacitor at the output of the VSC.

Fig. 3.7 shows a typical evolution of the current i_{in} injected by the converter at T1, as well as of the voltages at the two ends of the cable for a step in the load current i_{out}. The scenario discussed in the previous section, in which the cable was not included in the analysis, is added to the figure with a dashed green line for comparison.

The first thing that we should notice from Fig. 3.7 is that the voltages at the two ends of the cable have now different steady state values. The deviation in V_{dc1} is dictated only by the droop resistance r_d; meanwhile, the voltage V_{dc2} at T2 experiences an additional offset due to the current flowing through the resistance R_c of the connecting line.

The dynamic behavior of the system is also greatly influenced by the presence of the cable. Larger transients, in both the injected current and the two dc-voltages, can be observed in Fig. 3.7. As expected, the largest voltage overshoot appears at

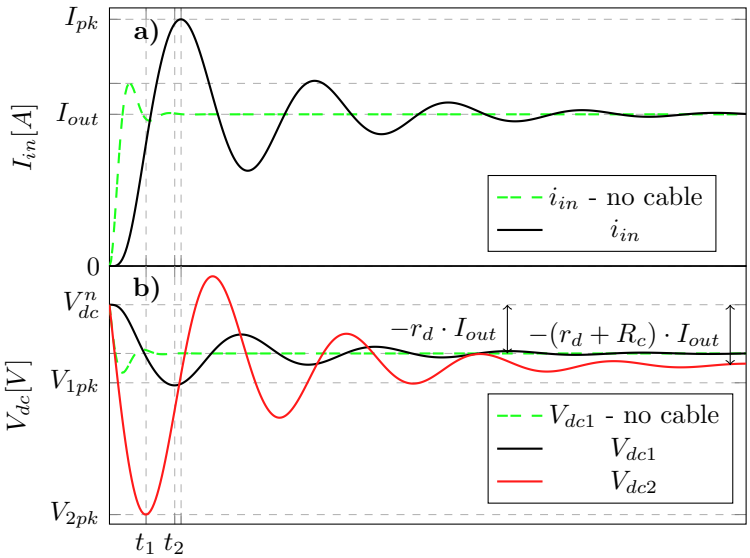

Fig. 3.7: Evolution of the a) current injected by the VSC and b) dc voltage at the two ends of the cable after a step in the load current.

the terminal where the load change occurred; for the case presented in Fig. 3.7, this is the overshoot of the voltage at T2, namely V_{2pk}.

The method described in the previous section for calculating the overshoots in the system cannot be applied for obtaining V_{1pk} nor V_{2pk}; this is due to the fact that the transfer functions from i_{out} to V_{dc1} and V_{dc2}, for the complete system, are of high order and cannot be easily approached analytically.

An interesting aspect to analyze is the dynamic evolution of V_{dc2} for different values of droop resistance used in the voltage-control strategy at T1. Fig. 3.8 shows the evolution of V_{dc2} after a step change in the load current i_{out} for different values of droop resistance used at T1. The case when V_{dc1} is considered a constant voltage source is added for comparison.

The first thing to note is that, as the size of the droop resistance used at T1 increases, also the steady state deviation from the nominal voltage increases. Another important aspect to notice is the effect of the droop resistance on the attenuation of the voltage oscillations. Using larger values for the droop resistance at T1 will damp faster the voltage oscillations that appear at T2. It can be seen in Fig. 3.8

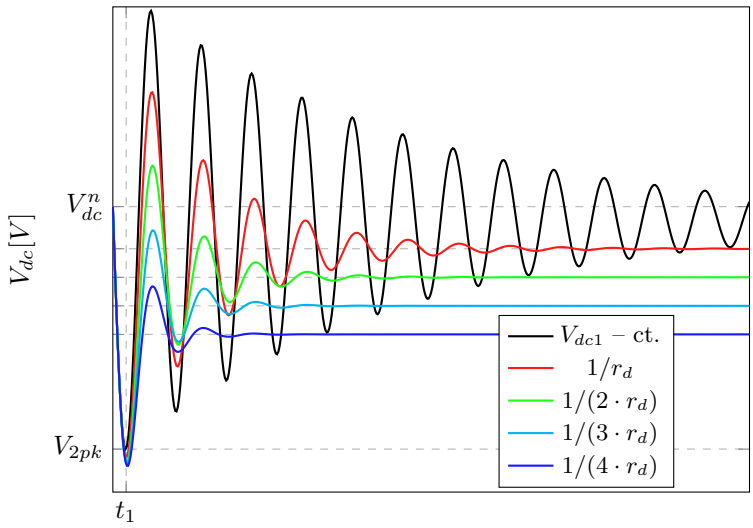

Fig. 3.8: Evolution of the dc-bus voltage V_{dc2} for different values of droop resistance used in the voltage control at T1 .

that V_{dc2} is the most oscillatory when the voltage at T1 is maintained constant. This is in accordance with our previous observation, as constant voltage control can be theoretically seen as a droop controller with r_d equal to zero.

According to Fig. 3.8, while even a small increase in the size of the droop resistance has a considerable effect on the attenuation of voltage oscillations, they have almost no effect on the firs peak of the transient V_{2pk}. Therefore, we can assume that V_{2pk} is independent of the size of the droop resistance for small values of r_d. In this way, by considering the system connected to a constant voltage source at T1, as shown in Fig. 3.9, we can obtain an analytical approximation for V_{2pk}.

For the system presented in Fig 3.9, the relationship between V_{dc2} and i_{out} is described by (3.11) and (3.12). The equivalent transfer function corresponds to a second order with an added zero and, for this type of transfer function, the methodology presented in Appendix B can be used in order to calculate its overshoot.

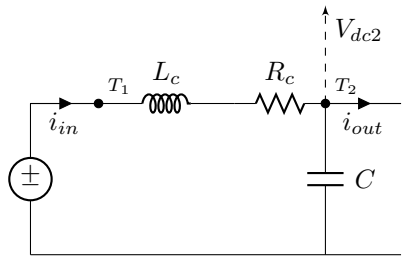

Fig. 3.9: Perturbation at the end of a cable connected to a voltage source

$$\begin{aligned} V_{dc2} &= i_{out} \cdot H_c(s) \\ H_c(s) &= k \cdot \frac{\omega_n^2 \cdot (a \cdot s + 1)}{s^2 + 2\xi\omega_n s + \omega_n^2} \end{aligned} \tag{3.11}$$

$$\begin{aligned} a &= \frac{L_c}{R_c}, \quad \omega_n = \sqrt{\frac{1}{L_c \cdot C}} \\ k &= R_c, \quad \xi = \sqrt{\frac{R_c^2 \cdot C}{4 \cdot L_c}} \end{aligned} \tag{3.12}$$

The analysis of a system composed of two terminals connected by a cable, presented in this section, provides some insight on how the different parameters affect the behavior of the system. This knowledge can be used as a starting point for sizing the dc-bus capacitors of the system. For a meshed MTDC network these methods have to be complemented by simulations in a software like Matlab/Simulink or PSCAD, as the dynamics of the voltage at each point in the power system are highly inter-coupled, resulting in a more complex behavior than the one described here.

3.4 Effect of C and T_{cl} on the system dynamics

The analysis of the the droop resistance effect on the voltage oscillation in Fig. 3.8 provided some useful insight on how tuning this parameter will affect the system response. However, besides the value of the droop resistance, we identified two other important parameters involved in the dynamics of the system. The first one was the time constant of the internal current loop of the converter T_{cl}.

The effect of T_{cl} on the voltage was rather clear when analyzing the behavior of a single converter: the smaller T_{cl} is in comparison with $r_d \cdot C$, the response of the system will resemble more the one of a first order system . The intuition on the impact of T_{cl} on the voltage dynamics after the cable is added to the analysis is not so straight forward.

Fig. 3.10 shows the evolution of the voltage at T2 for the two-point system presented previously in Fig. 3.4. The voltage at T1 is regulated using droop control and the time constant T_{cl} of the internal current loop is varied from very small values to very large values. The case when the voltage at T1 is constant is added to the plot as a reference-base for comparison.

The first thing that has to be noticed is that, for very large values of T_{cl}, that is to say if the current loop of the converter is very slow, the voltage response is considerably distorted. If the speed of the the current loop is increased, i.e., the smaller T_{cl} is, the response of the system approaches the one of a damped second order system with the frequency of the oscillations equal to the constant voltage case.

Also, it is interesting to observe that, regardless of how fast the current loop at T1 is, it has very little effect on the first voltage sag V_{2pk}.

This can be better understood by looking at the bode diagram of the transfer function between V_{dc2} and i_{out}, as shown in Fig. 3.11. First, let us analyze the case when the voltage at T1 is constant. In this case, a single resonance peak can be seen in the bode diagram and it is given by the interaction between the parasitic inductance of the cable and the output capacitor at T2, as approximated by (3.13).

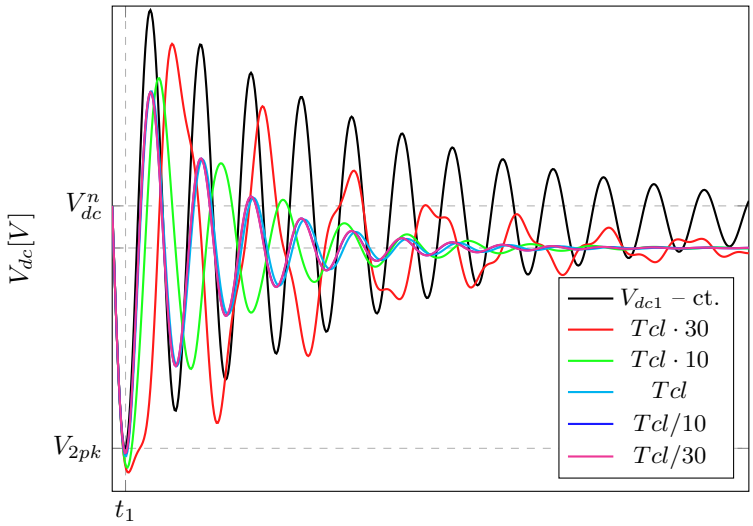

Fig. 3.10: Evolution of the dc-bus voltage V_{dc2} for different values of time constant T_{cl} used in the voltage control at T1.

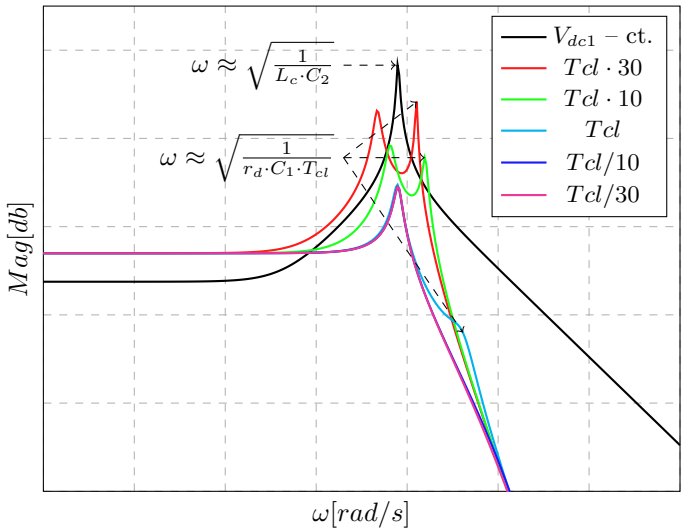

Fig. 3.11: Bode diagram of the transfer function between i_{out} and V_{dc2} for different values of time constant T_{cl} used in the voltage control at T1.

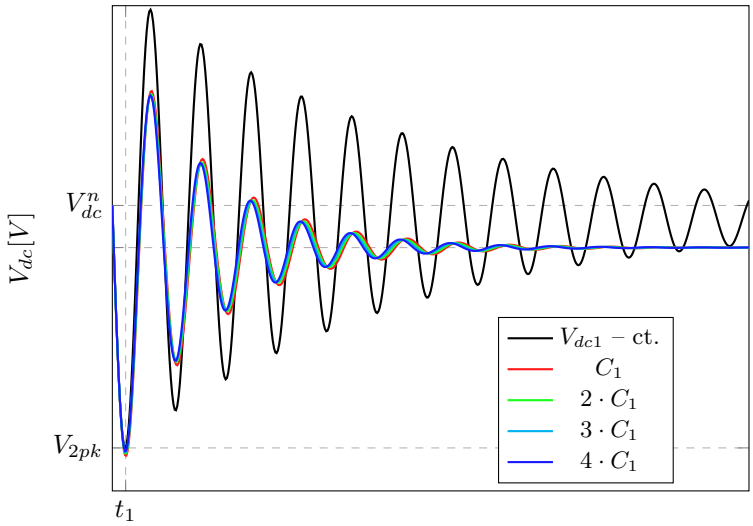

Fig. 3.12: Evolution of the dc-bus voltage V_{dc2} for different capacitor values C_1 used at the output of T1.

The steady state is influenced only by the resistance of the cable.

$$\omega \approx \frac{1}{\sqrt{L_c \cdot C_2}} \tag{3.13}$$

In the cases when droop control is employed at T1, for large values of T_{cl}, another resonance peak can be observed in Fig. 3.11. This is mainly due to the poorly damped control of V_{dc1}.

We have shown in Section 3.2 that for a single converter, when the voltage loop is closed around the slow current loop, oscillations are introduced into the system at the frequency defined in (3.14). We can approximate the frequency of the second peak to this value, but for large T_{cl} this would be a rather rough approximation. This is because that, while the second resonance peak is mainly influenced by the control at T1, the cable dynamics and the dynamics of the voltage at T1 are not completely separable; the closer the two resonating frequencies, the more they will influence each other.

$$\omega \approx \frac{1}{\sqrt{r_d \cdot C_1 \cdot T_{cl}}} \tag{3.14}$$

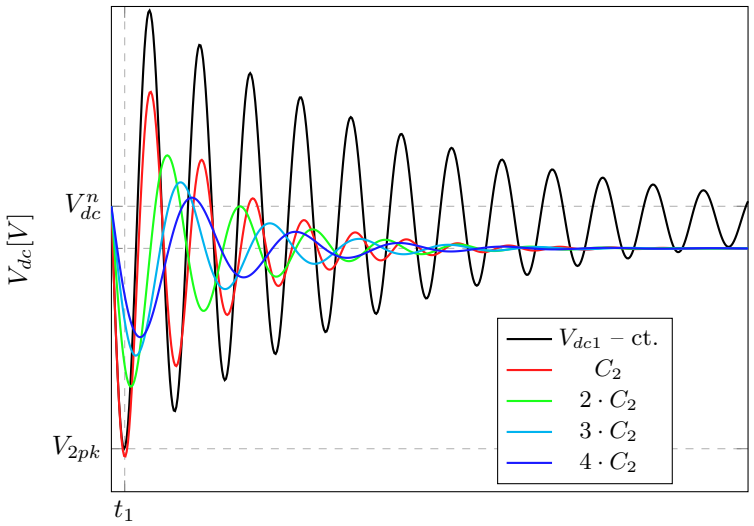

Fig. 3.13: Evolution of the dc-bus voltage V_{dc2} for different capacitor values C_2 used at the output of T2.

It can be observed that, as T_{cl} decreases, the second resonance peak flattens and its influence on the first resonance peak disappears. As can be seen in Fig. 3.11 the blue and magenta curve have only one resonance peak at the natural oscillating frequency of the cable.

What needs to be taken from all this is that, in order to avoid introducing additional oscillations into the system, T_{cl} has to be chosen small enough so the control of the voltage is faster than the natural oscillations of the cable connecting the two terminals.

The same thing is also expected when analyzing the impact of the capacitor size connected at T1, i.e., C_1, on the voltage evolution at T2. As seen before, C_1 appears only in the expression of the second resonance peak. Similar to T_{cl}, too small values would introduce additional oscillations into the system, as the two resonance peaks are getting closer together. Increasing C_1 will remove the second resonance peak, but, overall, it will have almost no effect on the first voltage sag experienced by V_{dc2}, as it can be seen in Fig. 3.12.

Looking at the impact of r_d, C_1, and T_{cl} on the voltage overshoot at T2, we can

safely conclude that there is not much that can be done when sizing the parameters for T1 in order to reduce V_{2pk}.

Given a fixed cable length connecting the two terminals, the only way to reduce V_{2pk} is by increasing the capacitor size connected at the T2. Fig. 3.13 shows the evolution of V_{dc2} for different values of capacitance used at T2. As expected, the larger the size of the capacitor, the smaller the first voltage dip will be. Also, as the size of C_2 increases, the damping of the system is improved as, now, there is more *inertial energy* closer to the load terminal.

3.5 Study case

In order to show how the presented methods can be used in the sizing of the primary control, we will take an arbitrary network and provide a step by step methodology in order to address some of the issues that might appear. Starting from the network topology, we will first provide an initial design based on the information available at the moment in the literature and then we will improve this design by making use of the methods shown previously.

3.5.1 Network topology

For our study case, we considered a hypothetical five-terminal dc-network proposed in [61] and reproduced here in Fig. 3.14. The reason why we selected this network is because its highly meshed structure, combined with the isolated position of T5, will yield some interesting conclusions further on. Since our work is focused only on the behavior of the dc-network, we did not include the sources of energy to which the power converters are connected. Either the primary source is an ac-grid, a wind turbine, a PV-plant, or a battery it does not matter to our analysis; the only important aspect is the speed of the internal current loop and the behavior of each terminal, i.e., whether the terminal is controlled using a droop strategy or as constant power.

In the original work that proposes the network of Fig. 3.14, two of the VSC-HVDC terminals (i.e., T3 and T5) are operated in constant power control mode, whereas the other three terminals participate in the dc voltage droop control. The

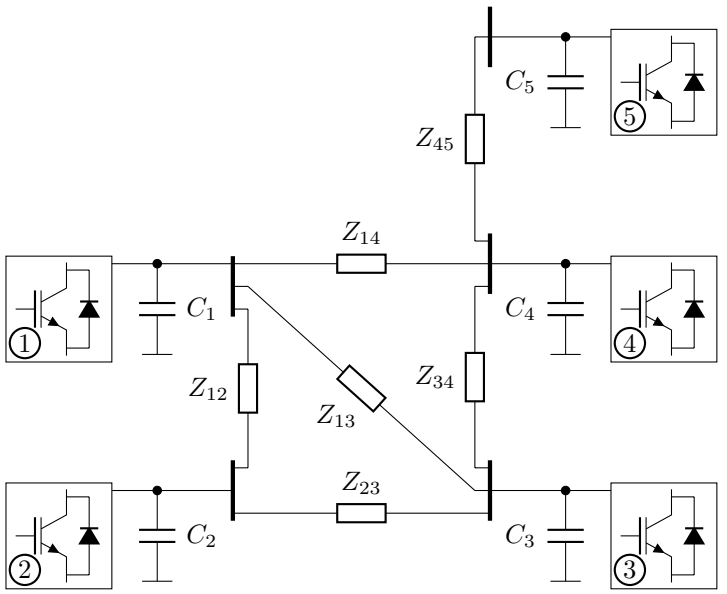

Fig. 3.14: Meshed MTDC network with droop-based primary control used in the simulation scenarios.

Table 3.1: MTDC network parameters

Terminal No.	T1	T2	T3	T4	T5
P_N[MW]	900	800	1000	750	1200
V_{dc}^n[kV]	400	400	400	400	400
Node Type	Droop	Droop	ct. P	Droop	ct. P

nominal operating voltage of the network is considered to be 400 kV. These aspects, together with the power ratings of each terminal, shown in Table 3.1, have been considered as the premises of our analysis.

The length of the cables connecting the five terminals used in [61] has also been maintained and, in order to obtain their equivalent π-models, the values of resistance, inductance, and capacitance per unit of length given in [49] have been used. In this way the equivalent cable models shown in Table 3.2 were obtained.

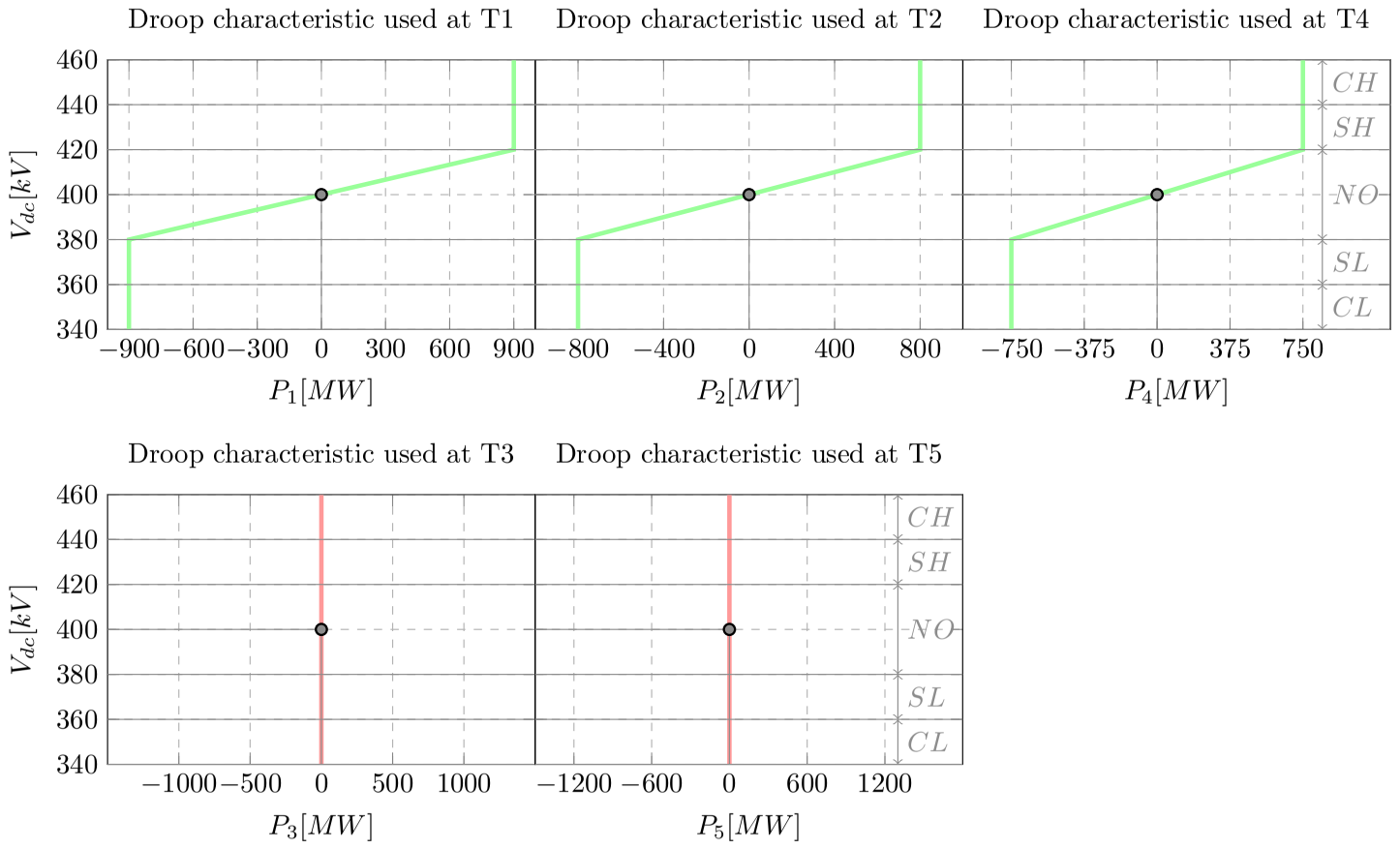

Fig. 3.15: Droop characteristics for the five converters

Table 3.2: MTDC network cables - equivalent π-model parameters

Cable	Z_{12}	Z_{13}	Z_{14}	Z_{23}	Z_{34}	Z_{45}
l[km]	80	200	125	160	160	250
R[Ω]	0.76	1.9	1.19	1.52	1.52	2.38
L[H]	0.169	0.422	0.264	0.338	0.338	0.528
C[μF]	7.624	19.06	11.91	15.25	15.25	23.83

3.5.2 Initial design

Output capacitor size

Given the initial structure of the network and the power rating of each terminal, the remaining hardware parameters of the initial design are the size of the capacitors used at the output of each of the converters, i.e, $C_1 ... C_5$. The literature on this topic is highly insufficient. The only resource found regarding this aspect is the work of the CIGRE work-group on HVDC and Power Electronics in [49]; here, the size of the output capacitor is linearly increased with the power rating of the converter so that a per-unit capacitance of 60 ms is connected at each terminal. We used the same approach for the initial sizing of the dc-bus capacitors. Taking the rated power of each converter we can pass from p.u. values to farads by making use of (3.15). The values obtained for the five capacitors are shown in Table 3.3.

$$C = \frac{\Delta t \cdot P}{0.5 \cdot V_{dc}^2} \tag{3.15}$$

Table 3.3: Capacitors connected at the output of the VSCs - CIGRE values

Terminal No.	T1	T2	T3	T4	T5
C[mF]	0.675	0.6	0.750	0.5625	0.9

Voltage operating bands

Once the hardware parameters have been set, the operating voltage bands used in the primary control have to be decided. The typical allowed voltage deviation for

Table 3.4: Operating bands used for primary control

Operating Band	%	kV
CL	5	340 – 360
SL	5	360 – 380
NO	10	380 – 420
SH	5	420 – 440
CH	5	440 – 460

normal power flow encountered in the literature is $\pm 5\%$, as reported in [45, 60, 76]. We used the same value for the NO band and allowed another 5% for each of the safety and critical bands. Overall, this sets the maximum allowed voltage V_{dc}^{ch} at 15% higher than the nominal; and similarly, the lowest allowed voltage V_{dc}^{cl} at 15% lower than the nominal.

In practice, V_{dc}^{ch} and V_{dc}^{cl} should be selected based on the rating and overvoltage capabilities of the converters connected to the network. Since such information is not readily available for large power converters, we settled for the value of 15%, given the fact that works such as [10] show voltage transients 20% higher than the nominal voltage for high power multi-modular converters.

Given the operating bands summarized in Table 3.4, we can build the droop characteristics for the five converters as described in the previous chapter. These characteristics are shown in Fig. 3.15: T1, T2, and T4 are controlled by bidirectional droops and are responsible for regulating the voltage. Meanwhile, T3 and T5 are controlled as constant power nodes, which corresponds to a critical droop characteristic.

Time constant of the current loop T_{cl}

The achievable speed of the current loop is an important parameter in the sizing of the system and can vary substantially depending on the topology of the converter and the control structure.

Classic two level converters have to reduce their switching frequency as the power rating increases due to the switching losses and this, unavoidably, reduces

the speed of the current loop. On the other hand, modern multi-modular converters will respond faster due to the reduced filter size.

For our analysis, we imposed the bandwidth for the current loop to be at 200 Hz, as it can be considered achievable also for converters switching at very slow frequency.

3.5.2.1 Steady state analysis

When analyzing the steady state interaction between the various droops in Chapter 2 we always ignored the resistance of the connecting cables. In this way, the steady state value of the voltage was easily predicted as it was influenced only by the droop gains. In practice, besides the droop values, the network topology also influences the operating point reached by the voltage at each bus; therefore, estimating the steady state voltage is not so straight forward as before.

The method developed by Haileselassie in [44] addresses exactly this issue, but before we can see how this can be applied, we need to pass all the involved parameters to vector format.

The voltage, treated in Chapter 2 as a unique value for all the network, now becomes a vector $\mathbf{V_{dc}}$ that contains the voltage at each bus in the network. In order to differentiate scalars from vectors or matrix quantities, boldface symbols will be used for the latter throughout the thesis. Similarly, as shown in (3.16), $\mathbf{P}$ and $\mathbf{P}^*$ represent the power measurement and reference for each terminal and $\mathbf{V^*_{dc}}$ represents the voltage reference for each unit involved in the primary control. For the moment, $\mathbf{V^*_{dc}}$ is considered equal to the nominal voltage of the network. As it will be seen in the next chapter, $\mathbf{V^*_{dc}}$ is handled by the secondary control in order to regulate the voltage profile of the network and to restore the voltages to the NO band after transients.

$$\mathbf{P} = \begin{bmatrix} P_1 \\ \vdots \\ P_n \end{bmatrix} \mathbf{V_{dc}} = \begin{bmatrix} V_{dc1} \\ \vdots \\ V_{dcn} \end{bmatrix} \mathbf{P}^* = \begin{bmatrix} P_1^* \\ \vdots \\ P_n^* \end{bmatrix} \mathbf{V^*_{dc}} = \begin{bmatrix} V^*_{dc1} \\ \vdots \\ V^*_{dcn} \end{bmatrix} \tag{3.16}$$

When working with networks, a method for describing the topology of the network is required. While graph theory offers several mathematical tools for quantifying node incidence, the nodal admittance matrix $\mathbf{Y}$ is the most used in power systems analysis. In dc systems, resistance is the steady state characteristic of the connecting cables. Therefore, the admittance matrix is replaced by the conductance matrix $\mathbf{G}$, defined in (3.17), where $g_{ij}$is the equivalent conductance of the cable connecting node i to node j.

$$G_{ij} = \begin{cases} \sum_{j=1}^{n} g_{ij} & \text{if } i = j \\ -g_{ij} & \text{if } i \neq j \text{ and } i \text{adjacent to } j \\ 0 & \text{if } i \neq j \text{ and } i \text{not adjacent to } j \end{cases} \tag{3.17}$$

The droop gains are also grouped in a vector $\mathbf{K_d}$ as shown in (3.18).

$$K_d^i = \begin{cases} \frac{1}{r_d} & \text{if node } i \text{ is droop controlled} \\ 0 & \text{if node } i \text{ is constant power} \end{cases} \tag{3.18}$$

Another important quantity when analyzing the steady state behavior of dc-networks is the Jacobian matrix of the grid defined in (3.19). $\mathbf{J_{dc}}$ relates the small deviations in voltage to the deviations in power flow and it is obtained by differentiating the power flow equations of each terminal in the network with respect to the nodal voltages. A more simple way to calculate the Jacobian, making use of the quantities defined so far, is provided in [61] and reproduced here in (3.20).

$$\mathbf{J_{dc}} = \frac{\partial \mathbf{P}}{\partial \mathbf{V_{dc}}} \tag{3.19}$$

$$\mathbf{J_{dc}} = diag\left(\mathbf{V_{dc}}\right) \cdot \mathbf{G} + diag\left(\mathbf{G} \cdot \mathbf{V_{dc}}\right) \tag{3.20}$$

Having defined all the required matrices and vectors, the deviations in the network voltages $\Delta\mathbf{V_{dc}}$ – given a certain deviation in the power reference $\Delta\mathbf{P}^*$ – can be calculated as shown in (3.21). Using this relationship, we can calculate how much the voltage will deviate from the nominal value if the power reference for any of the

terminals changes.

$$\Delta \mathbf{V_{dc}} = [\mathbf{J_{dc}} + diag\,(\mathbf{K_d})]^{-1} \cdot \Delta \mathbf{P}^* \tag{3.21}$$

Taking the values of the cable resistances for the network presented in Fig. 3.14, we obtain the conductance matrix shown in (3.22).

$$\mathbf{G} = \begin{bmatrix} 2.6842 & -1.3158 & -0.5263 & -0.8421 & 0 \\ -1.3158 & 1.9737 & -0.6579 & 0 & 0 \\ -0.5263 & -0.6579 & 1.8421 & -0.6579 & 0 \\ -0.8421 & 0 & -0.6579 & 1.9211 & -0.4211 \\ 0 & 0 & 0 & -0.4211 & 0.4211 \end{bmatrix} \tag{3.22}$$

For each terminal we will calculate the steady state voltage for different loading scenarios of the network. First, we will consider the converter at T3 operating at full load, then the converter at T5, and finally both the converters operating at the rated load values, as shown by the corresponding vectors in (3.23).

$$\mathbf{V_{dc}} = \begin{bmatrix} 400 \\ 400 \\ 400 \\ 400 \\ 400 \end{bmatrix} \text{kV}\, \Delta \mathbf{P_1^*} = \begin{bmatrix} 0 \\ 0 \\ 1000 \\ 0 \\ 0 \end{bmatrix} \text{MW}\, \Delta \mathbf{P_2^*} = \begin{bmatrix} 0 \\ 0 \\ 0 \\ 0 \\ 1200 \end{bmatrix} \text{MW}\, \Delta \mathbf{P_3^*} = \begin{bmatrix} 0 \\ 0 \\ 1000 \\ 0 \\ 1200 \end{bmatrix} \text{MW} \tag{3.23}$$

Using (3.18) and (3.20) we can calculate the remaining terms of equation (3.21),

Table 3.5: Analytical estimation of the steady state voltages compared with simulation results for different scenarios of network loading

	$\Delta\mathbf{P}_1^*$		$\Delta\mathbf{P}_2^*$		$\Delta\mathbf{P}_3^*$	
	Analytical estimation	Simulation results	Analytical estimation	Simulation results	Analytical estimation	Simulation results
V_{dc1} [kV]	391.8886	391.8606	390.5585	390.3541	382.4471	382.2093
V_{dc2} [kV]	391.8305	391.8011	390.8802	390.6901	382.7106	382.4906
V_{dc3} [kV]	390.4723	390.4096	390.1374	389.9135	380.6097	380.2698
V_{dc4} [kV]	391.7811	391.7507	389.0577	388.7842	380.8388	380.4944
V_{dc5} [kV]	391.7811	391.7507	381.9327	381.3102	373.7138	372.8492

i.e., $\mathbf{K_d}$ and $\mathbf{J_{dc}}$.

$$\mathbf{K_d} = \begin{bmatrix} 45 \\ 40 \\ 0 \\ 37.5 \\ 0 \end{bmatrix} \frac{\text{MW}}{\text{kV}} \tag{3.24}$$

$$\mathbf{J_{dc}} = \begin{bmatrix} 1073.6842 & -526.3158 & -210.5263 & -336.8421 & 0 \\ -526.3158 & 789.4737 & -263.1579 & 0 & 0 \\ -210.5263 & -263.1579 & 736.8421 & -263.1579 & 0 \\ -336.8421 & 0 & -263.1579 & 768.4211 & -168.4211 \\ 0 & 0 & 0 & -168.4211 & 168.4211 \end{bmatrix} \frac{\text{MW}}{\text{kV}} \tag{3.25}$$

Using (3.21) together with (3.22)–(3.25), we can calculate the steady state network voltages for the three cases. Table 3.5 shows the obtained results compared with the steady state values obtained by simulating the corresponding load-flow scenarios in Matlab/Simulink. The largest difference between the values obtained from (3.21), when compared with the simulation results, is of 0.23%, and can be accounted to numerical imprecision, especially when calculating the inverse of the $\mathbf{J_{dc}} + diag\,(\mathbf{K_d})$ term.

Analyzing the steady state behavior of the network voltages is important in order to asses if the height of the operating bands has been properly selected. As can be observed from Table 3.5, when only one of the loads is connected – either at T3, either at T5 – the voltages of the network will settle in the selected NO band, i.e., 380 kV – 420 kV. On the other hand, when the network is fully loaded (load at T3 and at T5 connected at the same time) the voltage at T5 will go outside of the NO band.

This goes against our definition of the operating bands: the NO band should include all normal power flow scenarios, meanwhile, the safety bands are reserved for transients. However, there is very little that can be done about it, as the steady state voltage is influenced by the structure of the network (which is usually fixed) and by the values of the droop resistances. One could decrease the value of the droop resistances in order to reduce the steady state voltage offset, but, as it was shown previously in Fig. 3.8 of Section 3.3, this will make the system more oscillatory, creating problems during transients.

Another option is to have a secondary control layer that periodically evaluates the state of the network and restores the voltages to the NO band. The behavior of the secondary control and how it can optimally recalculate the operating point of the primary is addressed in the next chapter.

3.5.2.2 Dynamic analysis

From the steady state point of view this initial design seems to be satisfying. However, this is not the case when we look at the dynamic behavior of the system. Fig. 3.16 shows the evolution of the nodal voltages and power injections at each terminal after a step in the load power at T5.

Initially, there is no power flow in the network and all the voltages are at the nominal value; then, after 0.5 seconds, the power at T5 is increased from 0 to 1200 MW. While step increases in the load are not typical events in a power system (usually the power is slowly ramped up or down), a sudden decrease of load can occur as a result of a converter trip or other faults in the network. Therefore, analyzing the transients for step changes makes sense; moreover, the response to step changes

is the standard approach in control theory for investigating the dynamic behavior of a system.

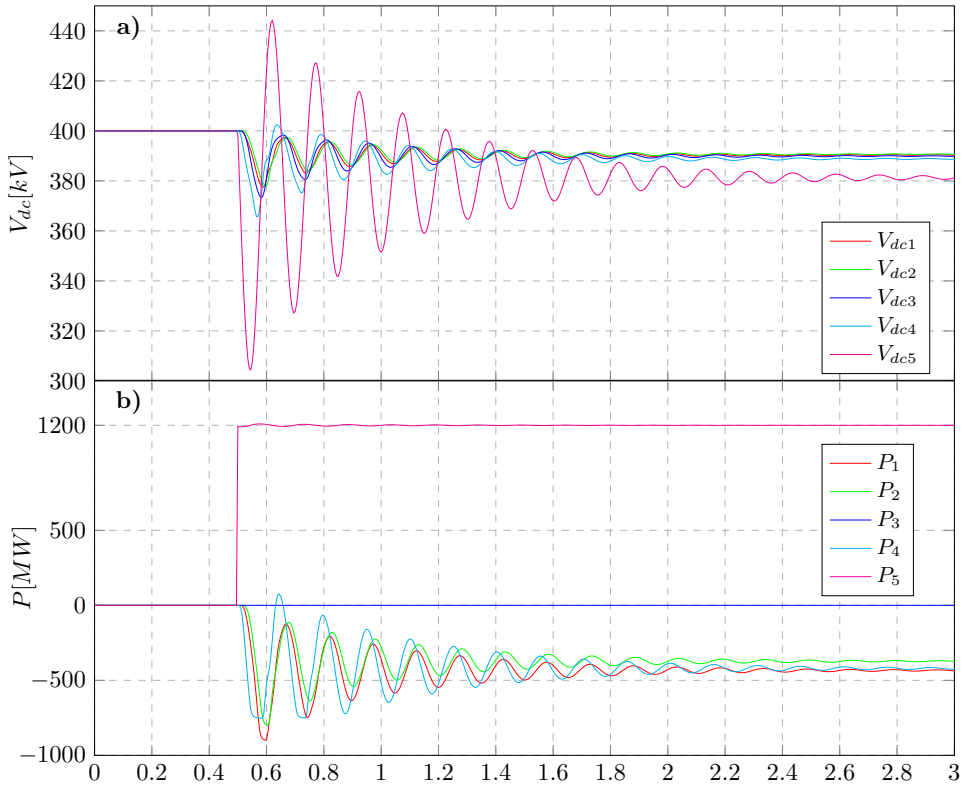

Fig. 3.16: 1200 MW step in the load power at T5. Evolution of the a) nodal voltages and b) power injections during transients.

A few things have to be noticed in Fig. 3.16. Firstly, the steady state voltages reach the values predicted in the previous section, remaining inside the NO band. Secondly, we can see that V_{dc5} has a very oscillatory behavior and the first two peaks are not only outside of the SL band, but also outside of the CL band, i.e., 340 kV – 360 kV. Such a large transient is unacceptable and it could damage the power converter in case of a load trip.

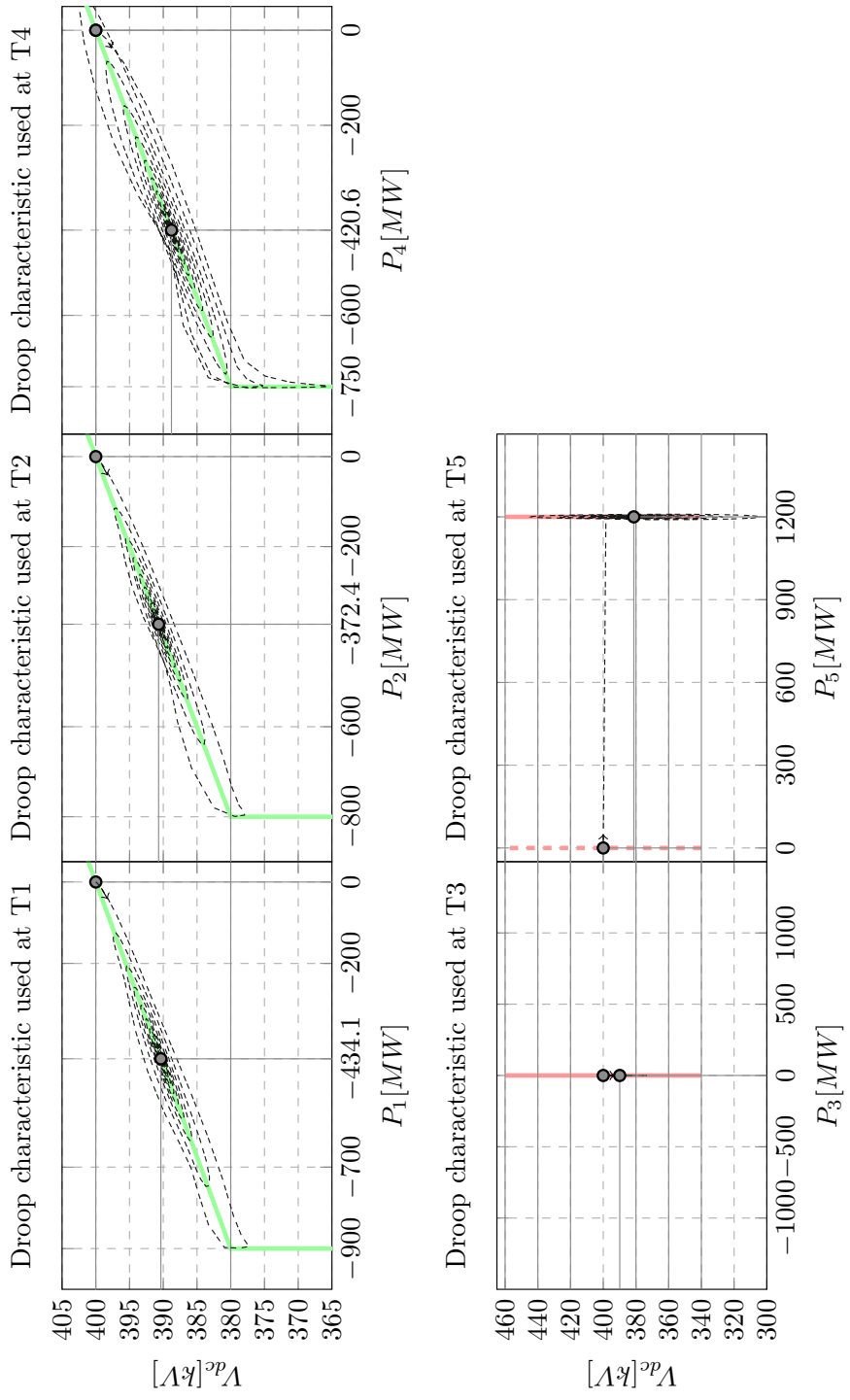

Fig. 3.17: 1200 MW step in the load power at T5. Evolution of the droop operating points.

It is interesting to see how the operating point of each droop evolves during transients. In Chapter 2 we always showed the operating point linearly sliding along the droop characteristic. As can be seen in Fig. 3.17, this is not really the case. After the load change, the operating point of each droop follows a rather complicated trajectory before reaching the new value. The power saturation of the converter at T4 during the transient is more obvious in this representation and also the violation of the operating bands by the operating point of droop 5.

Looking at the structure of the network, an oscillatory behavior of V_{dc5} was expected. The isolated position of the terminal, the long cable connecting it to T4 and its high power rating (compared with the power rating of T4) are all clues that indicate that V_{dc5} will be rather sensitive to any power change. As we saw in the previous section, the best way to reduce the peak of the voltages during transients is to increase the capacitor size. We will present next a sizing method that takes into account the height of the operating bands chosen for the primary control.

3.5.3 Sizing of output capacitors

In Section 3.3 we have shown that for a point to point connection, the first peak in the voltage transient, after a step in the current at the end of the cable, is independent of the droop resistance. As argued earlier, this is true only if the value of the droop resistance is maintained inside reasonable practical values and does not hold for theoretical values such as $r_d \to \infty$. This simplification allowed us to consider the cable connected to a constant voltage source and to estimate the overshoot in the voltage by approximating the system with a second order system with an additional zero.

For such a system, the peak unit-increase in voltage after a unit-increase in current – quantity that we will name *peak impedance* Z_{pk}– can be calculated using the formulas given in the Appendix B, as shown in (3.26). Some books on power systems analysis, such as [77], define a similar quantity – named *characteristic line impedance* Z_c– when presenting the traveling wave equations and the voltage and current transients. The main difference between Z_{pk} and Z_c is that in the definition of Z_{pk} we also take into account the resistance of the line, which in dc-systems is

more significant than in ac-systems. Then, we compute Z_{pk} in the time domain by taking the ratio between the current and the peak voltage in order to obtain a very precise description.

The terms that appear in (3.26) depend only on the parameters of the cable (R_c, L_c) and the total capacitance connected at the end of the cable (output VSC capacitor + cable parasitic capacitance C_c) and they are defined either in (3.12), either can be easily deduced by making use of the definitions listed in the Appendix B.

$$Z_{pk}(R_c, L_c, C_{tot}) = -k \cdot \left(1 - e^{-\xi \cdot \omega_n \cdot t_{pk}} \left(\cos\left(\omega_d \cdot t_{pk}\right) + \beta \cdot \sin\left(\omega_d \cdot t_{pk}\right)\right)\right) \quad (3.26)$$

Z_{pk} is a useful quantity as it relates the peak voltage with the current injection at a terminal. If a terminal is initially at a voltage V_{dc} and suddenly a load current I is subtracted from that terminal, the peak in the voltage can be calculated as shown in (3.27).

$$\begin{aligned} \Delta V &= Z_{pk} \cdot I \\ V_{pk} &= V_{dc} - \Delta V \end{aligned} \quad (3.27)$$

However, it is quite often that in power systems we know the injected or absorbed power at a terminal and not the current.In this case, the linear relation given by the peak impedance becomes a quadratic equation as shown in (3.28), where P is the load power at the terminal and V_{dc} is the voltage before P is connected.

$$\begin{aligned} \Delta V &= Z_{pk} \cdot \frac{P}{V_{pk}} \\ V_{pk}^2 - V_{pk} \cdot V_{dc} + P \cdot Z_{pk} &= 0 \end{aligned} \quad (3.28)$$

We can apply this approach in our study case in order to estimate the peak voltage at terminal 5 when a load of 1200 MW is suddenly connected. For this,

we have to firstly obtain the parameters required for calculating Z_{pk}. Since there is only one cable connected to T5, namely Z_{45} (see Table 3.2), it is rather easy to estimate the terms for calculating the peak impedance, as shown in (3.29). Here, we used the notation $Z_{ij}.R$, $Z_{ij}.L$, and Z_{ij}.C to refer to the equivalent π-model parameters of the cable connecting node i to node j. Z_{ij} has been defined earlier in Table 3.2.

$$\begin{aligned} R_c &= Z_{45}.R \\ L_c &= Z_{45}.L \\ C_{tot} &= C_5 + Z_{45}.C \end{aligned} \tag{3.29}$$

Using the values shown in (3.29) together with (3.26) and (3.28) we obtain that, if the network is in zero power-flow state (i.e., all the bus voltages are equal to the nominal voltage of 400 kV) and a load of 1200 MW is suddenly connected at T5, then V_{dc5} will reach a minimum point of $V_{pk5} = 303.35$ kV. This is exactly the scenario shown previously in Fig 3.16 and, as it can be seen, the peak in the voltage at T5 (i.e., the lowest value of V_{dc5}) is below 305 kV, so our estimation is not that far off.

Given the fact that we now have a direct relationship between C_5 and V_{pk5} we can plot one against the other, as seen in Fig. 3.18. In this plot, we can see how the peak voltage at T5 during the sudden connection of a 1200 MW load reduces exponentially as C_5 increases. It can be seen from the plot, that in order for the overshoot to be inside the defined CL band we need a capacitor of at least 2 mF and if we want V_{pk5} to be inside the SL band, C_5 has to reach a value larger than 4 mF.

This method for estimating the voltage overshoot can be applied also to the other terminals of the network. However, the extrapolation is not immediate, as the other terminals of the network are connected to more than one cable. A good approximation can be obtained if we consider all the cables connected to a terminal as being connected in parallel. In this way, the parameters required for calculating Z_{pk} at each terminal can be computed from the corresponding cable parameters, as summarized in Table 3.6.

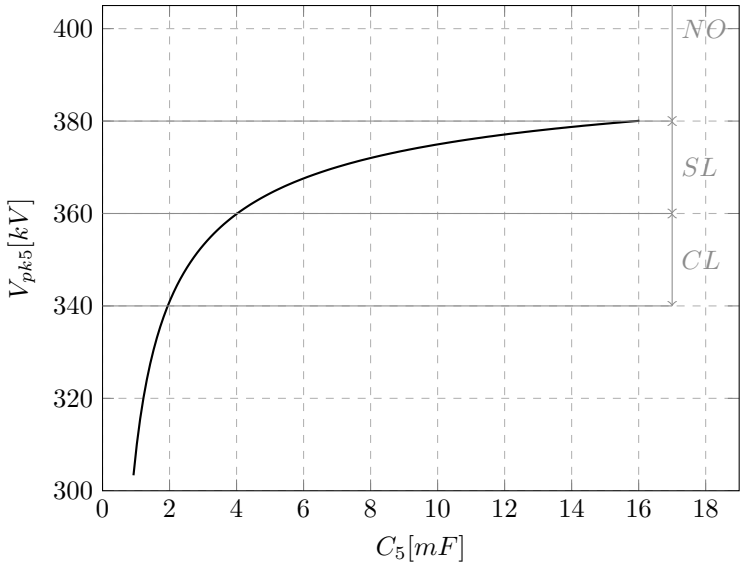

Fig. 3.18: Peak voltage at T5 during 1200 MW load step for different values of C_5.

Table 3.6: Parameters required for calculating Z_{pk} for each terminal.

	R_c	L_c	C_{tot}	Z_{pk}
T1	$Z_{12}.R \| \| Z_{13}.R \| \| Z_{14}.R$	$Z_{12}.L \| \| Z_{13}.L \| \| Z_{14}.L$	$C_1 + Z_{12}.C + Z_{13}.C + Z_{14}.C$	10.8542
T2	$Z_{12}.R \| \| Z_{23}.R$	$Z_{12}.L \| \| Z_{23}.L$	$C_2 + Z_{12}.C + Z_{23}.C$	13.5576
T3	$Z_{23}.R \| \| Z_{13}.R \| \| Z_{34}.R$	$Z_{23}.L \| \| Z_{13}.L \| \| Z_{34}.L$	$C_3 + Z_{23}.C + Z_{13}.C + Z_{34}.C$	12.4040
T4	$Z_{14}.R \| \| Z_{34}.R \| \| Z_{45}.R$	$Z_{14}.L \| \| Z_{34}.L \| \| Z_{45}.L$	$C_4 + Z_{13}.C + Z_{34}.C + Z_{45}.C$	13.8477
T5	$Z_{45}.R$	$Z_{45}.L$	$C_5 + Z_{45}.C$	24.4317

Table 3.7: Analytical estimation of the peak voltages compared with simulation results for transients at each terminal of the network

Transient location	P_{load} [MW]	V_{dc}[kV] estimated	V_{dc}[kV] simulation	Error [%]
T1	900	373.8714	373.5199	0.0941
T2	800	370.7451	370.2969	0.1210
T3	1000	366.1205	365.8876	0.0637
T4	750	372.0879	372.0797	0.0022
T5	1200	303.3534	304.2558	0.2966

In order to validate this approach we simulated the network in Matlab/Simulink; starting with the network in zero-power flow state (i.e., all the voltages equal to 400 kV), we sequentially triggered at each terminal a sudden load connection equal to the nominal power rating of the converter. Then, we measured the lowest value reached by the voltage at the terminal where the connection was performed. This data is compared in Table 3.7 with the values obtained analytically by applying (3.28) on the Z_{pk} values presented earlier in Table 3.6.

As can be seen in Table 3.6, the differences between the values obtained by simulation and the values obtained with the proposed method are smaller than 0.3%, therefore, we can consider the method to be quite accurate despite the several approximations.

Having now an analytical relationship between V_{pk} and C for each terminal of the network, we can once again plot the two together, as seen in Fig 3.19. From these plots we can then select the size of the capacitor to be connected at each terminal in order to ensure that a certain voltage limit is satisfied during transients. For example, in order to ensure that all the transients remain inside the safety band, we selected the values displayed in Table 3.8 for $C_1..C_5$. Slightly larger values were selected in order to account for the approximations considered when developing the method. For comparison purposes we added also the time constant of these capacitors.

Table 3.8: Capacitors connected at the output of the VSCs - taking into account transients

Terminal No.	T1	T2	T3	T4	T5
C[mF]	0.5	0.5	0.75	0.5	5.0
C[ms]	44.44	50	60	53.33	333.33

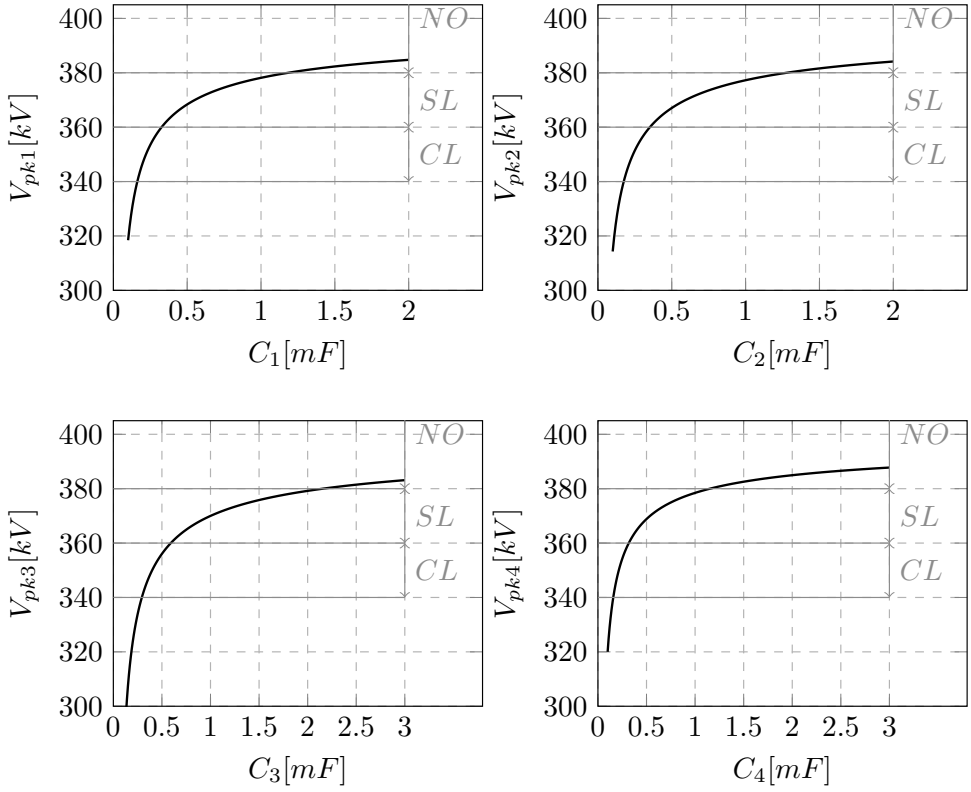

Fig. 3.19: Peak voltage at T1..T4 for different values of $C_{1..4}$.

Comparing the values of Table 3.8 with the initial capacitor values, we can see that C_1,C_2, and C_4 were oversized in the initial design, while C_5 was extremely undersized. This leads us to the conclusion that the size of the output capacitor is not only related to the power rating of the converter, but also to its position in the network. We can see the extremely large difference between C_3 and C_5 even though the power ratings of the two converters is almost equal. This is due to the fact that

the converter at T3 is strongly connected to the network by three cables, each of them ending at a terminal where the voltage is regulated. The converter at T5 on the other hand has an isolated position and its power rating is much higher than the neighboring terminal. Therefore, it requires more capacitance in order to *gain some time* until the perturbation propagates to the other terminals of the network and they start to participate in the voltage regulation.

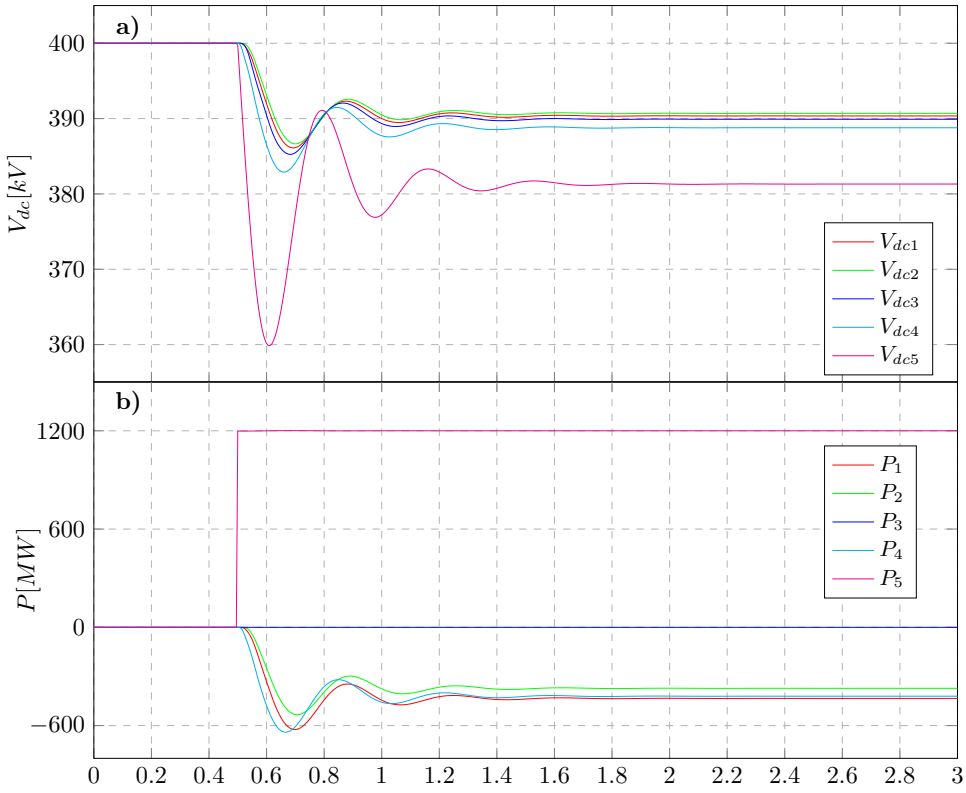

Fig. 3.20: 1200 MW step in the load power at T5. Evolution of the a) nodal voltages and b) power injections during transients.

In order to see the improvements in the dynamics of the system, we simulated once again the scenario shown previously in Fig. 3.16, i.e., all the network busses are initially at the nominal voltage and after 0.5 seconds a step of 1200 MW is applied to T5.

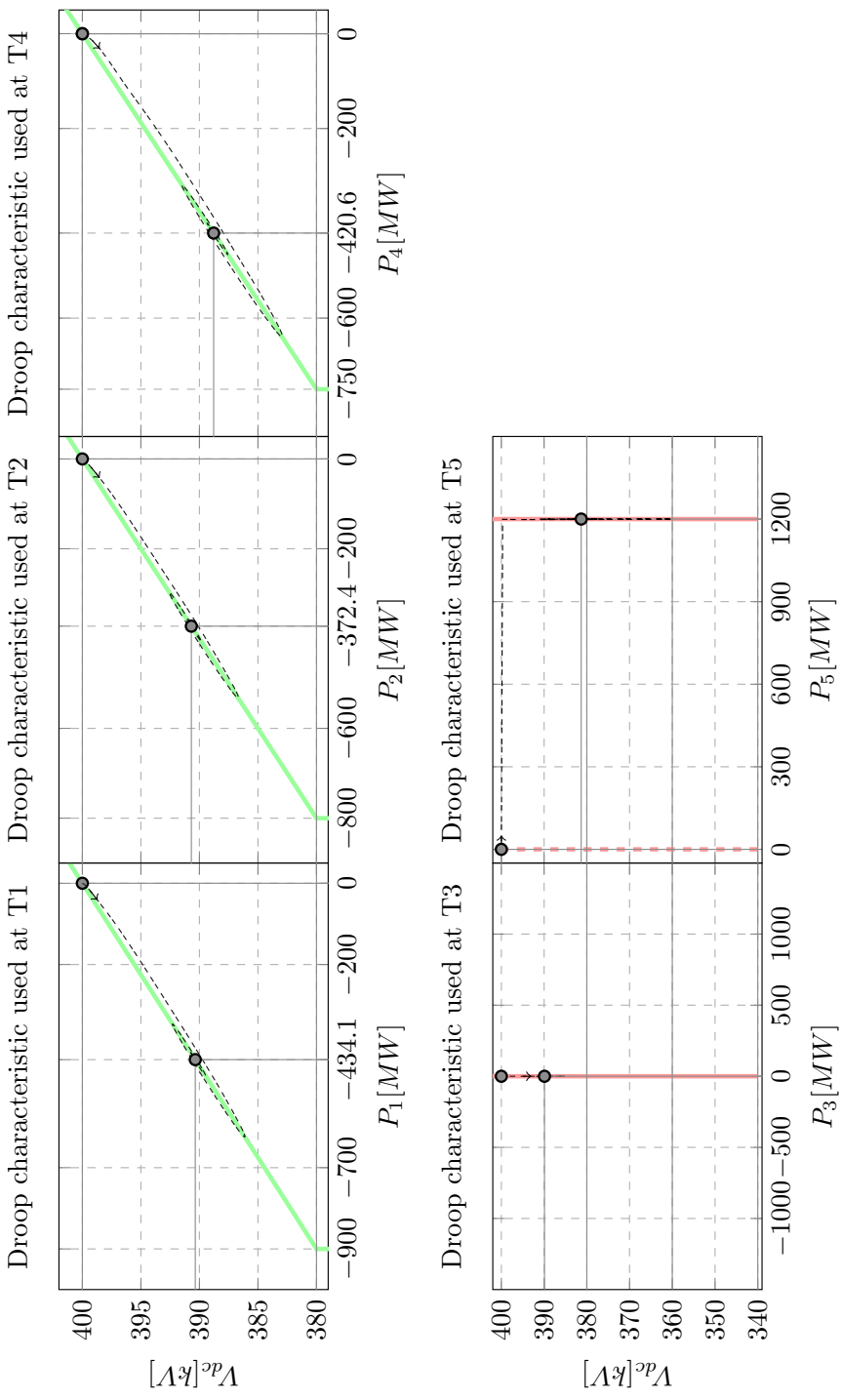

Fig. 3.21: 1200 MW step in the load power at T5. Evolution of the droop operating points.

The evolution of the network voltages and the power injection at each terminal is shown in Fig. 3.20. As can be seen in the figure, the transient response of the voltage at T5 has greatly improved and the first overshoot remains inside the SL operating band.

The improvements in the system behavior are also obvious if we look at the evolution of the operating points of the converters in the droop plane, as seen in Fig. 3.21. None of the converters reaches saturation and the trajectory followed for reaching the new operating point is less oscillatory.

3.6 Droop control with dynamic damping

We have shown in the previous sections that the size of the capacitors has a very strong impact on the dynamic response of the system. Increasing the value of the output capacitor is the only way to significantly reduce the first overshoot that occurs during the sudden connections or disconnections. A larger capacitor also provides better voltage damping, but not only a large capacitor has this effect. As was mentioned earlier in Section 3.3, the value of the droop resistance has also a considerable effect on the attenuation of voltage oscillations. A larger droop resistance will damp the oscillations faster, but it will also impose a larger steady-state voltage deviation. On the other hand, a smaller droop resistance will provide less damping, but it has the advantage of reduced steady-state voltage deviations.

We will analyze next how this aspect can be used in order to create a new droop controller that provides better damping during transients without affecting the steady state behavior.

3.6.1 Proposed droop control with dynamic damping

Let us consider again the two-terminals system shown in Fig. 3.6. We know from the previous sections that the frequency of the oscillations in V_{dc2} can be accounted almost entirely to the interaction between the parasitic inductance of the cable and the output VSC capacitor, given that the speed of the current loop controller at T1 is fast enough.

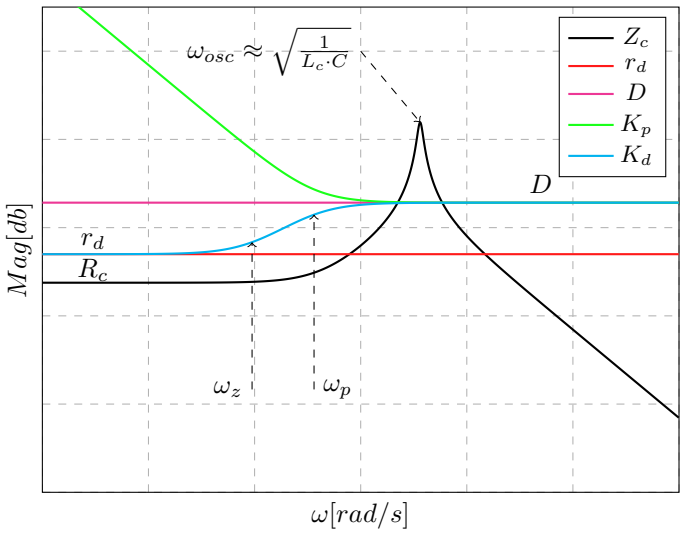

Fig. 3.22: Design of the droop control with damping.

Also, we have seen in Fig. 3.8 the impact of the droop resistance r_d on the time domain evolution of V_{dc2}. The same conclusions can be reached by looking at the frequency dependence of the equivalent impedance Z_c seen from T2.

$$Z_c = C||(R_c + s \cdot L_c) \tag{3.30}$$

First, we will consider Z_c for the case when V_{dc1} is constant, as shown in (3.30). We expect the steady-state gain to be influenced only by the cable resistance R_c, but as frequency increases the parasitic inductance of the cable will start to resonate with the capacitor at the output of the converter, creating a peak in magnitude at ω_{osc}, as defined in (3.31). The value of the cable resistance does not influence too much the resonating frequency, therefore (3.31) can be safely approximated by (3.32). A typical Z_c, plotted in the frequency domain, can be seen in Fig. 3.22.

$$\omega_{osc} = \frac{-R_c \cdot C + \sqrt{(R_c \cdot C)^2 + 4 \cdot L_c \cdot C}}{2 \cdot L_c \cdot C} \tag{3.31}$$

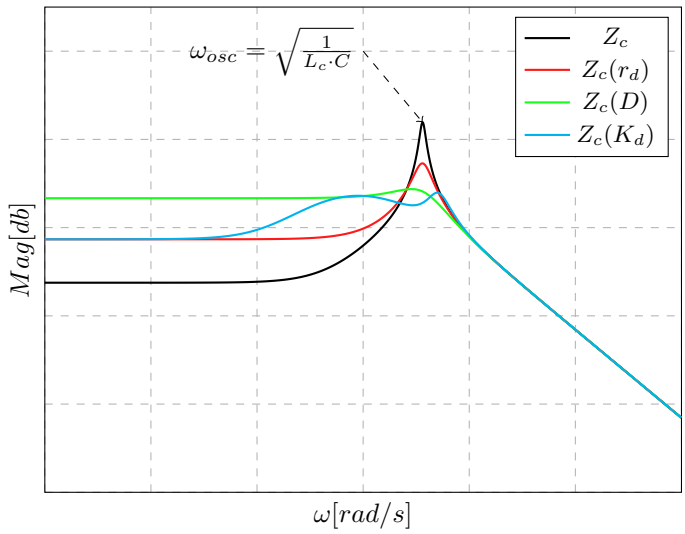

Fig. 3.23: Impact of the different droop controllers on Z_c.

$$\omega_{osc} \approx \frac{1}{\sqrt{L_c \cdot C}} \tag{3.32}$$

If V_{dc1} is not constant, but rather controlled by a droop controller, the virtual resistance r_d can be considered as connected in series with R_c and it has a direct impact on both the steady state gain of Z_c, and the resonance peak. The new value of Z_c is obtained as seen in (3.33).

$$Z_c = C||(R_c + r_d + s \cdot L_c) \tag{3.33}$$

Fig. 3.23 shows how Z_c changes for two distinct values of droop resistance, i.e., r_d and D (with $D > r_d$). It can be observed that, the larger the droop resistance, the larger the steady state gain of Z_c will be. This is the same conclusion from Fig. 3.8: the larger the droop resistance, the larger the steady state voltage deviation is. However, at the same time, the resonance peak reduces considerably as the droop resistance increases. Once again this reflects the increase in the damping of the system observed in Fig. 3.8.

We can see that using a small droop resistance or a larger one comes with both

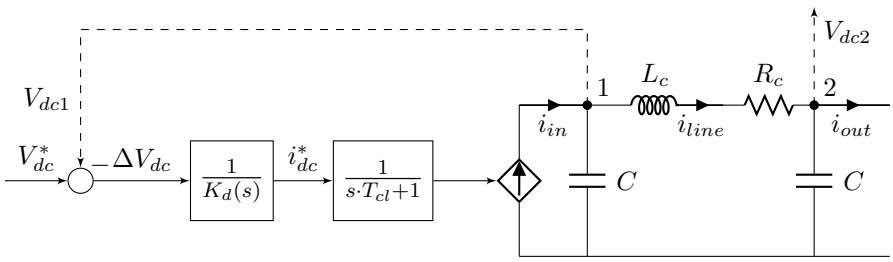

Fig. 3.24: Block diagram of DC-bus voltage controlled by dynamic droop.

positive and negative aspects. Therefore, an ideal controller should combine the steady state gain of a small droop resistance with the damping provided by a large droop resistance. Of course such a controller cannot be obtained, or better said, it cannot be obtained at each frequency. What can be done is to combine the advantages of the two into a frequency dependent droop characteristic that has a small gain at steady state and a larger gain at the frequencies where oscillations are expected.

A constant droop resistance, r_d, will offer the same amount of damping over the entire frequency range, as seen in Fig. 3.22. However, a dynamic droop resistance K_d, as defined in (3.34), will have at steady state a gain equal to r_d, but it will provide a larger damping at the resonating frequency. In order to see how the gain of the controller changes with respect to Z_c, the frequency characteristic of K_d is plotted together with r_d and D in Fig. 3.22 .

$$K_d(s) = r_d \frac{1 + \frac{s}{\omega_z}}{1 + \frac{s}{\omega_p}} \tag{3.34}$$

To analyze how these changes will influence the time response of the system, the simple proportional droop control is replaced by K_d, as shown in Fig 3.24. Maintaining the same format from the previous sections, we show in Fig. 3.25 the evolution of the injected current at T1 together with the voltage evolution at the two terminals. The dotted lines – displayed for comparison – are the response of the system by using the classic droop controller, previously shown in Fig. 3.7 of Section 3.3. The solid lines are the responses obtained by using K_d.

Several aspects should be pointed out. Firstly, K_d can be seen as a damper on

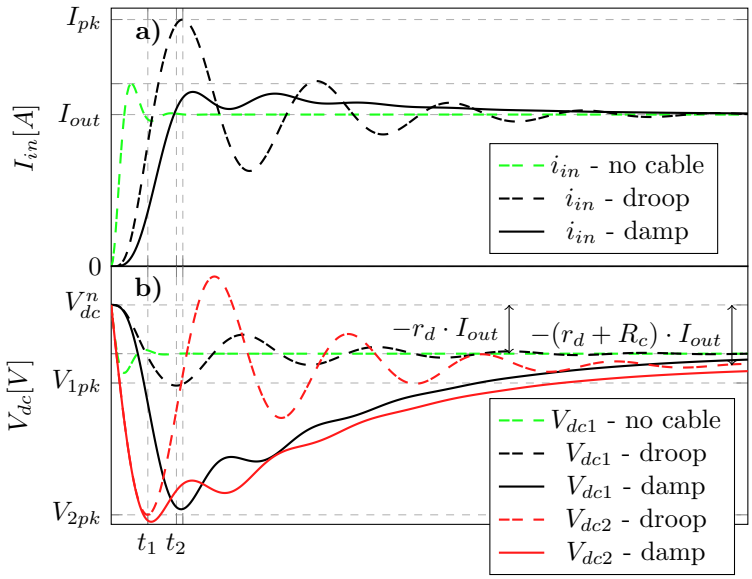

Fig. 3.25: Effect of the damping controller on the a) current injected by the VSC and b) dc-voltage at the two terminals.

the current dynamics; the current response to high frequency perturbations is slowed down; in this way the peak current is considerably reduced, as can be observed in Fig. 3.25a.

Because the current response is slower, V_{dc1} presents a much larger peak compared with the previous case (see the two black lines in Fig. 3.25b), but V_{dc2} only presents a slightly larger overshoot. In terms of damping, it can be clearly noted that the oscillations are considerably attenuated by using K_d and the two voltages follow a smooth trajectory towards the new steady state values.

To summarize, the advantage of using K_d, when compared with r_d, is that it considerably reduces the current overshoot and the oscillations in the voltage at the expense of a larger voltage sag in V_{dc1}.

We have showed the transfer function of K_d, but we have not yet discussed how to size its coefficients. In order to tune K_d, we have to select ω_z and ω_p, as described

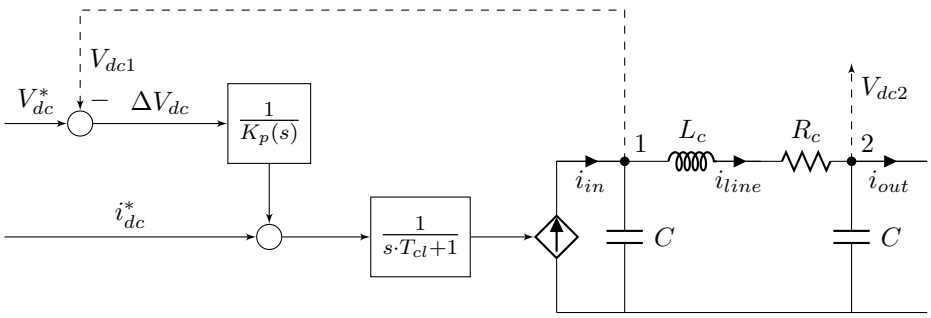

Fig. 3.26: Block diagram of constant current element with added oscillation damping controller.

in (3.35).

$$\begin{aligned} \omega_p &= \frac{\omega_{osc}}{10} \\ \omega_z &= \frac{r_d}{D}\omega_p \end{aligned} \tag{3.35}$$

We propose selecting the frequency of the pole, i.e., ω_p, so that the gain of K_d flattens out one decade before the oscillation frequency. The frequency of the zero, i.e., ω_z, is chosen based on the value of the steady-state droop resistance r_d and the value of the damping resistance D. Choosing the frequency for the pole and zero in this fashion, we ensure that at the resonating frequency the gain of K_d will be equal to D.

It can be seen that there is a trade-off between D and ω_z; this can be interpreted as a trade-off between the damping of V_{dc2} and the increase in the overshoot of V_{dc1}. A very large D will provide very good damping, but it will considerably reduce ω_z and, consequently, will slow the current dynamics even further, resulting in a large voltage drop at T1. On the other hand, a small damping factor will attenuate very little the oscillations. Therefore, in order to reach a good trade-off between damping performance and voltage drop, we propose choosing D as shown in (3.36).

$$D = \sqrt{\frac{L_c}{C}} \tag{3.36}$$

The proposed controller offers additional damping for the elements of the net-

work that are operated in droop mode. However, a similar damping controller can be imagined for the nodes that are in constant power control, if these nodes allow a slightly deviation from their power reference during transients. This type of behavior could be implemented in the converters connected to energy sources that have some inertial element, such sources could be wind turbines, strong ac-grids, and even PV+ES power plants emulating virtual inertia.

Having the voltage error as input, a damping element K_p, defined in (3.37), can be added to the control structure of the constant power converters as seen in Fig. 3.26. The only difference to K_d is that, at steady-state, K_p has infinite gain.

An important aspect that has to be taken into consideration when choosing ω_p and D for the constant power converters is the amount of inertia of the primary source of energy to which the converter is connected. A too small damping factor D could result in sudden large deviations from the initial power reference during transients; deviation that cannot be supported by elements with small inertia.

$$K_p(s) = \frac{1 + \frac{s}{\omega_p}}{\frac{s \cdot D}{\omega_p}} \tag{3.37}$$

3.6.2 Study case

In order to test the proposed control strategy we considered once again the five-terminal network of Fig. 3.14. Maintaining the previously calculated values for the network parameters, we changed the proportional droop controller by a droop controller with dynamic damping K_d and we added a damping element K_p to the constant power controllers.

In order to design these controllers, first, we had to identify the frequency of the oscillations at each terminal. Taking the parameters for R_c, L_c, and C_{tot} from Table 3.6, we calculated for each terminal ω_{osc} and D as seen in Table 3.9.

Looking at the data presented in Table 3.9, we can see a large difference in the frequency of the voltage oscillations generated by load changes at T5, when compared to the other terminals. This is an expected behavior, as the large capacitance at the output of T5 will push the resonating peak towards lower frequencies; in our

Table 3.9: ω_{osc} and D for the five terminals of the network

Terminal No.	T1	T2	T3	T4	T5
ω_{osc}[rad/sec]	149.72	130.30	101.80	125.22	19.41
D	12.40	14.67	12.28	14.49	10.25

Table 3.10: Initial steady state of the network

Terminal No.	T1	T2	T3	T4	T5
P[MW]	502.5873	445.6743	-900.00	445.0593	-500.00
V_{dc}[kV]	411.1685	411.0876	412.5737	411.8682	414.7315

case ≈3Hz, which is consistent with the results of Fig. 3.20.

In order to design a unified controller for all the elements of the network, we selected ω_{osc} as the average of the values showed in Table 3.9, i.e., 105.29 rad/sec. The same was done when choosing D. Better results might be obtained by choosing a different ω_{osc} and D for each element of the network depending on its neighboring elements, but this aspect was not approached in this work.

Until now we have analyzed only the behavior of the system with respect to perturbations at T5. Of course, we know from Table 3.7 and from the way we dimensioned the capacitors in the previous section, that all the terminals will be safe from voltage overshoots during transients, but it is interesting to also look at the dynamic evolution of the system when one of the terminals connected to a smaller capacitor is suddenly disconnected, because, as we can see from Table 3.9, higher frequency oscillations should be expected.

Let us consider the following scenario: the VSC converters at T3 and T5 are injecting power into the network and the other three converters regulate the voltage according to their droop characteristics. The initial steady state operating point reached by the network is shown in Table 3.10. Since the constant power elements are injecting power into the network and at the moment, there is no secondary control to correct the voltage, all the voltages will be above the nominal value.

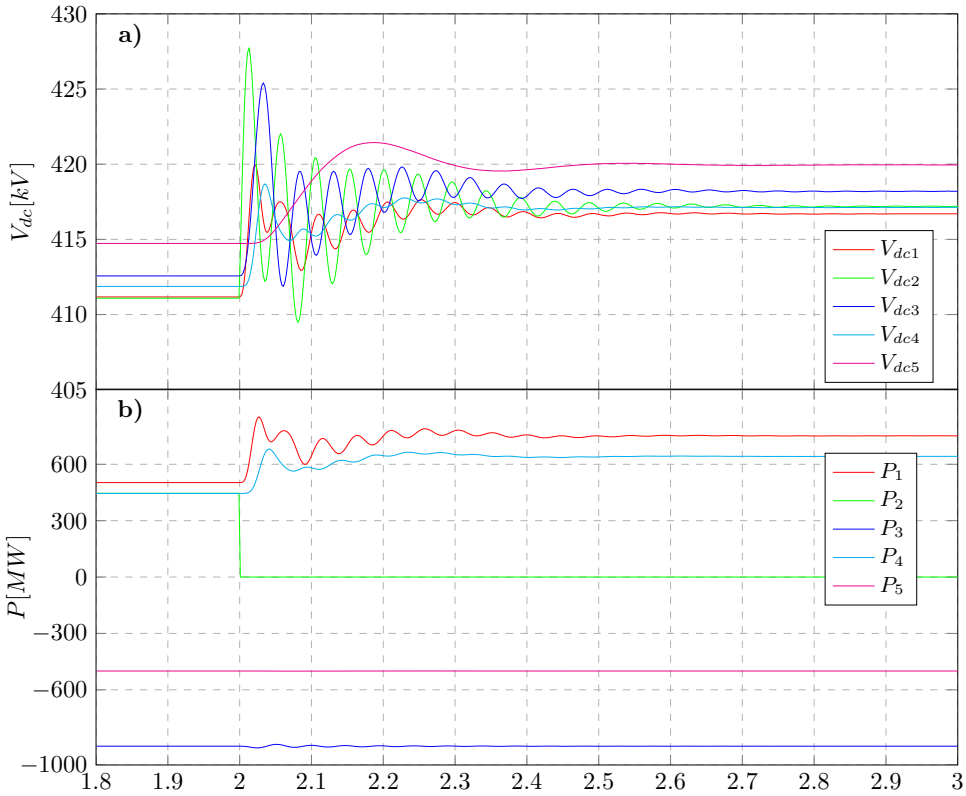

Fig. 3.27: 445 MW trip in the load power at T2. Network controlled by r_d. Evolution of the a) nodal voltages and b) power injections during transients.

First, lets see the response of the network when using the standard droop control. Starting from the steady state of Table 3.10, after 2 seconds, we trip the load at T2. According to Table 3.9, for trips at T2, we should expect oscillations at 130.30 rad/sec, i.e., 20.74 Hz; which is consistent with the results shown in Fig. 3.27.

We can see in Fig. 3.27 that the first overshoot in V_{dc2} is at around 427 kV and that the oscillations from T2 propagate also in the rest of the network, taking around 0.8 seconds to attenuate completely.

The same scenario as before is simulated again, only now the controllers at each terminal have been complemented with damping elements. Therefore, for the droop terminals, i.e., T1, T2, and T4, K_d controllers have been designed as showed in the previous subsection; meanwhile, a K_p element has been added to the constant power

terminals, i.e., T3 and T5. The results of the simulation are shown in Fig. 3.28.

We can see that the first peak of the transient is almost unaffected, but the damping of the oscillations is significantly improved. The oscillations die out in less than 0.2 seconds. What is also interesting to note is the behavior of the constant power elements. While in Fig. 3.27 the power at T3 and T5 was maintained constant during the transient, now it suffers a small deviation in order to contribute in the damping of the oscillations. However, once the transient has finished, the power reference returns to its initial value.

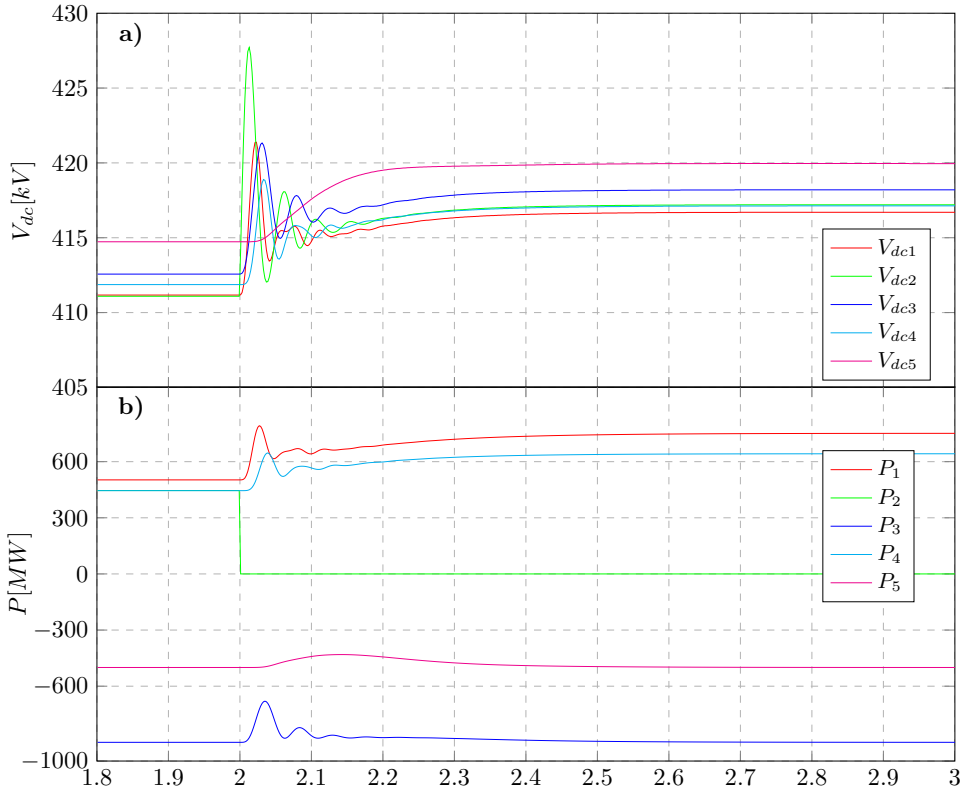

Fig. 3.28: 445 MW trip in the load power at T2. Network controlled by K_d. Evolution of the a) nodal voltages and b) power injections during transients.

3.7 Conclusions

While the previous chapter was focused on providing a clear idea about how the different droop characteristics interact with each other, we dedicated this chapter to analyze the dynamic behavior of, firstly, one droop controlled converter, and later, the interaction between two converters, and the importance of the connecting cable.

Based on this analysis, we were able to properly size the output capacitors together with the operating bands of the primary control in order to avoid overvoltages in case of sudden load variations.

We have also showed that the size of the capacitor is not related only with the power rating of the converter to which is connected, but it is influenced by the topology of the network. In our analogy with the ac systems from the previous chapter, we presented the capacitor as the inertial element of the system. This aspect was also visible here; the isolated terminals of the network – where the voltage control was rather poor – required significantly larger capacitance at their outputs, when compared with terminals in the same power ratings connected in the *strong* part of the network.

After properly sizing the network parameters we proposed a frequency dependent droop characteristic that offers improved voltage damping, when compared with the classic droop control.

The presented ideas were validated through simulation on a five terminal HVDC network. In the steady state analysis of the interaction between the droop values and the network cables, we acknowledged the need of a secondary control layer, as for a fully loaded network the voltages deviate considerably from the nominal value due to the current flowing through the resistive cables. This aspect is addressed in the next chapter, where we will show how the secondary control should guide the primary control in order to always maintain the voltage in the NO band for normal load-flow scenarios.

Chapter 4

Secondary Control of MTDC Networks

Since the control strategy that we propose for the MTDC network is hierarchical, we will focus this chapter on the operation of the secondary control layer and how it interacts with the primary control. The proposed secondary control is centralized and regulates the operating point of the network so that optimal power flow (OPF) is achieved. We will try to elaborate, both analytically and through simulations, on the dynamic interactions between the primary and secondary control layers. This also includes how local primary controllers have to be driven by the centralized controller in order to ensure a smooth transition to the optimal operating point, taking into account communication delays and the dynamics of the primary control layer.

4.1 Secondary control in ac networks

Similar to Chapter 2, we are going to start the discussion on secondary control by taking a brief look at how this control strategy is implemented in ac-networks and what is its purpose.

We have shown in Chapter 2 that, if primary control is implemented by a droop characteristic, as the one shown in Fig. 4.1, any deviation in frequency Δf will generate a deviation ΔP_m^{set} in the power injected by the generator. However, the intrinsic behavior of such a controller is purely proportional; once the steady state operating point (f_1, P_1) has been reached, the system will not be able to return to the nominal frequency f_0 on its own. The frequency can be returned to its nominal

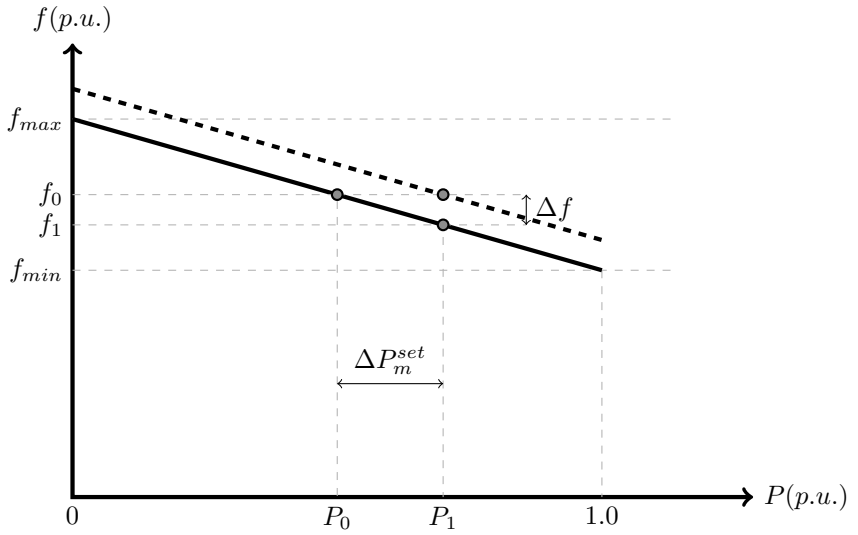

Fig. 4.1: Equilibrium points for various P-f droop characteristic used in the primary control of power plants.

value only by shifting the droop characteristic (considering the fact that the slope of the characteristic should be maintained constant) to the position of the dotted line in Fig. 4.1. In this way, the generated power is maintained at the same value P_1, but now this power injection corresponds to the nominal frequency.

Therefore, the main purpose of the secondary control in ac-networks is to recover the frequency back to its nominal value by controlling the generation characteristics, once a steady state operating point has been reached due to the action of the primary control. In order to avoid any conflict between the primary and secondary control, the time constants of these two controllers, or better said, the time of reaction for these control strategies, is well separated. According to ENTSO-E[51], the primary control has to remain active from a few seconds to maximum 15 minutes. After this time has passed, the primary control has to be replaced by the secondary reserves.

According to [50], for isolated ac systems, the functional block of the secondary control that corrects the frequency deviations can be implemented locally using a decentralized approach; this is done by complementing the turbine-governor sys-

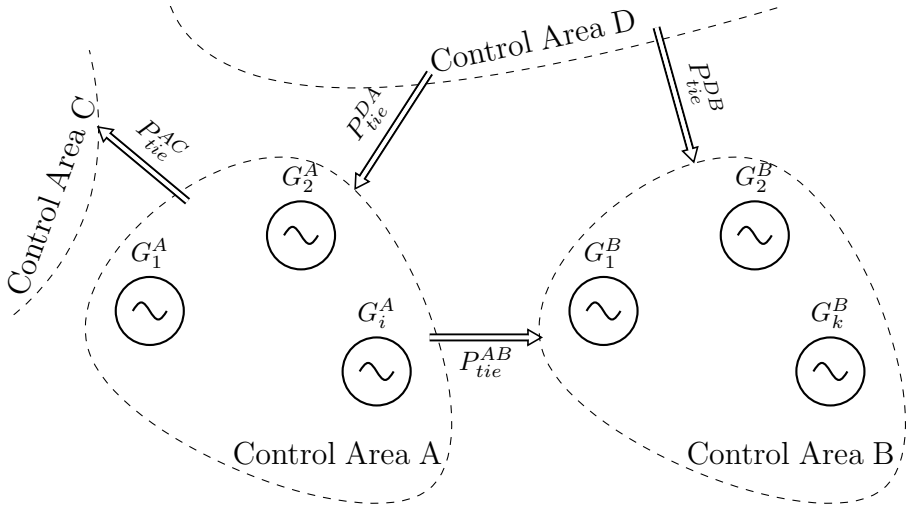

Fig. 4.2: Multi-area control of ac-networks.

tem, presented in Chapter 2, with an additional integrator term that has as input the frequency error. However, for interconnected systems, such as the one displayed in Fig. 4.2, besides correcting the frequency deviations, the secondary control has to maintain the tie-lines power flow at the scheduled value, therefore, it cannot be implemented as a decentralized controller.

In the case of a multi-area system, the secondary control is implemented for each area, as shown in Fig. 4.3. It can be seen that now there are two signals that go to the integral controller; the first one comes from the frequency error and the other one from the error in the tie-line power. This mechanism enables each of the secondary controller to establish if the deviation in the system frequency is caused by an unbalance produced in its control area. If the λ term, called *frequency bias factor* in the literature, is dimensioned correctly, then the ACE signal, i.e., the *area control error*, will be non-zero only for the area that is causing the unbalance. Then, according to Fig. 4.3, the secondary control in charge of that area will start to send new power references for the primary controllers in order to bring the frequency back to its nominal value and to return the tie-line power to its previous reference, if enough generation power is available in the affected area. The participation of each generator in this process can be controlled by selecting different scaling weights α.

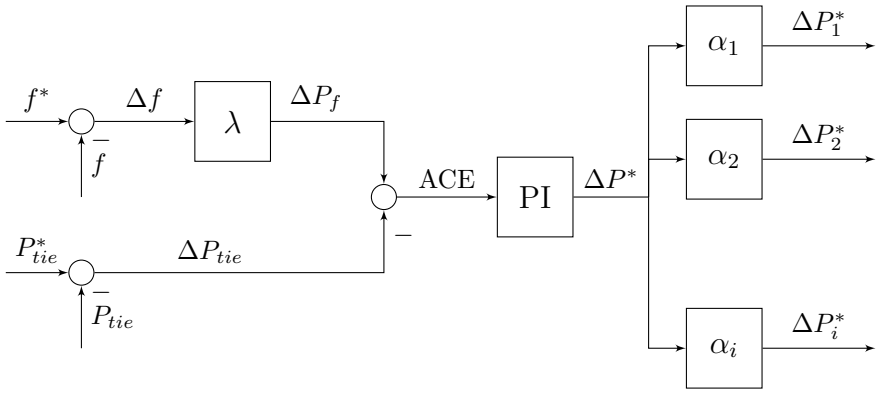

Fig. 4.3: Area control of ac-networks.

Probably the most critical point of this control strategy is determining the correct value for λ. Theoretically, this value should be equal to the gain of the aggregated droop characteristic, expressed in MW/Hz, of all the generators in the controlled area that participate in the primary control. Obtaining the exact value of λ in real time is a difficult task that is still the subject of on-going research in the field. The difficulty lies in the fact that the stiffness of the network depends on its structure and on the control strategy of the connected generators. For this reason, according to [50], in the European power system, the frequency bias factor λ is in practice established yearly, based on the share of energy production of one area with respect to the total energy production.

4.2 Secondary control in dc networks

We have seen in the previous chapters that droop control, regardless if applied to primary control of ac or dc networks, will present steady state deviations from the nominal operating conditions. Extrapolating the concept of secondary control from ac-networks, secondary control in dc-networks should restore the voltage of the network after the actions of the primary control have reached steady state. However, the same issues as before arise: the structure of Fig. 4.3 cannot be readily used for dc networks, because, as was discussed in the earlier chapters, dc voltage is not

a unique value like frequency and it varies with the power flow. Therefore, the secondary control will have to regulate the voltage at each bus, but the reference value that should be reached has to be calculated every time, depending on the state of the network.

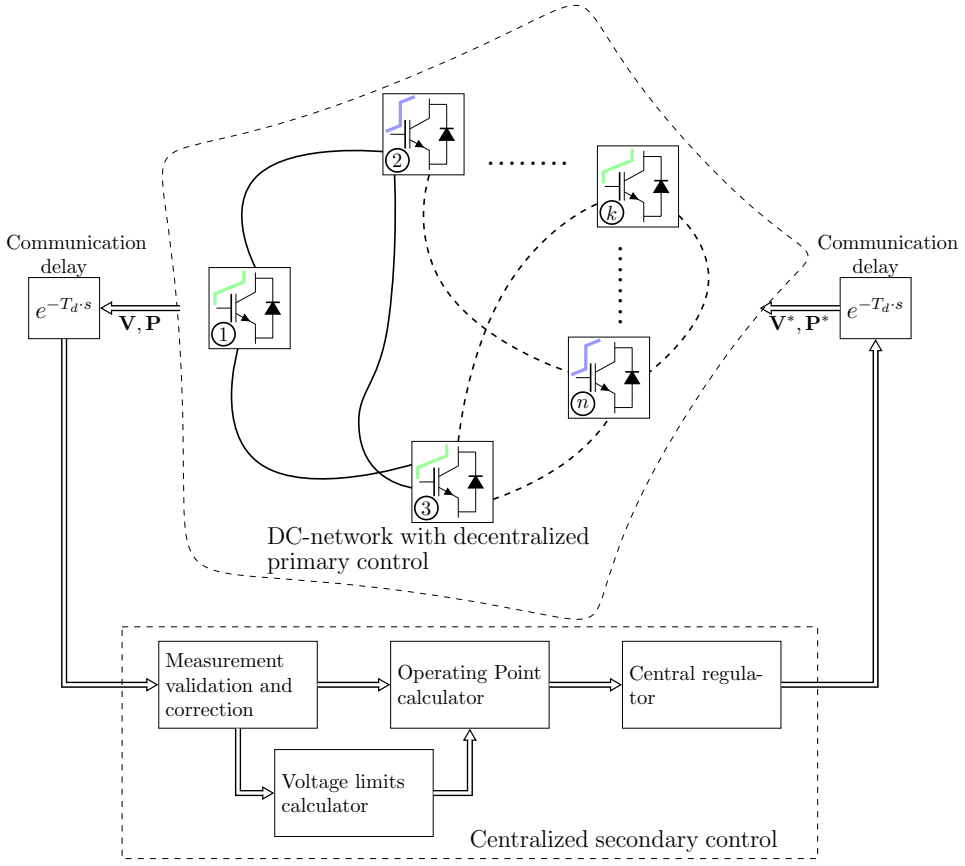

Fig. 4.4: Block diagram of hierarchical control of meshed MTDC grids.

Fig. 4.4 shows the conceptual diagram of the hierarchical control structure that we propose. The primary control is decentralized and runs locally in each converter, as presented in the previous chapters. When a change in load or generation occurs in the network, the droop-based primary control will react accordingly to the deviation in the voltage. The operating point (OP), at which the network arrives

after the action of the primary, is influenced in equal part by all the droop gains and the network topology. Therefore, given the influence of the network-structure, the operating point of the network can only be evaluated from a central controller.

The secondary control, marked by a dashed box in Fig. 4.4, is centralized and relies on low-bandwidth communication. Its objective is to periodically re-evaluate the operating point of the network and, if a better option is possible, it computes new references for the primary in order to bring the network to the new operating point.

Four imminent requirements arise when analyzing the design and implementation of the secondary control for MTDC, as highlighted by the four blocks in Fig. 4.4.

Firstly, the measurements received from the primary control have to be validated and corrected. Even though it does not affect the dynamic response of the system, this is a very important step for the practical implementation of this control strategy. However, state estimators and bad-data identification algorithms are complex topics that require a separate approach and are considered to be outside the topic of this thesis. As our analysis is focused more on the system dynamics, we do not consider measurement uncertainty, but dealing with this aspect is a crucial aspect for a practical implementation of the system.

The second functional block of the secondary control that we identified is the *Voltage limits calculator.* The purpose of this process is to establish how much the voltage can be safely increased or decreased in the following stage by the operating point calculator. We know from the previous chapter that the operating limits of the voltage at each terminal are dependent on the structure of the network and on the power flow. In order to obtain these limits, the *Voltage limits calculator* uses real-time measurements of the bus-voltages and power injections, together with apriori information about the network, such as the conductance matrix and the dynamics of each unit connected to the network.

The next step of the secondary control is the *Operating Point calculator*. This block computes the new OP of the network using a pre-established strategy. In our implementation we propose an operating point calculator based on an optimal

power flow (OPF) algorithm that will try to always bring the network to the minimal transmission losses OP. Other strategies, based on mixed ac-dc power flow, with focus on security and robustness, or following a pre-established participation factor, can be imagined and implemented in this block. Algorithms based on OPF for calculating the OP of the network will tend to increase the voltage of the network. Therefore, knowing the limits up to which the voltage can be increased is essential, hence the need for the *Voltage limits calculator* block.

Finally, once a new steady-state OP has been calculated, new references have to be sent to the primary control. The *Central regulator* has to take into account the dynamics of the dc-network and it has to change the reference without perturbing too much the system. Moreover, there might be cases when the actual OP of the network is far away from the optimum OP. Making the transition in one step will create undesirable perturbations in the network. Therefore, the central regulator has to smoothly drive the system from its current OP to the optimum OP.

In the following subsections we are going to take three out of these four functional blocks – *Measurement validation and correction* is left for future investigation – and explain their implementation.

4.2.1 Voltage limits calculator

The need of a voltage limit calculator block arose from the fact that any attempt to minimize the transmission losses in a dc-grid will necessarily raise the nodal voltages of the grid. At least one of the voltages of the busses that inject power will reach its upper limit when the optimum operating point is achieved. The remaining voltages will be determined by the drops arising from the need to accommodate power flows through the branch resistances.

Works as [45, 60, 76] allow a 10% voltage deviation for power transmission and, therefore, every time the losses of the network are optimized, at least one of the generating busses has the voltage amplitude bounded to 1.1 p.u. Using this strategy, the voltages at the load busses – which we have seen in the previous chapter that can experience large overshoots in case of trips – are unknown, as they are determined by the current flowing through the resistive lines. This approach raises questions

related to safety, as it does not allow any headroom for possible transients.

In the proposed method we consider the limiting factor to be the load busses. Given a certain load at a bus, the voltage at that bus can only be increased up to a certain value, if we want that the transient overshoot caused by an eventual load trip to be contained in the safety operating band.

In Section 3.5.3 of the previous chapter we presented a method for sizing the output capacitors of the VSC by analyzing the voltage overshoot at each terminal and the so-called *peak impedance* Z_{pk}, seen from the terminals of each VSC. Z_{pk} offered a direct link between the current of the VSC and the peak overshoot that it will produce in case of a trip. The same concepts can be used for calculating the maximum voltage allowed at a bus, given a certain load requirement at that particular bus.

As it was shown in Section 3.5.3, in order to calculate Z_{pk}, the exact parameters of the connecting cables are required as well as the structure of the network. The latter can be established in real-time by analyzing the state of the protective relays. However, the cable parameters might vary, for example due to heating effects; according to [78] the resistance of a copper cable can increase with 20-25% for a temperature increase from 20º to 85ºC. Therefore, a real-time estimation procedure should be employed in practical implementations in order to properly assess the cable parameters. However, this aspect might prove to be not so difficult, since it is reasonable to assume that in future MTDC systems, being so expensive and complex, temperature sensors will be available throughout the network, providing the cable temperatures (and hence resistances/inductances) in real time.

4.2.2 Operating point calculator based on OPF

The operating point calculator is the functional block responsible for calculating the new OP at which the network should operate. Since this block takes into account all the network, the involved variables are the network's vectors and matrices introduced in the previous chapter, i.e., $\mathbf{P}$ and $\mathbf{V}$ (the measurement of power and voltage at every bus), the conductance matrix $\mathbf{G}$, $\mathbf{P}^*$ and $\mathbf{V}^*$(the new references for the primary control).

The strategy that we propose for this block is to calculate the new OP of the network so that the transmission losses are minimized; therefore, an optimal power flow (OPF) algorithm taking into account the grid losses is employed. This problem can be formulated as an optimization problem of a constrained quadratic function that depends only on the voltage vector $\mathbf{V}$, as shown in (4.1).

$$\min_{\mathbf{V}} f(\mathbf{V}) \text{ such that } \begin{cases} c(\mathbf{V}) & \leq 0 \\ c_{eq}(\mathbf{V}) & = 0 \\ lb & \leq \mathbf{V} \\ ub & \geq \mathbf{V} \end{cases} \tag{4.1}$$

The objective function $f(\mathbf{V})$ is considered to be the losses of the transmission grid, as expressed in (4.2). Here, V_i and V_j represent the voltage amplitude at node i and j, respectively, and g_{ij} is the equivalent conductance of the cable between the two nodes. The same relationship can be expressed in matrix format, as shown in (4.3).

$$f(\mathbf{V}) = P_{loss} = \sum g_{ij} \cdot (V_i - V_j)^2 \tag{4.2}$$

$$= \mathbf{V^T} \cdot \mathbf{G} \cdot \mathbf{V} \tag{4.3}$$

Setting the problem in this manner avoids the selection of a slack bus by distributing the system imbalance among droop controlled converters. The buses operating at constant power can be introduced as equality constraints, while the rest of the buses become slack buses and are introduced in the problem formulation as inequality constraints.

Once the objective function is set, the remaining terms of (4.1) are the constraints. The inequality constraints are given by the power rating of the converters that participate in the voltage control, i.e., in our case, the droop-controlled converters. These converters will have to change their power reference in order to bring the network to the new OP and we have to ensure that this reference will not exceed the maximum power of the converter P_{max}. For a converter i, considered to be droop-

controlled, the corresponding inequality constraint can be expressed as shown in (4.4), where the term $\text{row}_i\mathbf{G}$ stands for the *i-th* row of the conductance matrix .

Another aspect that imposes inequality constraints to the optimization problem is the current rating of the power lines. The constraint for the power line connecting node i to node j can also be expressed as a function of voltage, as shown in (4.5); here, I_{ijmax} is the maximum current that can flow through the line.

$$c_i(V_i) = V_i \cdot \text{row}_i\mathbf{G} \cdot \mathbf{V} - P^i_{max} \tag{4.4}$$

$$c_{ij}(\mathbf{V}) = g_{ij} \cdot \left|V_i - V_j\right| - I_{ijmax} \tag{4.5}$$

The equality constraints c_{eq} of the optimization problem are given by the converters operating in constant power mode. If the power that is subtracted from node i has to be equal to P^i_{load}, then the equality constraint for this node can be set as shown in (4.6), where the term $-V_i \cdot \text{row}_i\mathbf{G} \cdot \mathbf{V}$ represents the power injected into the node i from all the adjacent nodes. A similar constraint, but with opposite sign, can be introduced also for the converters operating as constant power generators. In this way, we can ensure that the obtained solution will satisfy the requirement of the constant-power buses.

$$c_{eq}(V_i) = -V_i \cdot \text{row}_i\mathbf{G} \cdot \mathbf{V} - P^i_{load} \tag{4.6}$$

The last two sets of constraints in (4.1), namely *ub* and *lb*, represent the upper bound and the lower bound of the solution domain. The solution of the optimization problem will have to be inside this domain. The more critical bound is *ub*, as the tendency of the algorithm will be to increase the voltage in order to minimize the losses. That is why, *ub* is computed apriori by the voltage limits calculator and not just set to the maximum allowed voltage.

In its original form, this problem does not satisfy the convexity definition. However, in [45], it is shown that the equality constraints can be safely treated as linear functions, therefore, the optimization problem can be treated as convex, given the convexity of the objective function and of its domain. Such an optimization prob-

lem can be readily set and solved using standard solvers from Matlab's Optimization Toolbox.

4.2.3 Central regulator

Looking at the structure of the primary control, one can see that there are two ways for the secondary control to regulate the voltage of the network. One is to directly change the voltage reference V_{dc}^* of the primary droop controller and the other one is to bypass the voltage control loop and provide an additional input to the internal current loop, similar to the structure used in ac-systems and as seen in Fig. 4.5. However, the most convenient way, from a feedback control point of view, is to handle V_{dc}^* and P^* simultaneously.

Handling V_{dc}^* and P^* together might seem counter-intuitive at a first glance, but let us consider first the case when P^* is used for controlling the voltage. Based on the voltage and power measurements from the grid, the secondary control layer calculates the value for P^* that will bring the voltage to the new required value and sends it to the primary. As soon as the primary control starts to regulate the current flowing in the dc-bus capacitor, the voltage will start to change and the droop control loop will try to oppose this change. Therefore, the value that the secondary has to compute for P^* will have to be larger than the actual value that will be injected by the converter in order to counter-balance the effect of the droop control loop. Similarly, if V_{dc}^* is used to control the voltage, the value of the reference computed at the secondary will have to be different than the actual values desired for the grid voltages in order to account for the effect of the droop resistance.

For the case when both reference signals are used, the secondary calculates the desired voltage profile $\mathbf{V}^*$, and, using (4.7), it also calculates the required power injection; here, $\otimes$ is used to denote entry-wise matrix multiplication, also known as the Hadamard product operator. Sending both these references to the primary control will cancel the corrective effect coming from the droop control loop. This behavior can be also seen as follows: the secondary control knows in advance what voltage each bus will reach, given a certain power injection profile. Therefore, it calculates in advance how each of the droop curves of the primary has to be offset

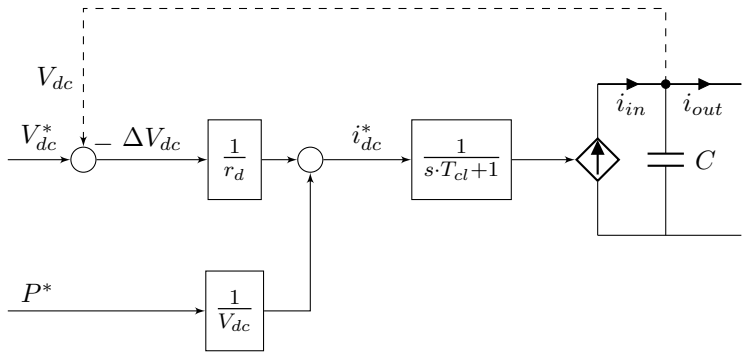

Fig. 4.5: Control structure of droop-based primary with secondary control inputs.

so that they are centered at that voltage, i.e., the zero-current operating point of the converter will be reached. In this way, ΔV_{dc} will be zero at steady state and there will be no power demand from the droop control loop.

$$\mathbf{P}^* = \mathbf{V}^* \otimes (\mathbf{G} \times \mathbf{V}^*) \tag{4.7}$$

The central regulator is the module of the secondary control that is in charge of sending new references to the primary control. It has as inputs the measurement of all the n voltages of the network, but usually only k of them correspond to busses that participate in primary control; $k < n$, if there are constant power busses in the network. Because a change in the power or the voltage at a terminal affects all the other voltages of the network, the design of the central regulator translates into a multi-input multi-output (MIMO) control problem of very large dimension for networks with many elements, as seen in Fig. 4.6. Here, $H_{V_i^* V_j}(s)$ is the equivalent transfer function from the change in reference V_i^* to the output voltage V_j and T_d is the communication delay between the primary and secondary control layer.

A full matrix controller could have the advantage of decoupling the signals, but it might prove incredibly difficult to design for large systems. Moreover, such a controller is not easily scalable as its off-diagonal elements would depend highly on the structure of the network reflected in $\mathbf{H}$. Taking this into consideration, we propose a diagonal controller where each element of $\mathbf{K}$ is a PI controller. This

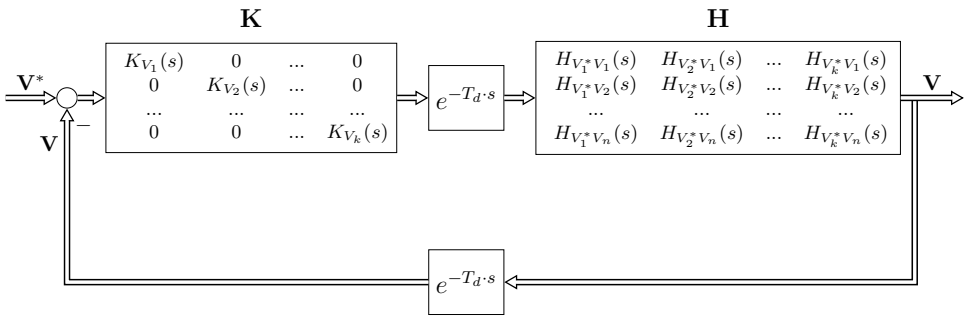

Fig. 4.6: Diagonal central regulator based on integral control.

approach is somehow similar to the central area regulator of the ac-grids, only now, due to the fact that the voltage is not a unique value as the frequency, we will have a PI controller at the secondary control for each unit controlled at the primary by the droop.

The order of the system is unmanageable analytically, but a loop-shaping approach can be used for tuning each controller that appears on the diagonal of **K**. Two aspects have to be taken into account when tuning these controllers, as we will show in the next section. Firstly, the time constant of the integrator has to be chosen slow enough so that it offers decoupling from the events that occur at the primary layer. For this, the controller needs a very small gain at all the resonating frequencies introduced by the cables and the primary control.

Secondly, a proportional term can be added in order to improve the phase margin of the system and, therefore, its stability. The gain margin of the open loop system has to be also monitored while adjusting the proportional gain, as a too high gain can significantly reduce this margin, making the system sensitive to any model uncertainties.

4.3 Study case

In order to validate the proposed approach, we designed a secondary control layer for the five terminal network analyzed previously in Section 3.5. The secondary control receives, at each sampling time T_s, a new set of measurements from the

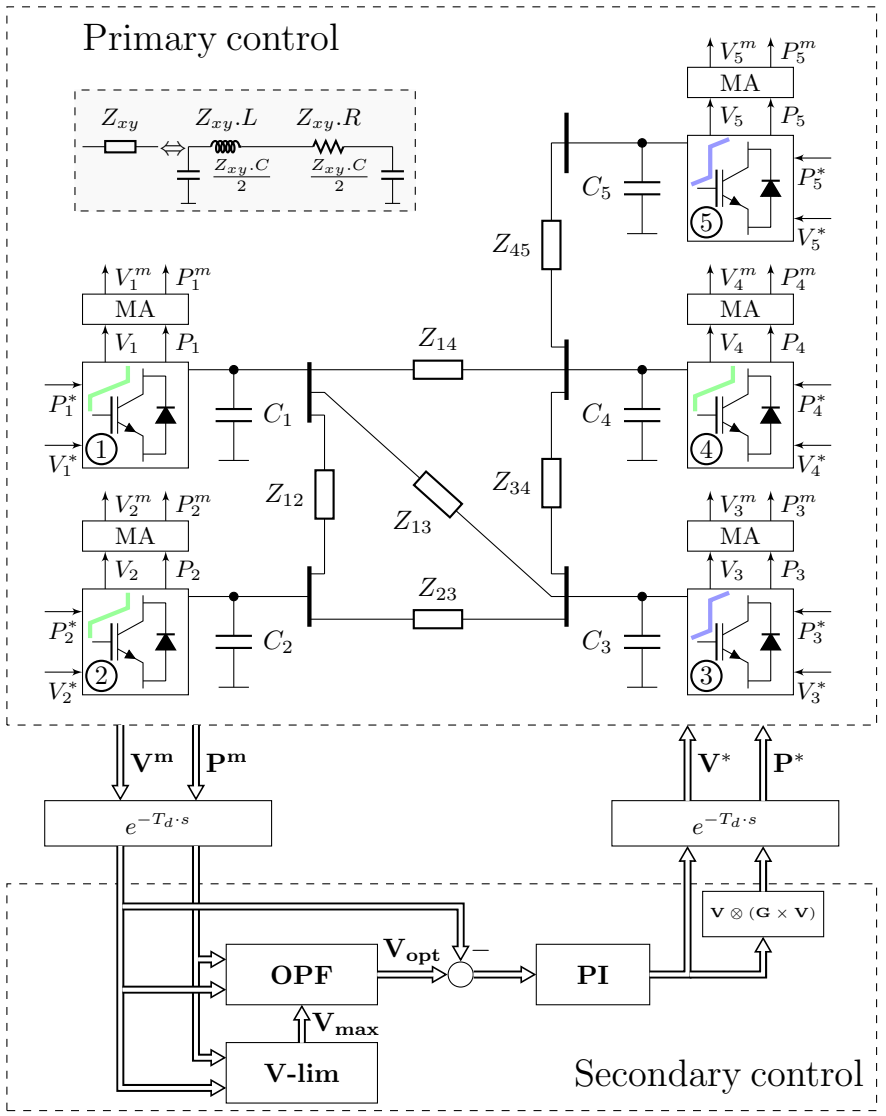

Fig. 4.7: Meshed MTDC network with droop-based primary control used in the simulation scenarios. Secondary control composed of operating point calculator based on OPF and integral control reference driver.

primary and it computes a new OP for the network. For our study case, we selected T_s equal to 0.5 seconds. This value was considered realistic given the fact that works on hierarchical wide-area control of power systems report measurement delays as low as 300ms [79]. Rather than operating with instantaneous measurement samples, a moving average (MA) of the measurements with a time window equal to T_s is computed at the primary control level, before being sent to the secondary, as shown in Fig. 4.7.

The communication delay T_d between the primary and the secondary was set to 300ms, following the values reported in [79].

The remaining parameters of the system, needed at the primary control level for characterizing the structure of the network and the rating of the converters were maintained the same as in the previous chapter, only now, each converter receives additional voltage and power references from the secondary control layer, as seen in Fig. 4.7.

4.3.1 Design of the central regulator

Similar to the study case presented in the previous chapter, in the system shown in Fig. 4.7, three terminals, i.e., T1, T2, and T4, participate in the control of the voltage, while T3 and T5 are operated at constant power. The first thing to do when designing the central regulator is to obtain the equivalent transfer function from the voltage reference V_i^*(which is sent to a converter by the secondary control) to the actual voltage obtained at the output of the converter V_i, i.e., the diagonal elements of **H** from Fig. 4.6. The non-diagonal elements are not important for our design, since the controller **K** is a diagonal controller.

Given the complexity of the system, these transfer functions cannot be easily obtained analytically; however, by making use of tools such as Simulink, one can linearize the system and obtain a good enough approximation. Following this exact procedure, we obtained the transfer function from $V_i^* \rightarrow V_i$ for T1, T2, and T4; the corresponding Bode plots for these transfer functions are illustrated in Fig. 4.8. As it can be seen from the figure, the three transfer functions present similar characteristics, with all the *dynamics* happening at frequencies larger than 10 rad/s.

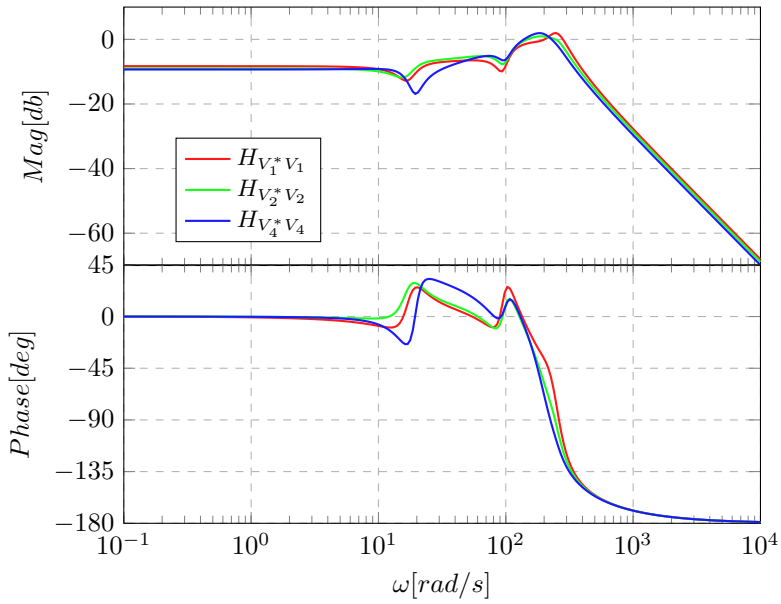

Fig. 4.8: Bode diagram of the voltage response of the linearized network seen from the secondary control layer.

These transfer functions are obtained without considering the communication delay and the sampling effect of the secondary. However, these aspects need to be taken into consideration when designing the controller. According to [80], the maximum bandwidth, that can be achieved in a system that contains delays, is smaller than $1/\theta$, where θ is the total delay of the loop. In our case, considering the communication delay and the delay introduced by the sampling of the secondary, we can determine θ, as shown in (4.8). Therefore, given the chosen values for T_d and T_s we can only expect a bandwidth smaller than 1.1765 rad/s for the central regulator.

$$\theta = T_d + \frac{T_s}{2} + T_d \tag{4.8}$$

However, high control speed is not the attribute that we desire most from the central regulator; we are more interested in a smooth response with no overshoot in order to avoid introducing perturbations in the network from the secondary control loops. For this, we can set the desired bandwidth considerably lower than the limit

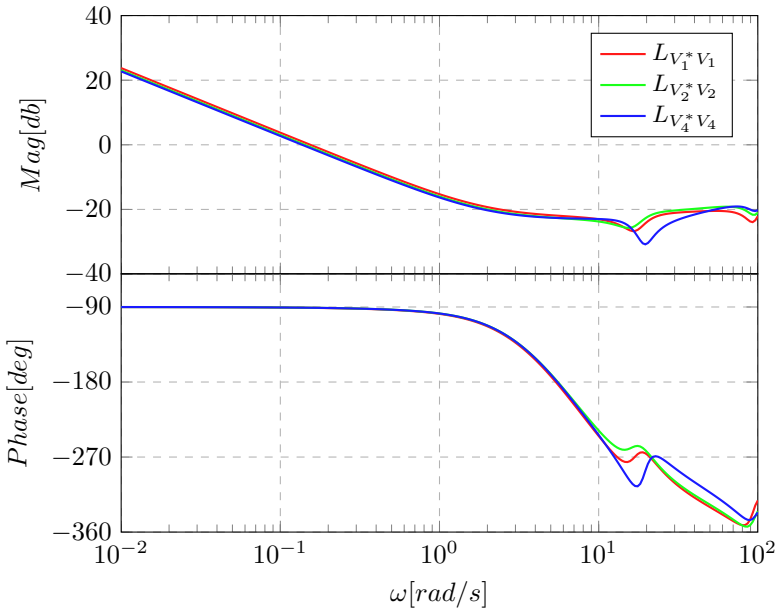

Fig. 4.9: Bode diagram of the open loop voltage dynamics.

imposed by θ.

Following this approach, we obtained the gains for the PI controllers listed in (4.9). The bode diagram of the voltage control open loop transfer function for the three terminals is displayed in Fig. 4.9. The crossover frequency is at 0.154 rad/s, 10 times slower than the limit imposed by the time delays. The system has almost 90 degrees of phase margin, therefore, we should expect a smooth response with no overshoot. More than 20 dB of gain margin should also be sufficient in order to account for modeling uncertainties.

$$\begin{aligned} K_P^{2nd} &= 0.2 \\ K_I^{2nd} &= 0.4 \end{aligned} \tag{4.9}$$

Fig. 4.10 shows the step response of the closed loop system using the PI controller and including the sampling and delay elements. It takes a little more than 30

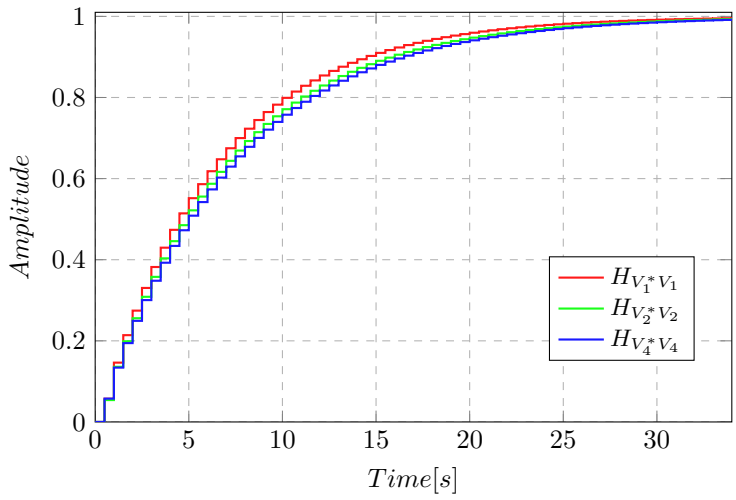

Fig. 4.10: Step response of the secondary controller

seconds for a reference change at the secondary to be followed by the network. For our purposes, we considered this design satisfactory.

4.3.2 Response of primary control

In order to see the improvement on the transmission losses brought by the secondary control layer, we are going to consider first a study case where only the primary control is enabled. The scenario starts with all buses operating at nominal voltage, therefore, there is no power flow in the network. After 0.1 seconds, a 1000 MW load change is applied at T3, followed by a 600 MW at T5 shortly afterward (at 0.8 seconds). The power unbalance creates a voltage deviation in the network which, in turn, activates the droop-based primary control.

Table 4.1: Steady state operating point of the network after the primary control

Terminal No.	1	2	3	4	5
V [kV]	387.09	387.20	385.40	386.20	382.47
P [MW]	-580.91	-512.08	1000.00	-517.59	600.00
P_{loss} [MW]	10.58				

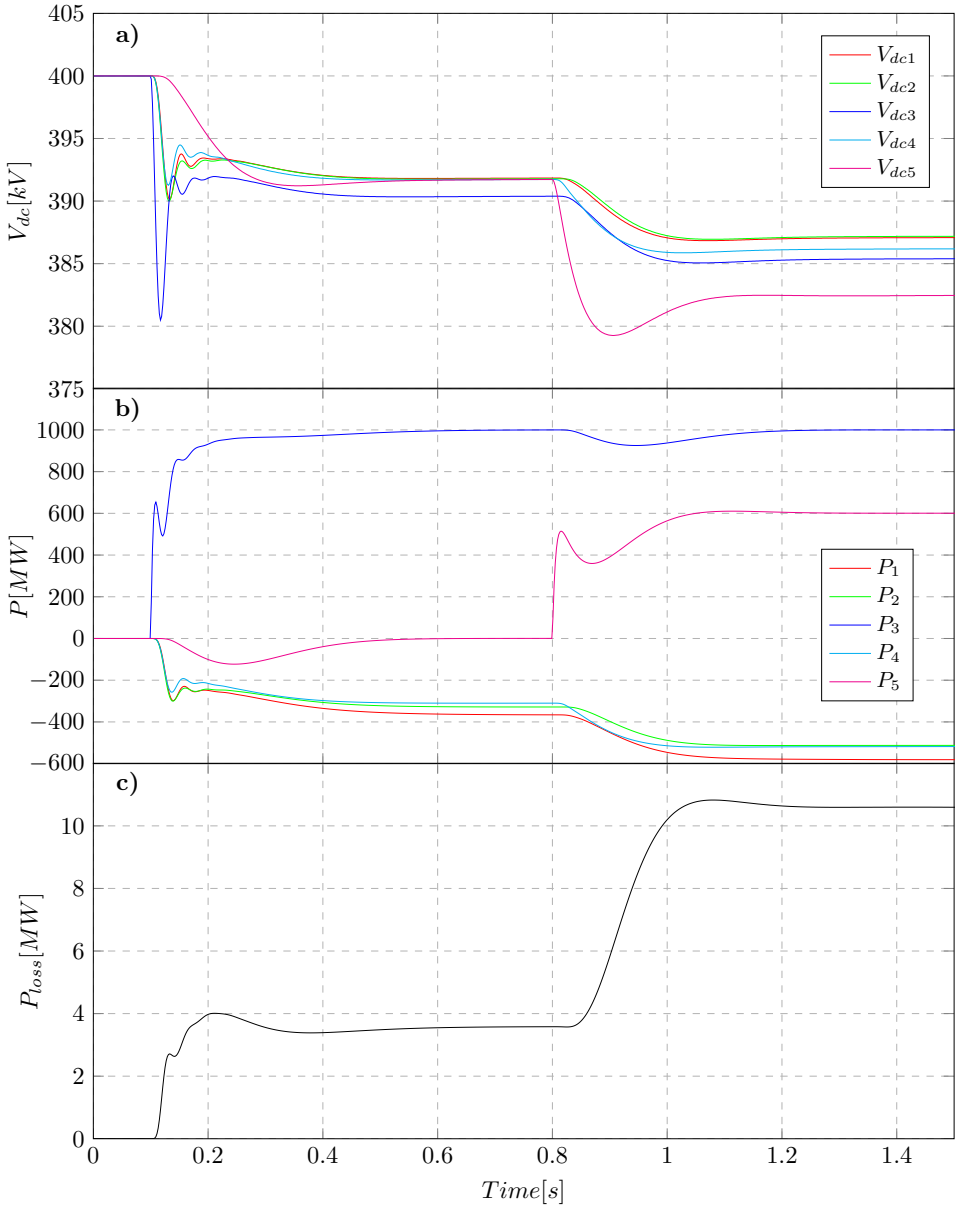

Fig. 4.11: Only primary control enabled. 1000 MW step in the load power at T3 followed by 600 MW load step at T5. Evolution of the a) nodal voltages, b) power injections, c) total transmission power loss.

As discussed extensively in the previous chapter, the power sharing at this point is influenced only by the droop-gains and by the network topology, which determines the propagation of the voltage unbalance. The voltage and the power response of the network during primary control can be seen in Fig. 4.11. Oscillations appear in the cables, but, with the proper design of the droop resistance and bus capacitance, the oscillations are properly damped.

The equilibrium point reached after the action of the primary is shown in Table 4.1. All the node voltages are below the nominal value and the total power transmission loss is equal to 10.58 MW.

4.3.3 Response of secondary control

This study case shows the coordination between the primary and secondary control. The same series of events as in the scenario presented in the previous subsection is employed, but, this time, with the secondary control activated. Fig. 4.12 shows the evolution of the nodal voltages and power injection.

While the transients at the primary level, with the help of the additional damping terms introduced in the previous chapter, die in less than 0.5s, the secondary control has a much slower control action. This behavior is expected given the fact that we designed the central regulator in order to obtain a smooth transition to the optimal operating point. The action of the secondary control at each sampling time $T_s = 0.5s$, as it drives the references of the primary control, can be seen in Fig. 4.12.

Table 4.2 shows the steady state operating point after the action of the secondary control. The losses are reduced by more than 18%, mainly due to the increase in the voltage. In the presented scenario, the converter at T4 is the closest to the loads at T3 and T5. Injecting more power from this terminal has also a large contribution to the minimization of losses. However, the power reference that the algorithm computes for this node respects the node ratings as a consequence of the inequality constraints set in the definition of the problem. As seen in Table 4.2, the converter at T4 has to operate at its nominal power according to the new OP, calculated by the operating power point calculator.

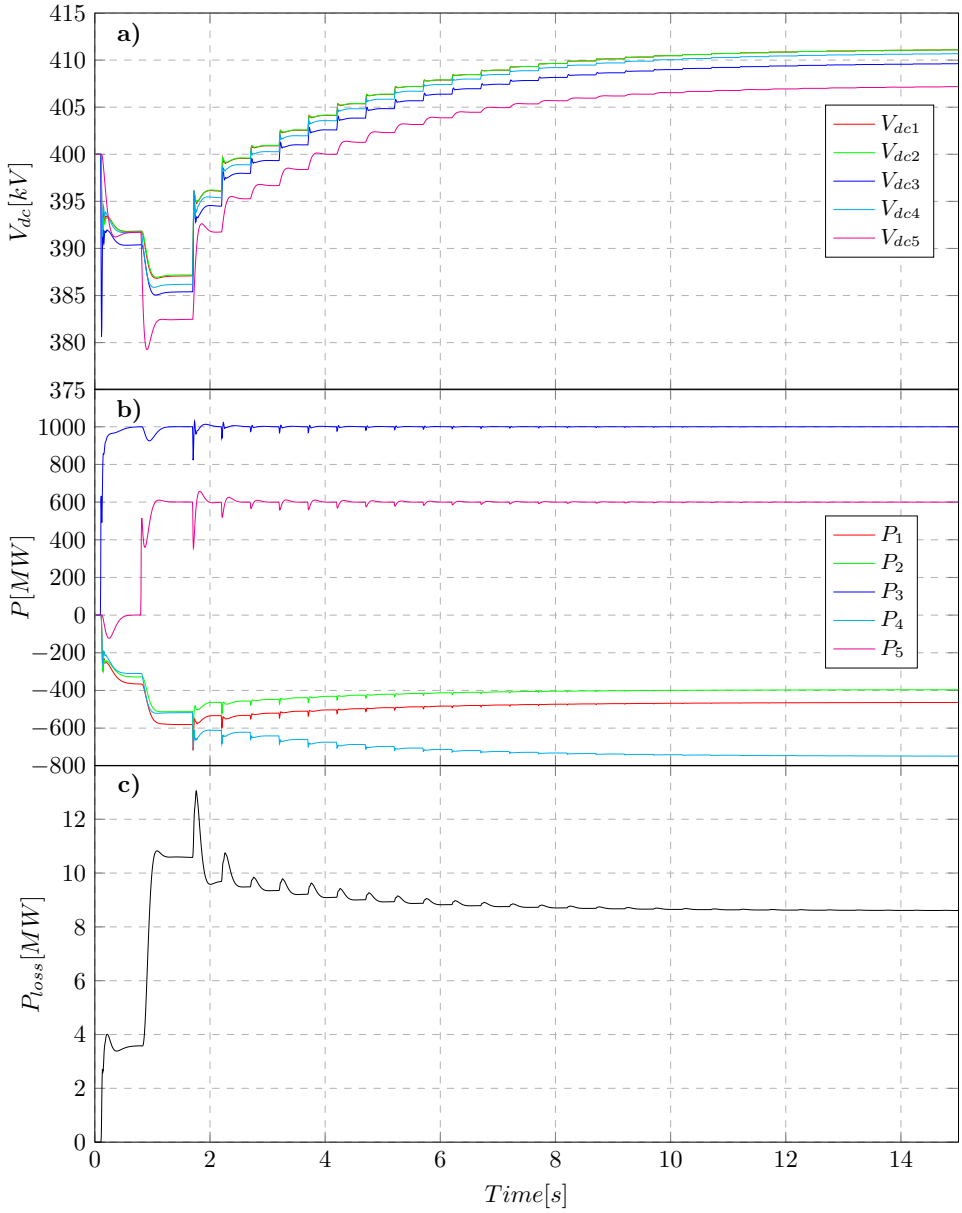

Fig. 4.12: Primary and secondary control are enabled. 1000 MW step in the load power at T3 followed by 600 MW load step at T5. Evolution of the a) nodal voltages, b) power injections, c) total transmission power loss.

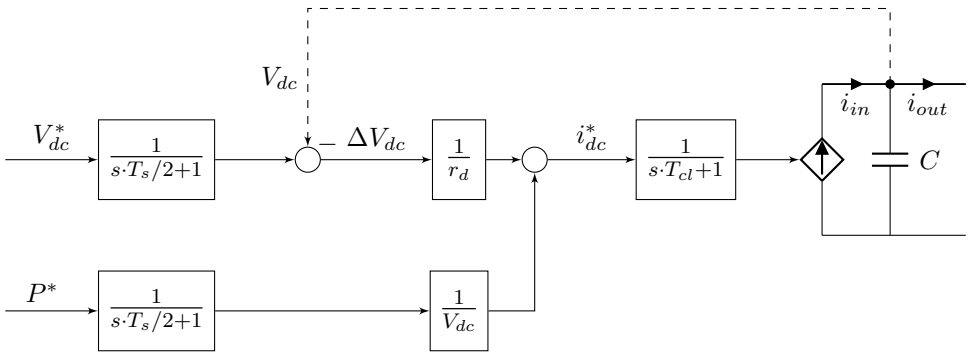

Fig. 4.13: Control structure of droop-based primary with additional filters on the secondary control inputs.

Table 4.2: Steady state operating point of the network after the secondary control

Terminal No.	1	2	3	4	5
V [kV]	411.20	411.20	409.73	410.79	407.29
P [MW]	-462.97	-395.63	1000.00	-749.99	600.00
P_{loss} [MW]	8.59				

The voltage response shown in Fig. 4.12, while it achieves its reference value and serves our purpose, presents small overshoots with each step transient; this behavior we did not observe in the step response of the system, i.e., in Fig. 4.10, while designing the central regulator. This is because the secondary control is not aware of what happens in the system between samples.

In order to smooth this voltage transient, we can slow down the effect of the input signals controlled by the secondary by mounting additional filters, as shown in Fig. 4.13. Taking into consideration that the secondary control sends a new reference every T_s, it makes no sense for the primary control to try to follow the reference faster than this. The filters that we show in Fig. 4.13 have a time constant equal to $T_s/2$, which means that when a new reference value will arrive from the secondary, the primary has reached almost 90% of the previous reference. Using these filters, we executed again the scenario of Fig. 4.12 and obtained the results shown in Fig. 4.14. The steady state operating point reached by the system is the same, only

now the transient is improved; the step-like response is smoothed by the filters.

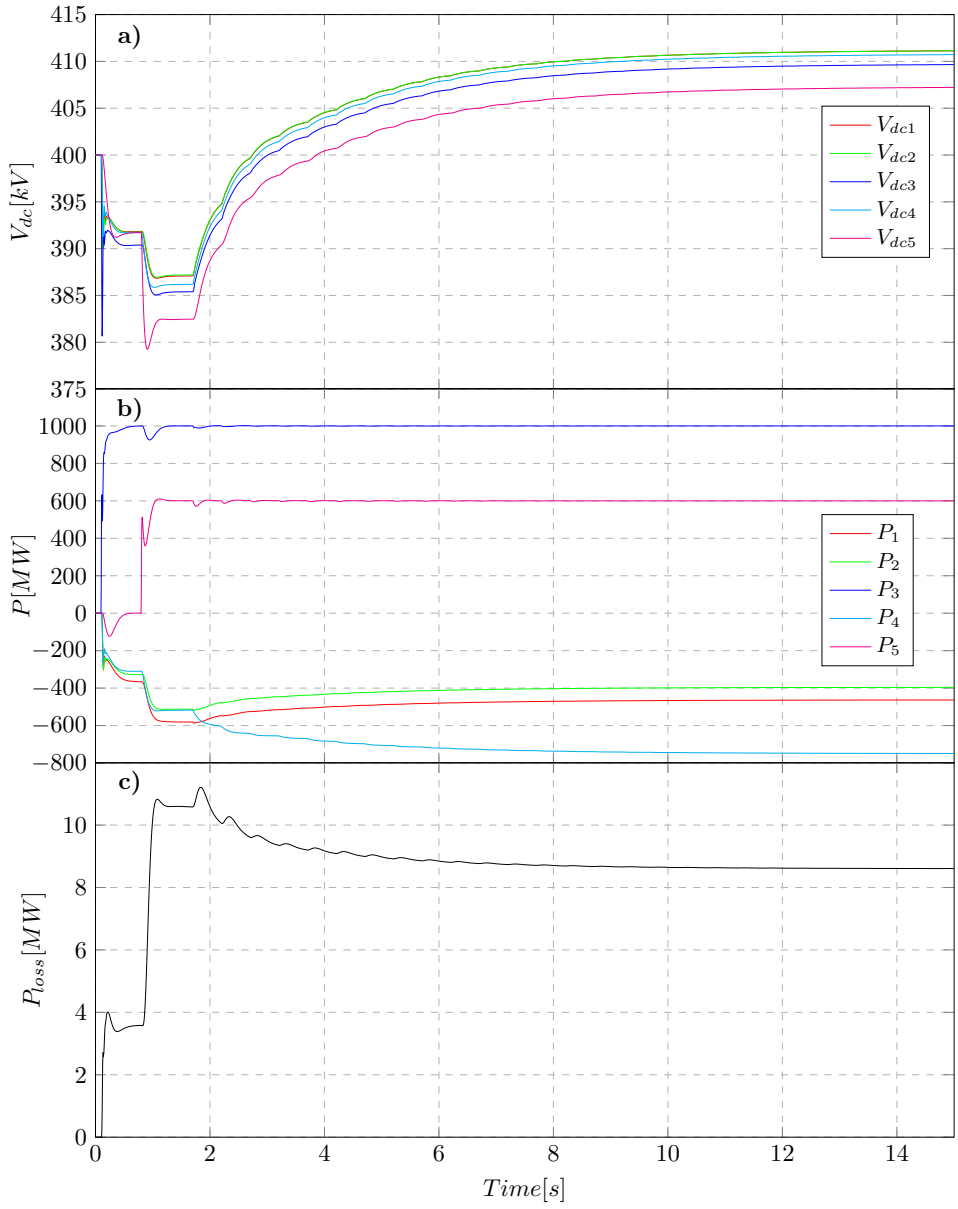

Fig. 4.14: Primary and secondary control are enabled. Additional filters mounted on the reference inputs.1000 MW step in the load power at T3 followed by 600 MW load step at T5. Evolution of the a) nodal voltages, b) power injections, c) total transmission power loss.

Table 4.3: Steady state operating point of the network after the secondary control

Terminal No.	1	2	3	4	5
V [kV]	428.10	428.10	428.10	428.10	424.75
P [MW]	0.00	0.00	0.00	-604.74	600.00
P_{loss} [MW]	4.74				

4.3.4 Response of secondary control - trip of converter

In the previous scenario, the transmission losses could be improved even more if the voltage of the network would be allowed to increase. However, the voltage limit calculator block bounds the maximum operating voltage in order to allow some headroom for possible transients. In order to exemplify why this is necessary, we consider the following scenario, which is a continuation of the study case from the previous subsection. The transient of the secondary controller has finished and the voltage and power have reached the steady OP listed earlier in Table 4.2. Then, at t=15 s the load at T3 trips.

While step increases in load are atypical for a network, the trip of a load is something that can occur in reality. A large voltage overshoot at T3 can be observed in Fig. 4.15a, but the voltage is maintained in the safety band, as we expected. This is because the voltage limits used in the optimization algorithm are calculated previously by the limit calculator block by analyzing the equivalent peak impedance seen from each converter.

After the load at T3 is disconnected, the only remaining load in the network is at T5. Since this load is rather small, it will not impose so tight limits on the maximum operating voltage, therefore, the OP calculated by the secondary control will be at a higher voltage. As seen in Fig. 4.15a, the secondary control starts to increase the voltage in the network.

The new OP calculated for the network is listed in Table 4.3. The load at T5 is smaller than the rating of the converter at T4, therefore, it can be supplied only from this terminal, and the secondary control correctly identifies this OP. T1, T2, T3, and T4 are operated at the same voltage in order to avoid power flow between them and the voltage at which they are operated is given by the load at T5, so that, in case of

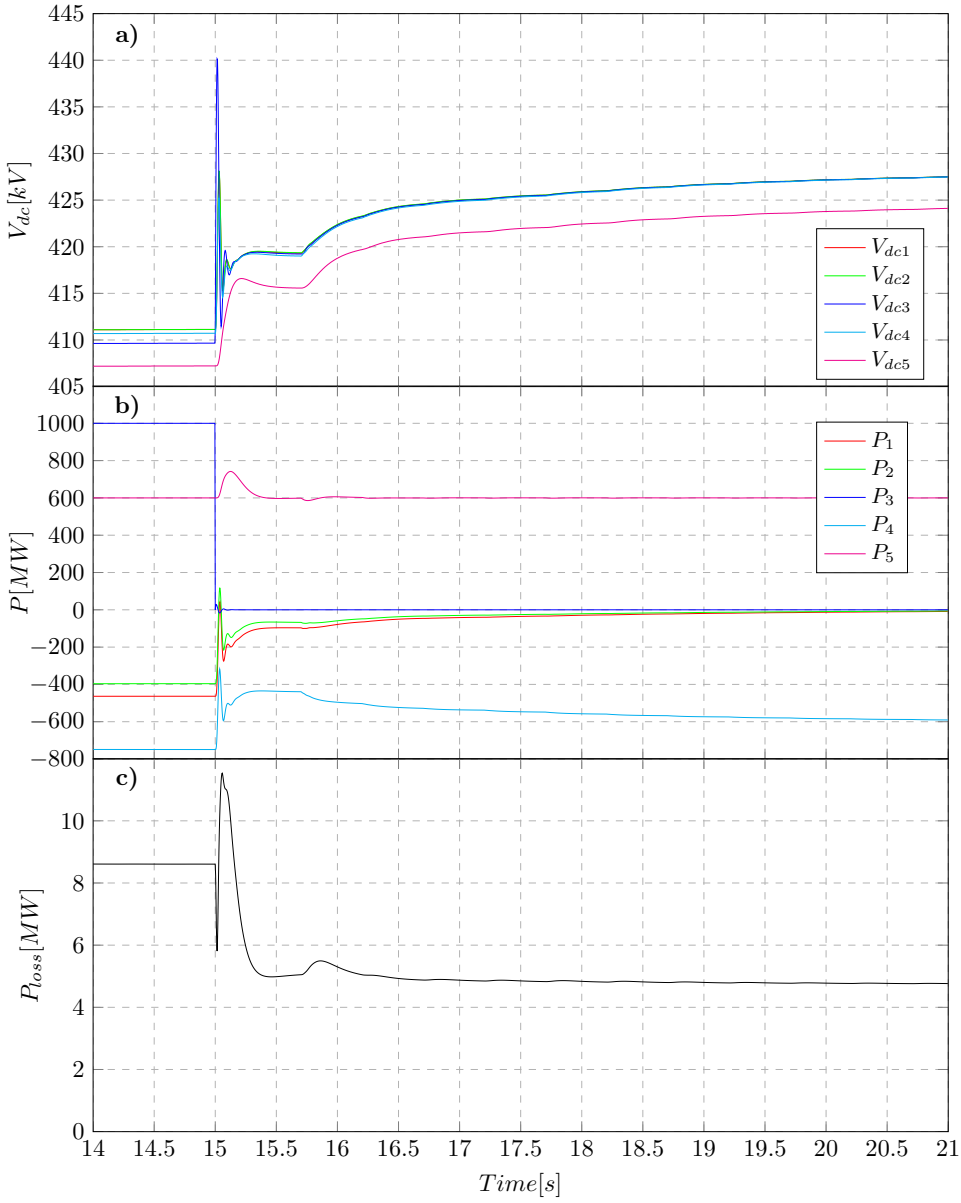

Fig. 4.15: Primary and secondary control are enabled. Additional filters mounted on the reference inputs. The converter at T3 trips. Evolution of the a) nodal voltages, b) power injections during transients, c) total transmission power loss.

a trip, the voltage will not overrun the safety operating band.

4.4 Conclusions

In this chapter we presented our proposal for the structure of a hierarchical control architecture for MTDC networks. In this approach, the primary control is implemented and sized as described in the previous chapters. Meanwhile, the secondary control is proposed as a centralized controller that acts as a global operation optimizer. Based on power and voltage measurements from the entire network, the secondary control recalculates the operating points of the primary control in an attempt to minimize a predefined objective function, which, in our case, is the transmission losses.

More than approaching the problem of OPF in MTDC networks, the work presented in this chapter also showed how the secondary has to drive the references of the primary without perturbing the system. For this, a central regulator based on a closed loop integral control was proposed and guidelines for tuning this controller were offered.

Besides the operating point calculator and the central regulator, we identified another important functional block for the structure of the secondary control, i.e., the voltage limit calculator. Knowing the operation limits for the voltage is crucial for the safe operation of the network, as headroom for possible transients should be allowed.

The proposed methods were tested in simulation by implementing a secondary control layer for the five terminal network used in the previous chapter. The parameters for the primary control and for the structure of the network, obtained in the previous chapter, were maintained identical and, on top of them, a centralized secondary controller was designed. The response of the system with only the primary control and both primary and secondary was compared. For the studied scenario, a reduction in the transmission losses of 18% was noticed between the operating point determined by the primary and the operating point calculated by the secondary.

We have also shown the importance of the voltage limit calculator by testing

the response of the system to a sudden load trip. It was shown that the secondary control increases the voltage of the system only up to the limit that guarantees that the voltage will remain in the corresponding operating limits, even for large load transients.

The results and methodologies shown in this chapter, even though they brush on some new topics regarding hierarchical control in MTDC grids, are still missing some aspects in order for them to be considered applicable in a practical scenario. First of all, the measurements received from the network have to be validated and corrected as power flow in dc grids is very sensible to uncertainties. Secondly, the algorithm used for calculating the optimal OP of the network has to be extended by taking into account the neighboring ac-areas and the price of energy imported or exported from each area. Rather than calculating the OP of the network so that the power loss is minimized, one could imagine more advanced algorithms that maximize the profitability of the dc-network. However, it should not be forgotten that the main purpose of the secondary control is to restore the voltage of the network to the NO band after the transient at the primary has finished. For the moment, we will leave the debate regarding what objective function is the most suitable to be implemented in the operating point calculator for future discussions and research.

Chapter 5

Conclusions and future work

5.1 Conclusions

The work presented in this thesis addresses the control and operation of MTDC networks and it follows the natural flow of questions and ideas that guided our development.

The starting point of the thesis was the control of a dc-dc converter connected to an energy storage unit. This dc-dc converter was planned as part of a PV power plant that also integrates ES in order to be able to provide services to the grid. Therefore, the dc-dc converter of the battery, together with the dc-dc converter of the PV generator and the grid connected inverter formed our initial three terminal dc bus. In this simple scenario, the dc-dc converter connected to the battery could regulate the dc bus voltage, but then the question of what would happen if more terminals are added to this dc-network arose. This led us to investigate decentralized control options and we started to notice the similarities and differences between dc networks and ac networks and, also, the lack of standardization in the control and operation of dc-networks. Also, we observed that there are no works addressing the integration of ES into networks.

Around these lines is where our work tries to make a first contribution. As described in details in Chapter 2, we propose a generalized droop control strategy that is based on the combination of a classic droop control method and dc-bus signaling methods in order to provide a more generic and flexible control solution that takes into account the state of the network. Five operating voltage bands are defined

for the network and, based on these operating bands, several droop characteristics are designed for the various elements that might be encountered in the network. A special droop characteristic is proposed for the interconnection of ES. Taking the voltage as well as the state of charge of the ES into account, the droop characteristic becomes a complex surface that avoids the overcharge and the deep-discharge of the ES. The proposed methods are tested through various simulation scenarios and validated through experimental results, explaining with great details the interaction between the different droop curves in different operating scenarios.

Once we developed the primary control strategy, we started to ask ourselves how its parameters have to be sized and, moreover, what are the important parameters that influence the voltage control of the network. Since we found very little information on this topic in the literature, we dedicated a part of the work in order to shed some light on these aspects. This is reflected in the ideas presented in Chapter 3. Here, we firstly show how the value of the droop resistance, together with the output capacitor and the time constant of the current loop, have a direct impact on the transient voltage overshoot that can occur at the terminals of the converter in the case of a sudden load trip. This voltage overshoot has to be bounded by the operating bands defined for the operation of the network. Afterward, we extend the analysis by looking at how the parameters of the connecting cables influence the transient voltages and, therefore, the design of the system. Further on, an improved droop control strategy that attenuates the voltage oscillations during transients was proposed. The presented methods were validated on a study case built around a five terminal dc network proposed in the literature. Starting from the structure of the network and the power rating of the converters at each terminal, the output capacitors and the primary control layer are designed together in order to ensure acceptable voltage transients. The importance of the output capacitor, as the only inertial element of the grid, is highlighted.

During the work on the design of the network it became clear that a large system, in order to work properly, would require a secondary control unit to restore the voltages back to their normal operating band after each transient. The need of the secondary controller is, on one hand, due to the proportional effect of the droop

control and, on the other hand, due to the voltage drops on the cable resistances that make possible the calculation of the voltage profile of the network only from a centralized controller. For this, we proposed a secondary controller, based on low bandwidth communication, that regulates the voltage profile of the network so that optimal power flow is achieved. More than approaching the problem of optimal power flow in dc networks, the work presented in Chapter 4 tries to elaborate, both analytically and through simulations, on the coordination between the primary and secondary control layers. One of the contributions of this chapter includes how local primary controllers have to be driven by the centralized controller in order to ensure a smooth transition to the optimal operating point. Another important aspect that is highlighted here is the need of limiting the voltage increase when a new operating point is calculated. Algorithms that try to minimize the power losses in the network will have the tendency to increase the voltage in the network, however, how much the voltage at each bus can be increased has to be computed apriori in order to allow headroom for possible transients. For this, we included a voltage limit calculator block in the operation of the secondary controller. This functional block evaluates the voltage transients that might occur in the network by looking at the peak impedance seen from the terminals of the converter.

Overall, in the end, we obtained a functional hierarchical control architecture that we tested through simulation in different operating scenarios. While we managed to touch some of the aspects regarding the operation of dc networks, a lot of research and development is still required in this field before a standard will be reached. Some of the ideas that we did not get to approach in this thesis, but we think that are essential for the practical operation of our control architecture, are described in the next section.

5.2 Future work

An important aspect that should be pursued in the future, and it was completely left out of the scope of this thesis, is the measurement validation and correction block of the secondary controller. The importance of correct measurements is crucial for

the operation of the secondary control. This is due to the fact that, the voltage is controlled in multiple points by PI controller. Hence, the voltage profile that the secondary control tries to enforce on the network has to be achievable by the network, otherwise the integrators will saturate and the control might be lost. Therefore, either a very precise measurement validation block should be implemented, either a new control method that allows for these uncertainties should be designed for the secondary control.

Also, at the secondary control, the optimal power flow algorithm should be extended so that it takes into account the neighboring ac areas. Moreover, the possibility for new objective functions for the optimization algorithm should be considered. Such optimization functions could approach economical aspects and could take into account also the presence of the energy storage elements. Here, an assessment of whether a tertiary control layer is needed for MTDC networks and what functionalities must be included at this level should be performed.

Another interesting aspect that is still left in the dark is the dynamic interaction between the dc network and the ac network. A converter interfacing the dc grid with the ac grid should implement a rather complex control algorithm. On one hand, in order to participate in the dc-voltage control it would require fast power dynamics as the time constants on the dc-side are quite fast, on the other hand, in order to comply with requirements regarding inertial response, the inverter will require more slow dynamics on the ac-side. How these two aspects can be satisfied, and how the two networks interact with each other through the interface converter is certainly something worth investigating in the future.

References

[1] GWEC, "Global wind report annual market update 2013," Global Wind Energy Council, Tech. Rep., 2013.

[2] EPIA, "Global Market Outlook for Photovoltaics 2014-2018," European Photovoltaic Industry Association, Brussels, Tech. Rep., 2013.

[3] J. Eyer, "Energy Storage for the Electricity Grid : Benefits and Market Potential Assessment Guide A Study for the DOE Energy Storage Systems Program," Sandia National Laboratories, Albuquerque, Tech. Rep. February, 2010.

[4] P. Sciences and Y. Rebours, "A Comprehensive Assessment of Markets for Frequency and Voltage Control Ancillary Services," Ph.D. dissertation, University of Manchester, 2008.

[5] K. Alanne and A. Saari, "Distributed energy generation and sustainable development," *Renewable and Sustainable Energy Reviews*, vol. 10, no. 6, pp. 539–558, Dec. 2006. [Online]. Available: http://linkinghub.elsevier.com/retrieve/pii/S1364032105000043

[6] T. Ackermann, G. Andersson, and L. Söder, "Distributed generation: a definition," *Electric Power Systems Research*, vol. 57, no. 3, pp. 195–204, Apr. 2001. [Online]. Available: http://linkinghub.elsevier.com/retrieve/pii/S0378779601001018

[7] S. M. Schoenung and J. Eyer, "Benefit / Cost Framework for Evaluating Modular Energy Storage A Study for the DOE Energy Storage Systems Program," Sandia National Laboratories, Albuquerque, Tech. Rep. February, 2008.

[8] IEEE Transmission and Distribution Committee, "HVDC project listing," HVDC and Flexible AC Transmission Subcommittee, Tech. Rep., 2012.

[9] M. Barnes and A. Beddard, "Voltage Source Converter HVDC Links - The State of the Art and Issues Going Forward," *Energy Procedia*, vol. 24, no. 0, pp. 108–122, 2012. [Online]. Available: http://www.sciencedirect.com/science/article/pii/S1876610212011320

[10] J. Peralta, H. Saad, S. Dennetiere, J. Mahseredjian, and S. Nguefeu, "Detailed and Averaged Models for a 401-Level MMC-HVDC System," *Power Delivery, IEEE Transactions on*, vol. 27, no. 3, pp. 1501–1508, 2012.

[11] T. M. Haileselassie, M. Molinas, and T. Undeland, "Multi-Terminal VSC-HVDC System for Integration of Offshore Wind Farms and Green Electrification of Platforms in the North Sea," in *Proceedings of Nordic Workshop on Power and Industrial Electronics*, Espoo, Finland, 2008, pp. 1–8.

[12] S. Cole, J. Beerten, and R. Belmans, "Generalized Dynamic VSC MTDC Model for Power System Stability Studies," *IEEE Transactions on Power Systems*, vol. 25, no. 3, pp. 1655–1662, 2010.

[13] O. Gomis-Bellmunt, J. Liang, J. Ekanayake, and N. Jenkins, "Voltage-current characteristics of multiterminal HVDC-VSC for offshore wind farms," *Electric Power Systems Research*, vol. 81, no. 2, pp. 440–450, Feb. 2011. [Online]. Available: http://www.sciencedirect.com/science/article/pii/S0378779610002403

[14] C. Dierckxsens, K. Srivastava, M. Reza, S. Cole, J. Beerten, and R. Belmans, "A distributed DC voltage control method for VSC MTDC systems," *Electric Power Systems Research*, vol. 82, no. 1, pp. 54–58, Jan. 2012. [Online]. Available: http://www.sciencedirect.com/science/article/pii/S0378779611001933

[15] T. M. Haileselassie and K. Uhlen, "Power System Security in a Meshed North

Sea HVDC Grid," *Proceedings of the IEEE*, vol. 101, no. 4, pp. 978–990, 2013.

[16] M. K. Bucher, R. Wiget, G. Andersson, and C. M. Franck, "Multiterminal HVDC Networks-What is the Preferred Topology?" *Power Delivery, IEEE Transactions on*, vol. 29, no. 1, pp. 406–413, 2014.

[17] T. M. Haileselassie and K. Uhlen, "Precise control of power flow in multiterminal VSC-HVDCs using DC voltage droop control," in *Power and Energy Society General Meeting, 2012 IEEE*, 2012, pp. 1–9.

[18] R. da Silva, R. Teodorescu, and P. Rodriguez, "Multilink DC transmission system for supergrid future concepts and wind power integration," in *Renewable Power Generation (RPG 2011), IET Conference on*, 2011, pp. 1–6.

[19] K. Meah and A. H. M. S. Ula, "A new simplified adaptive control scheme for multi-terminal HVDC transmission systems," *International Journal of Electrical Power & Energy Systems*, vol. 32, no. 4, pp. 243–253, May 2010. [Online]. Available: http://www.sciencedirect.com/science/article/pii/S0142061509001537

[20] L. Xu, B. W. Williams, and L. Yao, "Multi-terminal DC transmission systems for connecting large offshore wind farms," in *Power and Energy Society General Meeting - Conversion and Delivery of Electrical Energy in the 21st Century, 2008 IEEE*, 2008, pp. 1–7.

[21] N. R. Chaudhuri, R. Majumder, B. Chaudhuri, and J. Pan, "Stability Analysis of VSC MTDC Grids Connected to Multimachine AC Systems," *IEEE Transactions on Power Delivery*, vol. 26, no. 4, pp. 2774–2784, 2011.

[22] G. O. Kalcon, G. P. Adam, O. Anaya-Lara, S. Lo, and K. Uhlen, "Small-Signal Stability Analysis of Multi-Terminal VSC-Based DC Transmission Systems," *IEEE Transactions on Power Systems*, vol. 27, no. 4, pp. 1818–1830, 2012.

[23] M. E. Baran and N. R. Mahajan, "Overcurrent Protection on Voltage-Source-Converter-Based Multiterminal DC Distribution Systems," *IEEE Transactions on Power Delivery*, vol. 22, no. 1, pp. 406–412, 2007.

[24] L. Tang and B.-T. Ooi, "Locating and Isolating DC Faults in Multi-Terminal DC Systems," *IEEE Transactions on Power Delivery*, vol. 22, no. 3, pp. 1877–1884, 2007.

[25] J. Yang, J. E. Fletcher, and J. O'Reilly, "Multiterminal DC Wind Farm Collection Grid Internal Fault Analysis and Protection Design," *IEEE Transactions on Power Delivery*, vol. 25, no. 4, pp. 2308–2318, 2010.

[26] ——, "Short-Circuit and Ground Fault Analyses and Location in VSC-Based DC Network Cables," *IEEE Transactions on Industrial Electronics*, vol. 59, no. 10, pp. 3827–3837, 2012.

[27] O. Nanayakkara, A. D. Rajapakse, and R. Wachal, "Traveling-Wave-Based Line Fault Location in Star-Connected Multiterminal HVDC Systems," *IEEE Transactions on Power Delivery*, vol. 27, no. 4, pp. 2286–2294, 2012.

[28] B. Silva, C. L. Moreira, L. Seca, Y. Phulpin, and J. A. P. Lopes, "Provision of Inertial and Primary Frequency Control Services Using Offshore Multiterminal HVDC Networks," *IEEE Transactions on Sustainable Energy*, vol. 3, no. 4, pp. 800–808, 2012.

[29] J. Dai, Y. Phulpin, A. Sarlette, and D. Ernst, "Coordinated primary frequency control among non-synchronous systems connected by a multi-terminal high-voltage direct current grid," *Generation, Transmission & Distribution, IET*, vol. 6, no. 2, pp. 99–108, 2012.

[30] T. M. Haileselassie and K. Uhlen, "Primary frequency control of remote grids connected by multi-terminal HVDC," in *Power and Energy Society General Meeting, 2010 IEEE*, 2010, pp. 1–6.

[31] ——, "Frequency sensitivity analysis of ac grids connected to MTDC grid," in *AC and DC Power Transmission, 2010. ACDC. 9th IET International Conference on*, 2010, pp. 1–5.

[32] A. Gomez-Exposito, J. M. Mauricio, and J. M. Maza-Ortega, "VSC-Based MVDC Railway Electrification System," *Power Delivery, IEEE Transactions on*, vol. 29, no. 1, pp. 422–431, 2014.

[33] K. Sun, L. Zhang, Y. Xing, and J. M. Guerrero, "A Distributed Control Strategy Based on DC Bus Signaling for Modular Photovoltaic Generation Systems With Battery Energy Storage," *IEEE Transactions on Power Electronics*, vol. 26, no. 10, pp. 3032–3045, Oct. 2011. [Online]. Available: http://ieeexplore.ieee.org/lpdocs/epic03/wrapper.htm?arnumber=5730500

[34] X.-P. Zhang, "Multiterminal voltage-sourced converter-based HVDC models for power flow analysis," *IEEE Transactions on Power Systems*, vol. 19, no. 4, pp. 1877–1884, 2004.

[35] J. Bryan, R. Duke, and S. Round, "Decentralized generator scheduling in a nanogrid using DC bus signaling," in *Power Engineering Society General Meeting, 2004. IEEE*, 2004, pp. 977–982 Vol.1.

[36] K. Kurohane, A. Uehara, T. Senjyu, A. Yona, N. Urasaki, T. Funabashi, and C.-H. Kim, "Control strategy for a distributed DC power system with renewable energy," *Renewable Energy*, vol. 36, no. 1, pp. 42–49, Jan. 2011. [Online]. Available: http://linkinghub.elsevier.com/retrieve/pii/S096014811000251X

[37] J. Schonberger, R. Duke, and S. D. Round, "DC-Bus Signaling: A Distributed Control Strategy for a Hybrid Renewable Nanogrid," *IEEE Transactions on Industrial Electronics*, vol. 53, no. 5, pp. 1453–1460, 2006.

[38] D.-C. Lu and V. G. Agelidis, "Photovoltaic-Battery-Powered DC Bus System for Common Portable Electronic Devices," *IEEE Transactions on Power Delivery*, vol. 24, no. 3, pp. 849–855, 2009.

[39] K. Kurohane, T. Senjyu, A. Yona, N. Urasaki, T. Goya, and T. Funabashi, "A Hybrid Smart AC/DC Power System," *Smart Grid, IEEE Transactions on*, vol. 1, no. 2, pp. 199–204, 2010.

[40] J. M. Guerrero, J. C. Vasquez, J. Matas, L. G. de Vicuna, and M. Castilla, "Hierarchical Control of Droop-Controlled AC and DC Microgrids- A General Approach Toward Standardization," *IEEE Transactions on Industrial Electronics*, vol. 58, no. 1, pp. 158–172, 2011.

[41] K. Rouzbehi, C. Gavriluta, I. Candela, A. Luna, and P. Rodriguez, "Comprehensive Analogy between Conventional AC Grids and DC grids Characteristics," in *IEEE, IECON*, Vienna, Austria, 2013.

[42] V. Akhmatov, M. Callavik, C. M. Franck, S. E. Rye, T. Ahndorf, M. K. Bucher, H. Muller, F. Schettler, and R. Wiget, "Technical Guidelines and Prestandardization Work for First HVDC Grids," *Power Delivery, IEEE Transactions on*, vol. 29, no. 1, pp. 327–335, 2014.

[43] T. K. Vrana, J. Beerten, R. Belmans, and O. B. Fosso, "A classification of DC node voltage control methods for HVDC grids," *Electric Power Systems Research*, vol. 103, pp. 137–144, Oct. 2013. [Online]. Available: http://www.sciencedirect.com/science/article/pii/S0378779613001193

[44] T. M. Haileselassie and K. Uhlen, "Impact of DC Line Voltage Drops on Power Flow of MTDC Using Droop Control," *IEEE Transactions on Power Systems*, vol. 27, no. 3, pp. 1441–1449, 2012.

[45] M. Aragüés-Peñalba, A. Egea-Àlvarez, O. Gomis-Bellmunt, and A. Sumper, "Optimum voltage control for loss minimization in HVDC multi-terminal transmission systems for large offshore wind farms," *Electric Power Systems Research*, vol. 89, pp. 54–63, Aug. 2012. [Online]. Available: http://www.sciencedirect.com/science/article/pii/S0378779612000478

[46] M. Aragüés-Peñalba, A. Egea-Àlvarez, S. G. Arellano, and O. Gomis-Bellmunt, "Droop control for loss minimization in HVDC multi-terminal

transmission systems for large offshore wind farms," *Electric Power Systems Research*, vol. 112, no. 0, pp. 48–55, Jul. 2014. [Online]. Available: http://www.sciencedirect.com/science/article/pii/S037877961400100X

[47] A. Egea-Alvarez, J. Beerten, D. Van Hertem, and O. Gomis-Bellmunt, "Primary and secondary power control of multiterminal HVDC grids," in *AC and DC Power Transmission (ACDC 2012), 10th IET International Conference on*, 2012, pp. 1–6.

[48] P. Kundur, *Power System Stability and Control*, epri power ed. McGraw-Hill Education, 1994, vol. 23.

[49] B4-58 and B4-57, "The CIGRE B4 DC Grid Test System," Cigre SC B4 HVDC and Power Electronics, Tech. Rep., 2013. [Online]. Available: http://b4.cigre.org/Publications/Documents-related-to-the-development-of-HVDC-Grids

[50] J. Machowski, J. W. Bialek, and J. R. Bumby, *Power System Dynamics: Stability and Control*.

[51] ENSTSO-E, "Continental Europe Operation Handbook," Tech. Rep. [Online]. Available: www.entsoe.eu

[52] G. Anderson, "Dynamics and Control of Electric Power Systems," 2012.

[53] T. M. Haileselassie, R. E. Torres-Olguin, T. K. Vrana, K. Uhlen, and T. Undeland, "Main grid frequency support strategy for VSC-HVDC connected wind farms with variable speed wind turbines," in *PowerTech, 2011 IEEE Trondheim*, 2011, pp. 1–6.

[54] O. Gomis-Bellmunt, J. Liang, J. Ekanayake, N. Jenkins, and R. King, "Topologies of multiterminal HVDC-VSC transmission for large offshore wind farms," *Electric Power Systems Research*, vol. 81, no. 2, pp. 271–281, Feb. 2011. [Online]. Available: http://www.sciencedirect.com/science/article/pii/S0378779610002166http://www.sciencedirect.com/science/article/pii/S0378779610002403

[55] L. Zhang, K. Sun, Y. Xing, L. Feng, and H. Ge, "A Modular Grid-Connected Photovoltaic Generation System Based on DC Bus," *IEEE Transactions on Power Electronics*, vol. 26, no. 2, pp. 523–531, 2011.

[56] J. Holtz and K.-H. Werner, "Multi-inverter UPS system with redundant load sharing control," *Industrial Electronics, IEEE Transactions on*, vol. 37, no. 6, pp. 506–513, 1990.

[57] Y. Zhang and H. Ma, "Theoretical and Experimental Investigation of Networked Control for Parallel Operation of Inverters," *Industrial Electronics, IEEE Transactions on*, vol. 59, no. 4, pp. 1961–1970, 2012.

[58] G. S. Thandi, R. Zhang, K. Xing, F. C. Lee, and D. Boroyevich, "Modeling, control and stability analysis of a PEBB based DC DPS," *IEEE Transactions on Power Delivery*, vol. 14, no. 2, pp. 497–505, 1999.

[59] L. Xu and L. Yao, "DC voltage control and power dispatch of a multi-terminal HVDC system for integrating large offshore wind farms," *Renewable Power Generation, IET*, vol. 5, no. 3, pp. 223–233, 2011.

[60] S. Rodrigues, R. T. Pinto, P. Bauer, and J. Pierik, "Optimal Power Flow Control of VSC-Based Multiterminal DC Network for Offshore Wind Integration in the North Sea," *Emerging and Selected Topics in Power Electronics, IEEE Journal of*, vol. 1, no. 4, pp. 260–268, 2013.

[61] T. M. Haileselassie, "Control , Dynamics and Operation of Multi-terminal VSC-HVDC Transmission Systems," Ph.D. dissertation, Norwegian University of Science and Technology, 2012.

[62] A. Szumanowski, "Battery Management System Based on Battery Nonlinear Dynamics Modeling," *IEEE Transactions on Vehicular Technology*, vol. 57, no. 3, pp. 1425–1432, May 2008. [Online]. Available: http://ieeexplore.ieee.org/lpdocs/epic03/wrapper.htm?arnumber=4382919

[63] W. X. Shen, C. C. Chan, E. W. C. Lo, and K. T. Chau, "Estimation of battery available capacity under variable discharge currents," *Journal of Power Sources*, vol. 103, no. February 2001, pp. 180–187, 2002.

[64] M. Coleman, C. K. Lee, C. Zhu, W. G. Hurley, and A. S.-o.-c. Soc, "State-of-Charge Determination From EMF Voltage Estimation : Using Impedance , Terminal Voltage , and Current for Lead-Acid and Lithium-Ion Batteries," *IEEE Transactions on Industrial Electronics*, vol. 54, no. 5, pp. 2550–2557, 2007.

[65] D. Deepti and V. Ramanarayanan, "State of charge of lead acid battery," *2006 India International Conference on Power Electronics*, pp. 89–93, Dec. 2006. [Online]. Available: http://ieeexplore.ieee.org/lpdocs/epic03/wrapper.htm?arnumber=4685347

[66] M. Paolone, "Seal-healing Operation of Microgrids with Battery Energy Storage Systems (BESS)," pp. 1–45, 2012.

[67] W. X. Shen, C. C. Chan, E. W. C. Lo, and K. T. Chau, "A new battery available capacity indicator for electric vehicles using neural network," *Energy Conversion and Management*, vol. 43, pp. 817–826, 2002.

[68] A. J. Salkind, C. Fennie, P. Singh, T. Atwater, and D. E. Reisner, "Determination of state-of-charge and state-of-health of batteries by fuzzy logic methodology," *Journal of Power Sources*, vol. 80, no. 1-2, pp. 293–300, Jul. 1999. [Online]. Available: http://linkinghub.elsevier.com/retrieve/pii/S0378775399000798

[69] S. Malkhandi, "Fuzzy logic-based learning system and estimation of state-of-charge of lead-acid battery," *Engineering Applications of Artificial Intelligence*, vol. 19, no. 5, pp. 479–485, Aug. 2006. [Online]. Available: http://linkinghub.elsevier.com/retrieve/pii/S0952197606000133

[70] I.-H. Li, W.-Y. Wang, S. Member, S.-F. Su, and Y.-S. Lee, "A Merged Fuzzy

Neural Network and Its Applications in Battery State-of-Charge Estimation," *IEEE Transactions on Energy Conversion*, vol. 22, no. 3, pp. 697–708, 2007.

[71] W. Waag, C. Fleischer, C. Schäper, J. Berger, and D. U. Sauer, "Self-adapting on-board diagnostic algorithms for lithium-ion batteries," *Proc. of 3rd German Symposium "Advanced Battery Development for Automotive and Utility Applications and their Electric Power Grid Integration"*, 2011.

[72] J. H. Aylor, S. Member, A. Thieme, and B. W. Johnson, "A Battery State-of-Charge Indicator for Electric Wheelchairs," *IEEE Transactions on Industrial Electronics*, vol. 39, no. 5, pp. 398–409, 1992.

[73] D. Linden, *Handbook of Batteries*, 3rd ed. McGraw-Hill, 2002.

[74] S. Buso and P. Mattavelli, *Digital Control in Power Electronics*, J. Hudgins, Ed. University of Nebraska - Lincoln: Morgan&Claypool, 2006.

[75] J. Macias, A. Exposito, and A. Soler, "A Comparison of Techniques for State-Space Transient Analysis of Transmission Lines," *IEEE Transactions on Power Delivery*, vol. 20, no. 2, pp. 894–903, Apr. 2005. [Online]. Available: http://ieeexplore.ieee.org/lpdocs/epic03/wrapper.htm?arnumber=1413331

[76] J. Cao, W. Du, H. F. Wang, and S. Q. Bu, "Minimization of Transmission Loss in Meshed AC/DC Grids With VSC-MTDC Networks," *Power Systems, IEEE Transactions on*, vol. 28, no. 3, pp. 3047–3055, 2013.

[77] T. Gönen, *Electric Power Transmission System Engineering: Analysis and Design*, ser. A Wiley-Interscience publication. J. Wiley, 1988. [Online]. Available: http://books.google.es/books?id=uNEiAAAAMAAJ

[78] A. Gomez-Exposito, A. Conejo, and C. Cañizares, *Electric energy systems: analysis and operation*, 2008.

[79] A. E. Leon, J. M. Mauricio, A. Gomez-Exposito, and J. A. Solsona, "Hierarchical Wide-Area Control of Power Systems Including Wind Farms and FACTS

for Short-Term Frequency Regulation," *Power Systems, IEEE Transactions on*, vol. 27, no. 4, pp. 2084–2092, 2012.

[80] S. Skogestad and I. Postlethwaite, *Multivariable feedback control: analysis and design*, 2005, vol. 21.

Appendix A

Laboratory setup

A.1 Laboratory setup

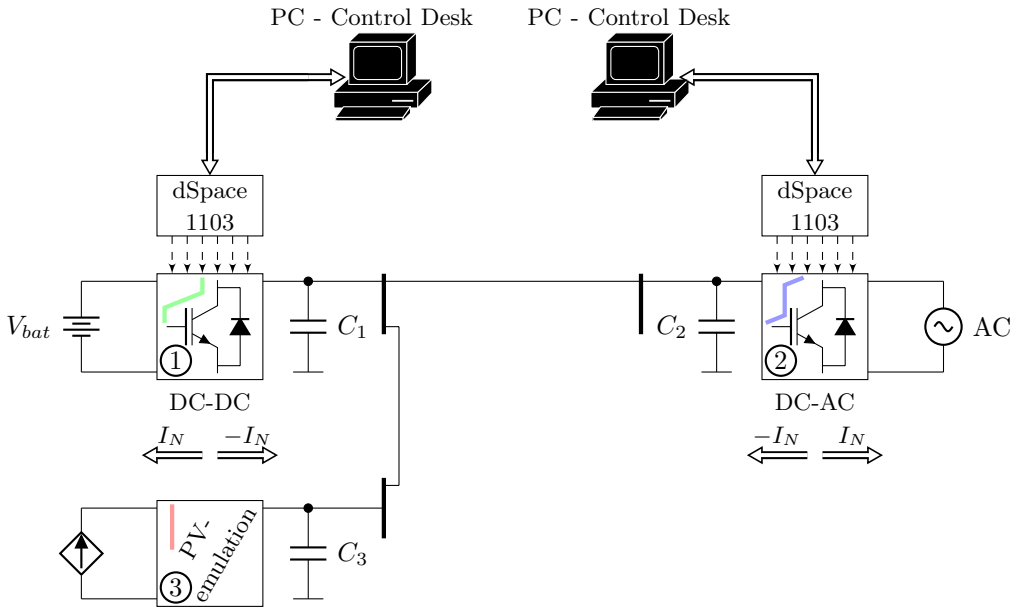

Fig. A.1: Block diagram of the 10 kW laboratory setup.

Fig. A.1 shows the block diagram of the 10 kW laboratory setup, pictured in Fig. A.2, that was used for obtaining the experimental results shown in this thesis. A three phase interleaved dc-dc converter, controlled by a dSpace 1103 unit, was connected to a 24 Ah lead-acid battery-bank. The high voltage part of the dc-dc converter was

Fig. A.2: 10 kW Laboratory setup.

connected to a two level grid connected inverter. A programmable Regatron power source was also connected to the common dc bus, and a real irradiance profile was programmed into the source in order to emulate a real PV generator.

The battery-bank, displayed in Fig. A.3, consists of 17 Sprinter – P12V600 lead-acid batteries with a nominal capacity of 24 Ah and an output voltage of 12 V. The batteries are connected in series, hence obtaining a total output voltage slightly above 200 V. However, since the output voltage of the battery is dependent on its current state of charge (SoC), the total voltage of the battery bank can be anywhere between 185 V and 225 V. Each battery is equipped with a LEM Sentinel sensor providing information on the voltage, temperature and the impedance as part of the battery management system (BMS). Additionally, the total current flowing in and out of the battery bank is monitored through a current sensor (ILink). The measured data is converted from the proprietary protocol of LEM to RS232 by a

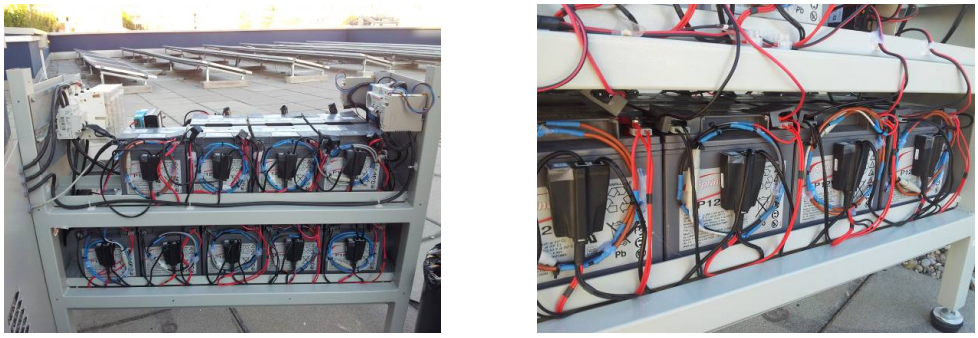

Fig. A.3: Battery bank and management system

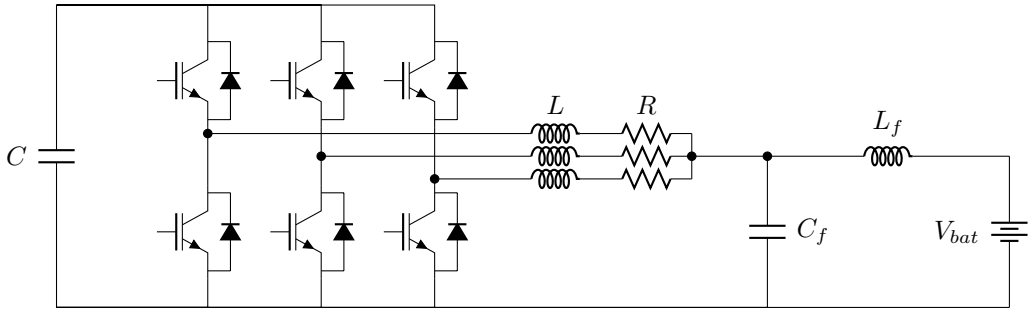

Fig. A.4: Electrical diagram of the three phase interleaved dc-dc converter.

special converting unit called S-box, and then it is sent to the dSpace unit connected to the dc-dc converter.

As was mentioned earlier, the battery-bank was interfaced to the dc bus by an three phase interleaved dc-dc converter. Fig. A.4 shows the structure of the converter, meanwhile, Fig. A.5 shows our laboratory prototype. The values of the used hardware components are listed in Table A.1.

A.2 Control of the dc-dc converter

One of the first tasks of this work was to design the control of the dc-dc converter connected to the battery-bank. Two control loops were implemented as discussed in Section 3.1. The external loop controls the dc bus voltage by regulating the reference

Fig. A.5: Three phase interleaved dc-dc converter

Table A.1: Parameters of the interleaved dc-dc converter

Component	Value	Description
L	250 [μH]	*filter inductor*
R	84 [mΩ]	*parasitic resistance of filter inductor*
L_f	750 [μH]	*filter inductor*
C_f	5 [μF]	*filter capacitor*
C	2.2 [mF]	*dc bus capacitor*

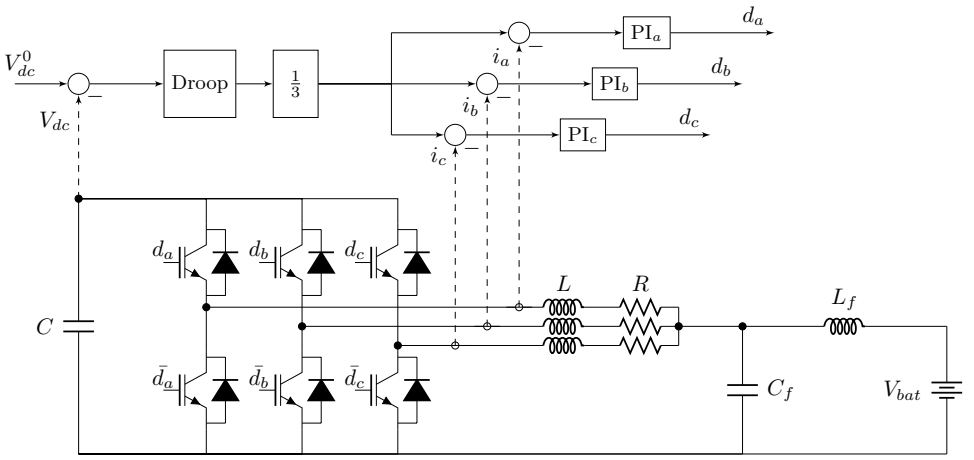

Fig. A.6: Control strategy for the interleaved dc-dc converter.

for the current control loop, as seen in Fig. A.6. The current controller is composed of three PI regulators, one for each converter leg, that directly control the PWM unit.

The parameters for the current controllers were obtained using the methods presented in [74] and then fine-tuned online. As can be seen in Table A.2, the parameters for the current controller of leg A of the converter are slightly different than the other two. This is because, due to manufacturing inconsistencies, the three phases of the converter, taking into account filters and sensors, are not exactly identical.

Fig. A.7 displays the steady state current in the three legs of the converter. The three phase currents, displaying 120 degrees of phase shift between them, are shown in purple, green, and yellow, together with the total current in cyan. The advantage of the interleaved topology can be noted here; while the currents in the three branches of the converter have a high ripple, the one in the total current is significantly lower.

In order to test the response of the current controllers, the dynamic response of the current in one leg of the converter is presented in Fig. A.8. The low voltage side of the dc-dc converter is connected to the battery bank, meanwhile, the high voltage side is connected to a constant voltage source. A step change in the reference of the current controller of 14A is then applied. A good performance of the system can

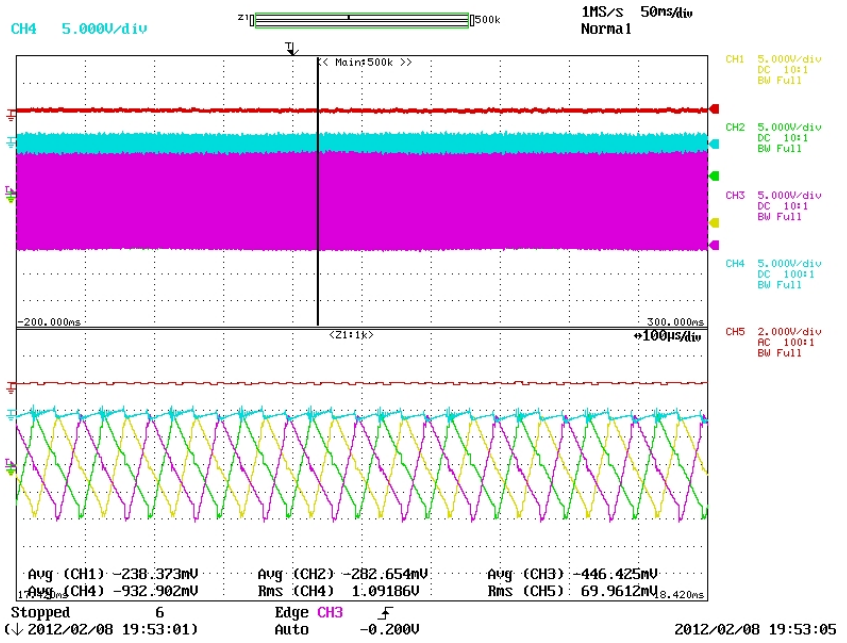

Fig. A.7: Steady state behavior of the current in the three legs of the converter (magenta, yellow, green) and total current (cyan).

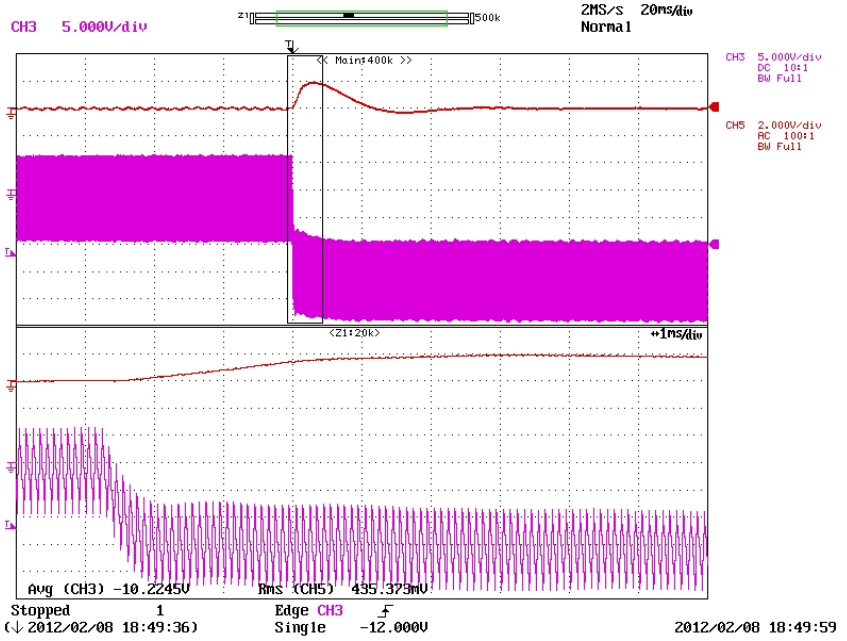

Fig. A.8: Step response of a 14 A step from -1A to -15A.

Table A.2: Parameters of the current and voltage controllers used in the experimental scenarios

Parameter		Value	Description
Current Control	f_{sw}	10 [kHz]	*switching frequency*
	PI_a-K_p	0.004	*proportional gain for the PI controller of leg A*
	PI_a-K_i	5.248	*integral gain for the PI controller of leg A*
	PI_b-K_p	0.004	*proportional gain for the PI controller of leg B*
	PI_b-K_i	4.381	*integral gain for the PI controller of leg B*
	PI_c-K_p	0.004	*proportional gain for the PI controller of leg C*
	PI_c-K_i	4.381	*integral gain for the PI controller of leg C*
Voltage Control	V_{dc}^0	685 V	*nominal voltage of the dc bus*
	NO	16 V	*height of the normal operating band*
	SH, SL	8 V	*height of the safety bands*
	CH, CL	8 V	*height of the critical bands*
	V_{dc}^{ch}	709 V	*maximum allowed voltage*
	V_{dc}^{cl}	661 V	*minimum allowed voltage*
	$SoC_{l1,l2}$	45%-30%	*low state of charge interval*
	$SoC_{h1,h2}$	60%-75%	*high state of charge interval*

be noted, with a raising time smaller than 1ms and a settling time of around 4ms. The red channel shows the dynamic response of the dc voltage. It can be noted that, when a change in the current reference is applied, the voltage source takes around 20ms to stabilize the bus voltage. This is an additional disturbance for the current control, but, even with this extra perturbation, the control is able to perform rather well.

Finally, Fig. A.9 shows a more complex scenario, where the capability of the dc-dc converter to control the dc-bus voltage is tested. The low voltage side of the dc-dc converter was connected to the battery bank. The high voltage side was connected to the dc-ac converter through the common 685 V bus and the dc-dc converter was set in charge of regulating the dc bus voltage through droop control. Unidirectional power flow, as well as bidirectional, were tested in the following sequence: the active power reference of the dc-ac converter was changed in steps from 0 kW to -10 kW, then from -10 kW to -5 kW, followed by -5 kW to 10 kW, 10 kW to 5 kW and, finally, 5 kW to 0 kW.

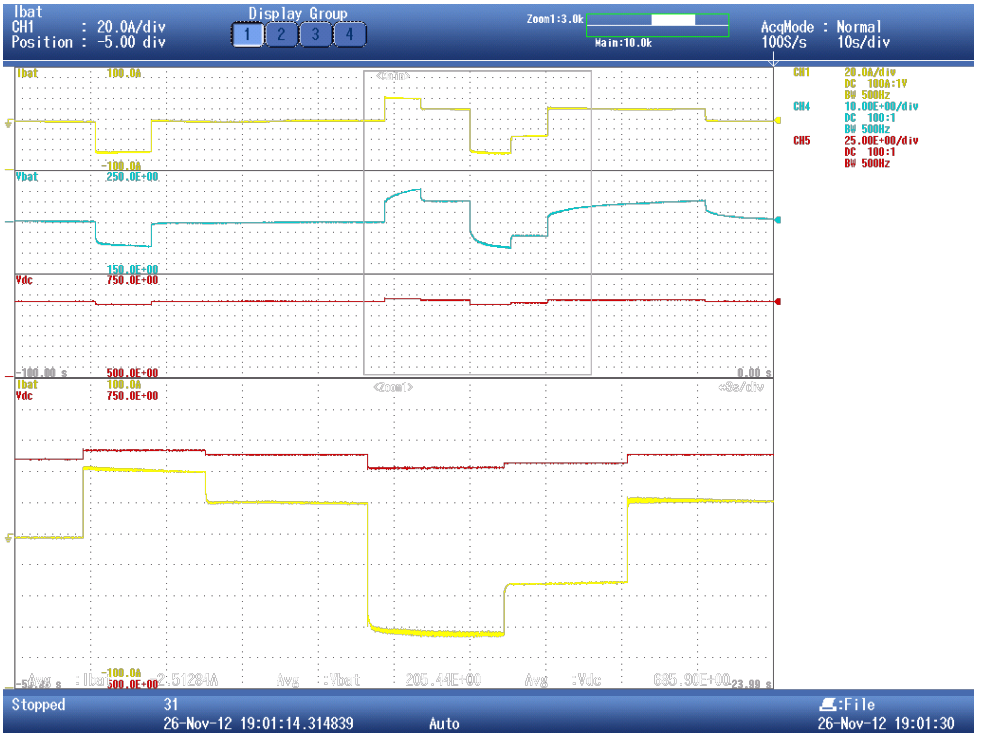

Fig. A.9: Droop voltage control. Total battery current (yellow), battery voltage (cyan), dc bus voltage (red)

As it can be seen in Fig. A.9, the dc bus voltage varies according to the implemented droop curve, as explained in Section 2.2. When the power reference is equal to the nominal, also the voltage is at the limit of the NO band, i.e., 693 V in our case.

Appendix B

Overshoot of typical transfer functions

B.1 Overshoot of second order systems

$H_2(s)$ in (B.1) is the canonical form of a second order system, where ω_n is the natural oscillation frequency of the system and ξ is the damping of the system. Considering the underdamped case, $\xi < 1$, the time response of the system, $y_2(t)$, to a step change can be calculated as shown in (B.2).

$$H_2(s) = \frac{\omega_n^2}{s^2 + 2\xi\omega_n + \omega_n^2} \tag{B.1}$$

$$\begin{aligned} y_2(t) &= \mathscr{L}^{-1}\left\{\frac{1}{s}\cdot H_2(s)\right\} \\ &= 1 - e^{-\xi\omega_n t}\left[\cos(\omega_d\cdot t) + \frac{\xi}{\sqrt{1-\xi^2}}\sin(\omega_d\cdot t)\right] \\ \omega_d &= \omega_n\cdot\sqrt{1-\xi^2} \end{aligned} \tag{B.2}$$

In order to get the maximum value of $y_2(t)$, we can set its derivative to zero, in order to obtain the time value, t^{pk}, at which the peak of y_2 occurs. Afterward, by evaluating y_2 at t^{pk}, one can obtain the peak overshoot, y_2^{pk} as shown in (B.3).

$$\begin{aligned} \left.\frac{dy_2(t)}{dt}\right|_{t=t^{pk}} &= 0 \\ t^{pk} &= \frac{\pi}{\omega_d} \\ y_2^{pk} &= 1+e^{-\pi\cdot\frac{\xi}{\sqrt{1-\xi^2}}} \end{aligned} \tag{B.3}$$

B.2 Overshoot of second order systems with an additional zero

The same methodology applied for calculating the overshoot of second order systems can be applied for second order systems with a zero. The transfer function of such a system is shown in (B.4).

$$H_{20}(s) = \frac{\omega_n^2\cdot(a\cdot s+1)}{s^2+2\xi\omega_n s+\omega_n^2} = a\cdot s\cdot H_2(s)+H_2(s) \tag{B.4}$$

When calculating the time response to a step change, one can see it as the sum between the response of a second order system and its derivative scaled by the a term, as seen in (B.5).

$$\begin{aligned} y_{20}(t) &= \mathscr{L}^{-1}\left\{\frac{1}{s}\cdot H_{20}(s)\right\} \\ &= a\cdot\frac{dy_2(t)}{dt}+y_2(t) \\ &= 1-e^{-\xi\omega_n t}\left[\cos(\omega_d\cdot t)+\beta\sin(\omega_d\cdot t)\right] \\ \beta &= \frac{\xi}{\sqrt{1-\xi^2}}-a\cdot\omega_d-\frac{\xi^2}{\sqrt{1-\xi^2}}\cdot a\cdot\omega_n \end{aligned} \tag{B.5}$$

Similar to the previous case, in order to obtain the peak value y_{20}^{pk}, the derivative of y_{20} has to be set to zero and then, the initial function has to be evaluated at the obtained peak time, t^{pk}, as shown in (B.6).

$$\left.\frac{dy_{20}(t)}{dt}\right|_{t=t^{pk}} = 0$$

$$t^{pk} = \frac{1}{\omega_d}\cdot\left[\tan^{-1}\left(-\frac{a\cdot\omega_n^2}{\omega_d+\xi\cdot\omega_n\cdot\beta}\right)+\pi\right]$$

$$y_{20}^{pk} = 1-e^{-\xi\omega_n t^{pk}}\cdot\left(\cos(\omega_d\cdot t^{pk})+\beta\cdot\sin(\omega_d\cdot t^{pk})\right) \tag{B.6}$$